Local Heat Transfer And Fluidization Dynamics Around Horizontal Tubes In Fluidized Beds.

Citation

CHANDRAN, RAVI. *Local Heat Transfer And Fluidization Dynamics Around Horizontal Tubes In Fluidized Beds.* 1980, https://preserve.lehigh.edu/lehigh-scholarship/graduate-publications-theses-dissertations/theses-dissertations/local-heat.

INFORMATION TO USERS

This was produced from a copy of a document sent to us for microfilming. While the most advanced technological means to photograph and reproduce this document have been used, the quality is heavily dependent upon the quality of the material submitted.

The following explanation of techniques is provided to help you understand markings or notations which may appear on this reproduction.

1. The sign or "target" for pages apparently lacking from the document photographed is "Missing Page(s)". If it was possible to obtain the missing page(s) or section, they are spliced into the film along with adjacent pages. This may have necessitated cutting through an image and duplicating adjacent pages to assure you of complete continuity.
2. When an image on the film is obliterated with a round black mark it is an indication that the film inspector noticed either blurred copy because of movement during exposure, or duplicate copy. Unless we meant to delete copyrighted materials that should not have been filmed, you will find a good image of the page in the adjacent frame.
3. When a map, drawing or chart, etc., is part of the material being photographed the photographer has followed a definite method in "sectioning" the material. It is customary to begin filming at the upper left hand corner of a large sheet and to continue from left to right in equal sections with small overlaps. If necessary, sectioning is continued again—beginning below the first row and continuing on until complete.
4. For any illustrations that cannot be reproduced satisfactorily by xerography, photographic prints can be purchased at additional cost and tipped into your xerographic copy. Requests can be made to our Dissertations Customer Services Department.
5. Some pages in any document may have indistinct print. In all cases we have filmed the best available copy.

University
Microfilms
International

300 N. ZEEB ROAD, ANN ARBOR, MI 48106
18 BEDFORD ROW, LONDON WC1R 4EJ, ENGLAND

CHANDRAN, RAVI

LOCAL HEAT TRANSFER AND FLUIDIZATION DYNAMICS AROUND HORIZONTAL TUBES IN FLUIDIZED BEDS

Lehigh University PH.D. 1980

University
Microfilms
International 300 N. Zeeb Road, Ann Arbor, MI 48106

LOCAL HEAT TRANSFER AND FLUIDIZATION DYNAMICS AROUND HORIZONTAL TUBES IN FLUIDIZED BEDS

by

Ravi Chandran

A Dissertation
Presented to the Graduate Committee
of Lehigh University
in Candidacy for the Degree of
Doctor of Philosophy

in

the Department of
Mechanical Engineering and Mechanics

Lehigh University
1980

Approved and recommended for acceptance as a dissertation in partial fulfillment of the requirements for the degree of Doctor of Philosophy.

September 19, 1980
(date)

John C. Chen
Professor in Charge

Accepted September 19, 1980
(date)

Special committee directing
the doctoral work of
Ravi Chandran Natarajan

John C. Chen
Chairman

E K Levy

T E Jackson

John C Chen

Marvin Charles

Dedicated to

LV, MAMA, DAD & GP

ACKNOWLEDGMENT

Many individuals have contributed to the advancement of this work. I would like to express my appreciation and gratitude to all of them, and in particular to the following:

- to Professor J. C. Chen for initiating me into this topic and for guiding me. His technical expertise and scientific acumen have inspired me a great deal and have influenced the course of this work;
- to Mr. F. W. Staub, Dr. G. S. Canada, and Professors E. K. Levy, M. Charles, D. O. Rockwell and T. E. Jackson for their time and for their comments and suggestions;
- to Messers R. E. Towne, F. J. Pechacek Jr., F. J. Wehden and J. A. Bunderla III for fabricating the various components of the test facility. Their cooperation and timely help were invaluable. I wish to specially thank Mr. R. E. Towne and Mr. F. J. Pechacek Jr. for their skill and patience in constructing the instrumented test tubes. I am sure they would be more than glad not to see me again in the ME shop premises;
- to Mr. T. C. Nixon for developing the electronics from scratch for the capacitance probe. It is also admirable that he kept his composure despite my constant nagging during the testing stage;

- to Mr. G. E. Mcconnel and Mr. N. A. Deily of the Computer Center for their help in interfacing the system for data transfer;
- to Dr. R. T. Wood and Messers. S. J. Brzozowski, K. Hardcastle, G. T. Astin, S. P. Urbaetis and P. A. Morgan for their help and assistance during the course of experimentation at General Electric Company. I am grateful to GE Corporate R&D Center for granting me permission to use their test facility and am thankful to the RIAS program for providing monetary support;
- to Mr. and Mrs. Ersoy for their help with the figures;
- to my parents for their understanding;
- to the Corporate Research and Development Center of General Electric Company for sponsoring this project;
- to Ms. S. L. Cawley, D. Reiss, J. J. Loosbrock and Mrs. K. Dickie for their excellent typing of this manuscript;
- and finally to all those brave individuals who are determined to read past this page, I wish good luck.

TABLE OF CONTENTS

TABLE OF CONTENTS (Continued)

LIST OF TABLES

LIST OF FIGURES

LIST OF FIGURES (Continued)

LIST OF FIGURES (Continued)

LIST OF FIGURES (Continued)

NOMENCLATURE

Ar	Archimedes number, $g\bar{d}_p^3\rho_g(\rho_s-\rho_g)/\mu_g^2$
a_1,a_2,a_3	coefficients in Equation (17)
B	geometric factor, Equation (13)
b_1	coefficient in Equation (29)
b_2	coefficient in Equation (30)
C	effective correction factor, Equation (16)
C_p	volumetric specific heat
c_o	coefficient in Equation (2)
c_1,c_2	property correction factors, Equation (14)
c_p	specific heat
D	tube diameter
$\bar{d}_p$	mean particle diameter
E	coefficient in Equation (23)
F	parameter in Equation (25), E/S
F_i	instantaneous Fourier number, $(k_D t)/[\rho c_p)_D \bar{d}_p^2]$
F_o	time-mean Fourier modulus $(k_D\bar{\theta}_D)/(C_{pD}\bar{d}_p^2)$
f( )	function of the parameters in paranthesis
f_L	fraction of the total time lean phase is in contact with the tube surface
G	superficial mass velocity
g	acceleration due to gravity
H	center-line elevation of instrumented tube above the distributor
H_S	static bed height

NOMENCLATURE (Continued)

h	local heat transfer coefficient, (time-averaged)
$\bar{h}$	average heat transfer coefficient, (circumferentially-averaged)
h_D	effective heat transfer coefficient in the dense phase
h_f	heat transfer coefficient that accounts for the effect of fluid flow on conduction
h_g	heat transfer coefficient for gas flow alone
h_L	effective heat transfer coefficient in the lean phase
h_{mf}	heat transfer coefficient at minimum fluidization condition and in the absence of surface renewal
h_s	heat transfer coefficient due to surface renewal of a dense medium with stagnant fluid
h_{si}	instantaneous heat transfer coefficient during transient conduction
h_s'	time-averaged heat transfer coefficient for dense phase residence time of $\bar{\theta}_D$
I	number of dense phase contacts in the sample time period
J	number of lean phase contacts in the sample time period
k	thermal conductivity
k^o	thermal conductivity in a packed medium with motionless fluid
k'	thermal conductivity due to heat flow through solid-fluid-solid, Equation (13)
L_R	capacitance signal reference level for demarcation between dense and lean phases
Nu	Nusselt number, $(\bar{h}\bar{d}_p)/k_g$
Nu_s'	time-mean Nusselt number, $(h_s'\bar{d}_p)/k_D$
n_1	exponent in Equation (29)

NOMENCLATURE (Continued)

n_2	exponent in Equation (30)
P	absolute pressure
Pr	Prandtl number, $(c_{pg}\mu_g)/k_g$
q	local heat flux
Re	Reynolds number, $(G\bar{d}_p)/\mu_g$
Re_G	Reynolds group, $(G\bar{d}_p\rho_s)/(\rho_g\mu_g)$
Re_{mf}	Reynolds number at minimum fluidization condition $(\rho_g U_{mf}\bar{d}_p)/\mu_g$
S	slip parameter, U_{rg}/U_{rs}
T	temperature
T_1	dense phase temperature in domain 1, Figure 63
T_2	dense phase temperature in domain 2, Figure 63
t	time
U_{gm}	gas velocity based on minimum flow area
U_{mf}	superficial gas velocity at minimum fluidization condition
U_N	normalized velocity parameter or reduced velocity, $(U_{sg}-U_{mf})/(U_t-U_{mf})$
U_{rg}	real velocity of gas
U_{rs}	real velocity of solid
U_{sg}	superficial gas velocity
U'_{sg}	local superficial gas velocity
U'_{ss}	local superficial solid velocity
U_t	particle terminal or free-fall velocity
$\bar{U}_t$	free-fall or terminal velocity for particles of size $\bar{d}_p$

NOMENCLATURE (Continued)

w	natural log of conductivity ratio, $\ell n(k_D/k_g)$
X	parameter defined in Equation (31)
x	distance from the wall, Figure 63
x_1	non-dimensional quantity $(g\bar{d}_p)/(U_{sg}\bar{U}_t)$
x_2	non-dimensional quantity, $[(\frac{\rho_s}{\rho_g})(\frac{1-\alpha_L}{\alpha_L})(\frac{c_{ps}}{c_{pg}})]$
x_p	heat penetration depth
z	dimensionless distance from the wall, $x/\bar{d}_p$

Greek Symbols

α	void fraction
$\bar{\alpha}$	average bed void fraction
α_c	void fraction cut-off value for differentiating between dense phase and lean phase contact with the tube surface
β	angular position around the circumference of tube, measured from the top of the tube
ΔT	temperature difference, T_W-T_B
ε_H	eddy diffusivity for heat
ε_M	eddy diffusivity for momentum
η	excess temperature, T_2-T_B
η_z	first-order derivative, $\partial\eta/\partial z$
η_{zz}	second-order derivative, $\partial^2\eta/\partial z^2$
θ	residence time

$\bar{\theta}_D$	dense phase root-square-average residence time, $\left[\sum_{i=1}^{I} \theta_{D_i} \Big/ \sum_{i=1}^{I} \sqrt{\theta_{D_i}}\right]^2$
μ	dynamic viscosity
ρ	density
ϕ	excess temperature, T_1-T_B
ϕ_z	first-order derivative, $\partial\phi/\partial z$
ϕ_{zz}	second-order derivative, $\partial^2\phi/\partial z^2$
ψ_s	particle shape factor

Subscripts

A	air
B	bed, (away from the tube surface)
D	dense phase
e	effective value
g	gas
L	lean phase
mf	minimum fluidization state
P packed	packed state
s	solid/particle
w	wall/tube surface

ABSTRACT

This research task involved the study of the characteristics of fluid mechanics and heat transfer around horizontal tubes immersed in fluidized beds. The objective was to develop a phenomenological model for the heat transfer process. To achieve this, the following steps were taken: (i) experimentally investigate bed-surface contact dynamics and generate quantitative information on fluidization behavior close to the tube surface, and (ii) measure local heat transfer coefficients around the tube for the purposes of comparison and validation of the model.

The experimental program was carried out in two different test facilities. Measurements were obtained in air-fluidized beds of glass beads for both a single tube and a ten-row bare tube bundle configuration. Special instrumented tubes were developed for the measurement of both local heat transfer coefficients and local fluidization characteristics. The heat transfer data were obtained by employing a segmented heating concept and the bed-surface contact dynamics were studied using the capacitance probe technique. Measurements were made at 45° intervals around the circumference of the horizontal test tubes.

The test results indicated that local heat transfer coefficients are strongly influenced by angular position and gas flow rate, as well as by particle size and system pressure. The circumferentially-averaged heat transfer coefficients exhibited a general tendency to increase with decreasing particle size and

increasing system pressure. The heat transfer coefficients for a tube in an inner-row position within the bundle were found to be slightly higher than those for a tube in the bottom-row. Comparison of the average heat transfer coefficient data obtained in this study with some of the existing correlations for heat transfer from horizontal tubes showed that the correlations are unsatisfactory.

The capacitance signals showed that the transient bed-surface contact behavior changes drastically around the perimeter of the tube. Quantitative information on the local fluidization characteristics were obtained by differentiating between a "dense phase" and a "lean phase" contact at the tube surface. The capacitance signals were processed to determine the values of the following parameters--root-square-average residence time of the dense phase, fractional contact time of the lean phase, and the average void fractions of the dense and the lean phases. The magnitude of these quantities were found to strongly depend on circumferential position, gas flow rate, particle size and system pressure. From the experimental data, empirical correlation curves for the fluidization parameters were generated for use in the phenomenological model to predict heat transfer coefficients.

Based on different mechanisms for dense phase and lean phase contact at the tube surface, a model for local heat transfer coefficient was developed. The dense phase heat transfer process was modeled by packet renewal mechanism, and the lean phase transfer process by pneumatic turbulent convection mechanism. With input data on local fluidization characteristics, the model was able to successfully predict both local and average heat transfer coefficients for the range of test conditions covered in this investigation.

1. INTRODUCTION

1.1 Background

During the past three decades, fluidization technology has made an impact on many an industrial operation. Since the first major commercial use of the technique of fluidization in the petroleum industry, it has gained prominence in chemical, metallurgical, coal, environmental and nuclear industries. This development has resulted from such attributes as good contact between the solids and the fluid, vigorous mixing and agitation, and excellent heat and mass transfer characteristics attainable in fluidized-bed operation.

A remarkable feature of the fluidized bed is its temperature uniformity. This property makes it attractive for processes that are temperature-dependent. In these applications, it is usually required to either supply or remove heat in order to maintain the desired temperature level in the bed. This heat transfer can be accomplished by means of either the fluidizing medium or an exchange surface. For the thermal design of such systems, a knowledge of either the fluid/solid or bed/surface heat transfer characteristics is needed.

Many applications of fluidized beds involve heat transfer to or from immersed tubes and tube bundles. Current interest in processing fossil fuels for steam and power generation has given an added impetus to the study of bed/tube heat exchange. The rate of heat transfer between a fluidized bed and a submerged tube depends upon a number of factors, including the properties of the bed material and the contact fluid, bed and tube geometries, and the fluidization state [1-4]. Measurements of heat transfer between fluidized beds and horizontal tubes have been carried out by many investigators and both experimental data and correlations are reported in the literature [5-14]. Reviews of the work are given in [1-4, 15-18].

In general, early investigators of heat transfer between a fluidized bed and an immersed surface had resorted to the classical approach of correlating experimental data in terms of a power-law relationship. These correlations were developed by manipulating dimensionless parameters with little or no attention to the physics involved in the heat transfer process. Often, it was required to expand the equations to unwieldy proportions in order to achieve a good curve-fit. Thus, these empirical relationships became restricted in scope and data-span-limiting, due to the inadequate allowance made for the dynamic behavior of fluidized beds.

Over the years, a number of researchers have attempted the mechanistic approach and have arrived at semi-empirical relations for the heat transfer coefficient. In what follows, the contribution due to radiation is considered insignificant. The mechanisms that have been proposed by the various investigators for the heat transfer process are:

i. Film Model - a fluid film adjacent to the exchange surface constitutes the principal resistance to heat transfer and moving solid particles scour away the limiting film, reduce the resistance and increase heat transfer [19-23]. These models are based on the fluid convection mechanism and generally involve a steady state concept of the heat transfer process. This hypothesis is not supported by the experiments of van Heerden et al. [24] and Ziegler and Brazelton [25]. Herein, absorption of heat by the fluidized solids as opposed to the reduction of film resistance, is advocated as the dominant mechanism for heat transfer.

ii. Penetration Model - either "packets" [26,27] or "single" particles [28-30] contact the heat exchange surface for a certain duration, are periodically replaced by fresh material, undergo transient conduction during the residence time at the surface, and thus serve to transfer heat by transport of sensible heat. These models utilize an unsteady state approach and are based on the "surface renewal" concept that accounts for particle convective transport.

The packet model, proposed by Mickley and Fairbanks [26], treats the fluid-solid medium (packet) that comes into contact with the exchange surface as homogeneous and assigns it the average thermal properties of the bed at incipient fluidization. This is unrealistic; besides, the effect of the transfer surface on local particle packing is ignored. The error introduced is likely to be significant, especially for short contact times. Also, this model predicts an infinite heat transfer coefficient in the limit of zero residence time and a zero coefficient in the limit of infinite contact time.

Modifications have been suggested by different workers to improve the basic packet model cited above. Baskakov [31] introduced an empirical, time-independent contact resistance at the wall-packet interface to achieve a good comparison with data. Yoshida et al. [32] used an approach analogous to the film-penetration theory advanced by Toor and Marchello [33] for gas absorption into liquids. Their model unified the steady state conduction and unsteady state absorption concepts and used a limiting emulsion layer (packet) thickness. The inclusion of a characteristic length that is usually unknown, and the retention of the low Fourier number deficiency of the original packet model were the limitations of this work. Koppel et al. [34] not only invoked the film-penetration mechanism of Toor and Marchello to assign a finite thickness to the packet, but also allowed a non-zero surface-packet thermal resistance, in the manner of Baskakov [31]. Kubie and Broughton [35] disliked the use of empiricism and introduced the concept of a property boundary layer to account for the wall effect. Özkaynak and Chen [36] used the concept of penetration depth to make an allowance for the influence of the wall on packing at short residence times. Gel'perin and Einstein [15] solved the basic packet model in terms of two heat transfer resistances, one due to the increased voidage in the vicinity of the wall that extended to one-half the diameter of a particle, and the other due to an adjoining two-phase packet. Antonishin et al. [37] analyzed heat conduction in a dispersed system by allowing for local temperature relaxation in the heterogeneous medium.

The single particle model, proposed by Botterill and Williams [28], recognized the heterogeneity of the fluidized media and considered transient conduction between the exchange surface and a contacting spherical particle immersed in fluid. The resulting parabolic differential equations were solved by a numerical scheme. This model turned out to be inappropriate for long residence times wherein the depth of heat penetration exceeded one particle diameter. Realization of this limitation led to the development of a two-particle model by Botterill and Butt [38] and subsequently, a model based on a solid-chain of unlimited length by Gabor [39]. All these models had to resort to an artificial fluid-film gap between the surface and the first-row of particles to obtain a good data-fit.

Ziegler et al. [30] considered the unsteady-state heat absorption by a cold sphere immersed in stagnant gas and in contact with a hot wall. They solved for the time-mean heat transfer coefficient by using a gamma distribution to represent the residence time of the particles. This model resembles that of Botterill and Williams and suffers from similar limitations. Chung et al. [40] extended the model of Ziegler et al. to large solid-to-fluid thermal conductivity ratios.

Some additional studies [41-44] have provided comparisons of experimental heat transfer coefficient data with the predictions of selected penetration models.

iii. Gas Convection - A few investigators [3, 45-47] have stressed the importance of gas convective heat transfer for fluidization of large particles and elevated pressure operation, and have presented data and correlations.

iv. Turbulent Flow Model - Staub [48] has proposed a turbulent gas-solids flow model to predict the heat transfer coefficients for tube banks immersed in fluidized beds. It is essentially intended for use under conditions of high gas flow velocity and large particle fluidization.

In order to determine the applicability of the mechanisms outlined above, it is necessary to know the transient contact characteristics between the bed emulsion and the heat transfer surface on a local basis. Until recently, a lack of such knowledge happened to seriously hamper the development and use of phenomenological models [49,50].

Comparisons of existing design correlations for bed-to-tube heat transfer coefficient are presented in [14, 15, 18, 51]. As pointed out by Chen [51], there is little agreement amongst the various correlations or between correlations and data. This state is attributed to incorrect or insufficient accounting of the governing parameters/mechanisms as well as to the empiricism that is usually invoked in fitting data. From an applications standpoint, there is a need for improved phenomenological understanding of the mechanisms and appropriate modeling of the transport processes.

The foregoing remarks are especially true for tubes placed horizontally in fluidized beds. Since the fluid flow is in a direction normal to the tube axis for horizontal tubes, it is incorrect to assume axial symmetry. Local heat transfer coefficients could, in principle, vary with circumferential position on the tube surface. Evaluation of this effect has been hampered by insufficient experimental data on local heat transfer coefficients. A few studies [15, 18, 42, 52-54] have reported local measurements around horizontal tubes. These data are of limited scope, since they were obtained from experiments performed at atmospheric pressure and with relatively small particle sizes ($\bar{d}_p < 350$ μm).

From a review of the literature, the existence of a knowledge gap was uncovered. The need for understanding the governing mechanisms was also recognized. This work was initiated to provide the necessary information and develop a model suitable for practical applications.

1.2 Scope of Present Investigation

The objective of this research effort was to study the characteristics of local fluid dynamics and heat transfer around horizontal tubes in fluidized beds. Emphasis was placed on assessing the dynamic nature of solid-fluid behavior close to the tube surface. Transient fluidization data were obtained on a local basis around the circumference of horizontal tubes, using the capacitance probe technique developed at Lehigh [49]. This fluid-dynamic information was then used to develop a phenomenological model for the heat transfer process. For the purposes of comparison and validation of the model, local heat transfer measurements around the tube were made using a test tube specially developed for this investigation.

Specifically, the experimental program involved the study of the effect of variations in gas flow rate, system pressure and particle size on heat transfer from a single horizontal tube, and the effect of variations in gas flow rate and tube location on heat transfer from a horizontal tube bundle immersed in fluidized beds. Local heat transfer and fluidization measurements were all obtained in air-fluidized beds of glass beads, for both a single tube and a ten-row bare tube bundle configuration.

2. EXPERIMENTAL METHOD

2.1 Test Apparatus

The experimental program was carried out in two different fluidized bed test facilities, one at Lehigh University and the other at the Corporate Research and Development Center of General Electric Company. Schematic diagrams of these are shown in Figures 1 and 2 respectively.

The test apparatus shown in Figure 1 was designed, fabricated and assembled specifically for this task. The facility consisted of two fluidized beds, one for operation at atmospheric pressure and the other for operation at pressures up to 500 kPa. Fluidizing air was supplied by a pair of reciprocating compressors (Ingersoll Rand, Model LLE Air Cube, two stage, two cylinder double-acting type), capable of delivering 0.47 m^3/s at a maximum pressure of 860 kPa. The air flow rate was monitored at a specially designed flowboard that used annubar sensors (pitot tube rakes) with associated read-out instruments. The flow metering system was designed to measure air flow rates, from 0.004 to 0.57 m^3/s and at pressures up to 690 kPa, with an accuracy of two percent. The single tube tests were all performed in the pressurized bed of 0.203 m inside diameter, shown in Figure 3. The middle section of the cylindrical vessel was fabricated from acrylic plastic to permit visual observation. Aluminum headers at the top and bottom of the bed were used for air and instrumentation connections. The distributor was a sandwich assembly of a perforated steel plate, a plastic porous sheet and a metal screen (Figure 4). The pressure drop across the distributor ranged from 25 to 350 mm H_2O, depending on the flow rate of air.

The tube bundle experiments were carried out in GE's atmospheric pressure fluidized bed of 0.305 m square cross-section (Figure 2). The bed was transparent with column walls made out of Lexan sheets. The distributor employed was of the bubble-cap type. Air was supplied to this test facility by a two-stage blower driven by a 75 KW motor. Air flow measurements were made by means of ASME flow nozzles and associated instrumentation.

2.2 Heat Transfer Test Section

A specially instrumented tube was developed for the measurement of local heat transfer coefficients. Figure 5 shows the details of the test tube. Eight strips of 50.8 μm thick Inconel foil were bonded to a solid Lexan rod as shown. Each foil strip was heated by an individually controlled AC power supply. Miniature thermocouples (0.25 mm diameter wires) were placed in grooves directly beneath the foil strips. The temperature sensed by the thermocouples were corrected (less than 1 percent correction of ΔT) to obtain surface temperatures at the top of the heated foils. All the heat transfer tests were carried out under isothermal wall conditions, wherein the power to individual foil strips were adjusted to obtain a uniform temperature around the circumference of the rod. The measured input power to each strip then permitted the determination of the local heat fluxes, $q(\beta)$. Thermocouple readings yielded the difference between the foil surface temperature and the bed bulk temperature, ΔT. From these measurements, local heat transfer coefficients could be obtained directly,

$$h(\beta) = q(\beta) \div \Delta T \qquad (1)$$

The heat transfer measurements were all made at angular positions 45° apart around the circumference of the horizontal test tubes.

The power input to each foil was regulated by an electrical circuit, consisting of a powerstat, a fuse, a fixed resistor and a current shunt, in series with the heater strip. The circuit components were all mounted on an electrical control panel.

All the instrumentation lead wires were strung from the interior of the pressurized bed, through compression seals, to a common junction box. The terminal box was hooked up to a scanning datalogger (Esterline Angus Key Programmable Data System - PD2064 with 64 channels) by means of a cable and a set of multipin connectors. The data system featured two output devices, an onboard digital printer and a RS-232-C interface. The interface, in turn, was coupled to a cassette recorder (Techtran 8410 Datacassette System). Several samples were taken for each test run and the data were both printed out on paper and recorded on cassettes. Subsequently, the central computer (CDC 6400) was used to process the data as well as record the data on 7-track magnetic tapes.

2.3 Capacitance Test Section

Fluidization characteristics at the surface of a tube were determined using the capacitance probe technique developed at Lehigh [49]. Two different test sections, one for use in the multi-tube experiments (Figure 6) and another for use in the single tube experiments (Figure 7), were designed and instrumented. The test tube shown in Figure 6 consisted of a micarta cylinder flanked by two aluminum tubes. The micarta piece carried a pair of miniature capacitance electrodes implanted flush with the surface. In the case of the test section exhibited in Figure 7(a), an aluminum solid cylinder with a Lexan insert containing the capacitance electrodes was used instead of the micarta piece. This was done in order to provide a superior ground shield. Figures 7(b) and 7(c) show the details of construction.

The electrode leads, in both instances, were connected to a circuit designed to sense capacitance changes of the order of a few pf [55]. A block diagram of the circuit is shown in Figure 8. In principle, it operates on an amplitude modulation scheme to yield a DC voltage output proportional to the capacitance sensed at the electrodes. The probe capacitance forms one leg of a modified wheatstone bridge circuit with a capacitance reactance and pure resistances constituting the other three legs. The bridge is excited by a low distortion oscillator. The free running frequency and the bridge controls are adjusted so as to obtain a null output when the probe is exposed to air. A change in the probe capacitance from this value unbalances the bridge and amplitude modulates the signal. This output signal is amplified and buffered by a F.E.T. op amp. located within the test tube and fed into a signal conditioner through a coaxial cable. Herein, the AC component is filtered out to get a DC output that varies with the probe capacitance. The power supply used in this system has two dual tracking plus-minus voltage regulators--one for the probe electronics and the other for the oscillator and amplifier circuits in the signal conditioner box.

For the tests, the bridge excitation frequency was set at 22.3 KHz and the input power to the system was fixed at ±15V. The probe circuitry was sufficiently miniaturized to permit mounting directly within the test tube. Metallic end tubes provided shielding for the probe electronics.

This new circuit has the ensuing advantages over the capacitance bridge circuit used in previous studies [49,50]. It does not inhibit the use of long lead lengths, yields a cleaner output signal with a high signal-to-noise ratio, responds faster, and provides a TTL compatible output [55]. It is also compact and less expensive to build.

The probe output was continuously monitored on a digital oscilloscope (Nicolet 1090A Explorer Digital Oscilloscope). From time to time, a signal was captured on the scope and routed to the Techtran Cassette recorder through a RS-232-C interface (Nicolet Model 194 A). Several such samples were taken and recorded on cassettes for each test run. Once again, the central computer (CDC 6400) was used to process the signals as well as record the data on 7-track magnetic tapes.

Transient bed-surface contact measurements were made at angular positions 90° apart around the circumference of a single horizontal tube and at 45° apart around a test tube positioned at two locations in a tube bundle.

2.4 Test Parameters

The single tube studies were carried out in fluidized beds of glass beads over a range of air flow rates (up to 12 times the minimum fluidization flow rate). Data were obtained for five different particle sizes ($125 \leq \bar{d}_p \leq 1580$ μm) and at pressures of 101.3, 202.6 and 405.3 kPa. The multi-tube experiments were performed with a medium size particle ($\bar{d}_p = 650$ μm) and at atmospheric pressure. Local heat transfer and fluidization dynamic measurements were obtained for a tube at two different positions within a ten-row bare tube bundle and over a range of air flow rates. Geometry of the tube bundle is shown in Figure 9. The characteristics of the various test particles are furnished in Table 1. The mean particle diameter ($\bar{d}_p$) was computed on the usual basis of weight fractions [1,2]. The minimum fluidization velocity (U_{mf}) was determined experimentally by observation of pressure drop behavior. The value for the terminal velocity (U_t) was calculated by standard equations [1] for the smallest particle size in the bed.

In all tests, the static height of the (unfluidized) bed (H_s) was 0.457 m. In the case of single tube experiments, the center-line elevation of the tube above the distributor (H) was held constant at 0.229 m. The tube was 28.58 mm in diameter (D) and 188.9 mm in length. In tube bundle experiments, the instrumented tube was positioned at locations shown in Figure 9. The test tube was 285.8 mm long and had a diameter (D) of 31.75 mm. The heat transfer measurements were all made at angular positions 45° apart around the circumference of the horizontal test tubes. Capacitance data were obtained at 90° intervals in the case of single tube experiments and at 45° intervals in the case of multi-tube experiments.

3. EXPERIMENTAL RESULTS

3.1 Heat Transfer Data

Heat Transfer from a Single Horizontal Tube

Local heat transfer measurements were obtained around a single tube for five different particle sizes and at three different pressures. The data are furnished in Tables 2 through 6.

The local heat transfer coefficients obtained around a single tube, for a fluidized bed of a medium size particle (GT-3), are shown in Figure 10. Data are plotted for fluidization at a pressure of 202.6 kPa and at three different gas flow rates. It is seen that the heat transfer coefficients are vertically symmetrical about the axis as expected, confirming the reproducibility of the instrumentation method. Secondly, it is apparent that the coefficients vary significantly with changing gas flow velocity and changing angular position around the tube. At the lowest velocity indicated, the maximum heat transfer coefficient is found at the sides of the tube (90°/270° positions). A distinct minimum in the coefficient is found at the top of the tube (0° position). This result is consistent with the observations reported in [56-58], which indicate the presence of a stagnant cap of solid particles at the top of the tube at low flow rates. An increase in the gas flow rate serves to enhance heat transfer for all positions around the tube and results in a much more uniform distribution of the coefficients. The location of the maximum coefficient remains unchanged and still occurs at the sides of the tube. With further increase in gas velocity, the trend reverses and a decline in the local coefficients occurs at all angular positions. At the higher velocities, the maximum coefficient occurs at the top of the tube. This complex trend was observed for essentially all the runs and is an indication that the local heat transfer mechanisms change significantly with varying fluidization states.

For a given particle, fluidization gas flow velocity range is bounded by minimum fluidization velocity (U_{mf}) and terminal entrainment velocity (U_t). To compare results for different bed particles, it is desirable to select an appropriate generalized velocity parameter. The ratio of the superficial gas velocity to either limiting velocities (i.e. U_{sg}/U_{mf} or U_{sg}/U_t) is awkward to use in comparing results obtained with particles of different sizes, because the range of flow velocities is large for small particles [$(U_t/U_{mf}) \sim 30$ to 80] but small for large particles [$(U_t/U_{mf}) \sim 7$ to 15]. In this study, a normalized velocity parameter ($U_{sg}-U_{mf}/U_t-U_{mf}$) is used to characterize the fluidization flow. The value of this velocity parameter (U_N) usually lies between 0 and 1. For fine powders, however, the value may exceed unity unless U_t is revised as the terminal velocity for the largest particle in the size range. The magnitude of U_N is indicated for all data shown in Figures 10 through 20.

The effect of particle size on the local heat transfer coefficients at atmospheric pressure is shown in Figure 11. The heat transfer coefficients at the sides and bottom portion of the tube show a continuous decline with increasing particle size. The coefficients at the top of the tube tend to increase for an initial increase in particle size from small to medium, but then decrease with further increase to large particle size. However, the magnitude of variation is less pronounced at the top of the tube, as compared to the sides and bottom. It is also worth noting that the heat transfer coefficients are highly nonuniform around the circumference of the tube for small particles (125 μm) but are relatively more uniform for large particles (1580 μm). These data are representative of results for low to moderate fluidization flow rates.

The effect of pressure on the local coefficients is exhibited for small particles (245 μm) in Figure 12 and for large particles (1580 μm) in Figure 13. Each plot corresponds to a specific value of the normalized velocity parameter. It is evident that there is a significant improvement in the heat transfer coefficients due to an increase in pressure for both particle sizes. The circumferential distribution is seen to be somewhat different for the two particles, particularly at the higher pressure (405.3 kPa). The top and bottom portions of the tube are more effective in transferring heat in the case of small particles, while in the case of large particles, the sides are better heat transfer locations. This complex effect of pressure on heat transfer for particles of different sizes results from the relative contributions of packet-conduction and dilute-phase convection mechanisms. Increasing pressure tends to increase the gaseous conductivity and convection. However, increasing pressure decreases frequency of packet renewal resulting in a decline in the effectiveness of packet-conduction. Thus the overall effect depends on the relative contributions of conductive and convective mechanisms, which are different at different circumferential locations for particles of various sizes.

Some limited data on local heat transfer coefficients for horizontal tubes are available in the literature [15, 18, 42, 52-54]. Because of differences in the test parameters, it is difficult to make a direct comparison of the data from the various investigations. But a review of all the test results indicates general qualitative agreement. For the purposes of illustration, a representative sample drawn from the data of Berg and Baskakov [54], Gel'perin et al. [15,53] and this study are shown in Figure 14. The plot gives a measure of the distribution of the relative heat transfer coefficients ($h/\bar{h}$) around the tube. It is seen that the profiles of the local coefficients around the perimeter are rather similar in nature although the values of the test parameters are quite different. The local fluidization characteristics seem to be the common denominator. Thus, it is plausible that a general relationship between the system parameters and the local fluidization dynamics could be found, and that information in turn could be used to predict the local heat transfer coefficients.

The values of the average heat transfer coefficient around the tube ($\bar{h}$) have been calculated from the measured local coefficients (h), and some sample results are plotted in Figures 15 and 16. Figure 15 shows data for three different particle sizes at the same pressure (101.3 kPa). The main part of Figure 16 shows a cross-plot of $\bar{h}$ versus particle diameter ($\bar{d}_p$), for a constant flow-rate parameter and at a constant pressure. The inset in Figure 16 shows a cross-plot of $\bar{h}$ versus system pressure (P) for three particle sizes, at the same constant value of the flow-rate parameter.

It is seen that the parameters of particle size and operating pressure both have significant effects on the magnitude of the average heat transfer coefficient. In general, $\bar{h}$ increases with decreasing particle size or increasing system pressure. The strong decrease in the magnitude of $\bar{h}$ with increasing particle size is clearly evident in both figures. The effect of system pressure over the range of 405.3 kPa tested, is shown in the inset. While $\bar{h}$ increases slightly with pressure for the larger particles (950 μm), it changes little for the medium size particles (610 μm). With small particles (245 μm), there is a marked increase in the average coefficient for a change in pressure from 101.3 kPa to 202.6 kPa, but little change with further increase to 405.3 kPa. These rather complex trends would argue for a more mechanistic modeling of the heat transfer process in fluidized beds, rather than the conventional attempts to correlate $\bar{h}$ versus operating parameters ($\bar{d}_p$, P, U_{sg}, etc.).

Heat Transfer Results for Tube Bundle

As stated earlier, an instrumented tube was placed at two different positions within a ten-row, bare tube bundle for the measurement of local heat transfer coefficients. The two locations are indicated in the sketch shown in Figure 20. The locations of thermocouples used to measure bed temperature are also shown in the sketch. Data were obtained with glass particles denoted as SG (see Table 1) at a bed pressure of 101.3 kPa. These are listed in Table 7.

Figures 17 and 18 show polar plots of the local heat transfer coefficients measured at locations 1 and 2 within the bundle, respectively. For an internal tube (location 1), the coefficients were found to peak at an intermediate rather than at the highest gas flow rate. For the tube in the bottom-row of the bundle (location 2), the data bear a greater resemblance to the data obtained for a single horizontal tube. For both locations, the coefficients over the top portion of the tube were small for flow rates close to minimum fluidization conditions, but were substantially higher at larger values of the flow parameter. For moderate to high flow rates, the largest local coefficients were found at the top of the tube rather than at the side or bottom positions.

The local coefficients around the tube at two locations in the bundle are compared with those obtained around a single tube in the cylindrical bed (Figure 19). For the U_N parameter value of ~0.14, the coefficients for the internal tube within the bundle are seen to be slightly higher than those for the tube at the bottom-row and for the single tube.

The circumferentially averaged heat transfer coefficients ($\bar{h}$) for the two locations in the bundle are plotted in Figure 20 as a function of gas flow rate. For comparison, the average coefficients for a single horizontal tube in the cylindrical bed, with particles of about the same size, are also shown. The coefficients for each of the three configurations were found to exhibit similar trends. Moreover, the $\bar{h}$ values for the single tube are seen to be bounded by those for the bottom-row and inner-row tubes.

3.2 Comparisons of Heat Transfer Data with Existing Correlations

A survey of the literature indicated that correlations for local heat transfer coefficients have not been published to date.

An attempt was made to compare the average heat transfer coefficient ($\bar{h}$) obtained in this study with correlations proposed for heat transfer from single horizontal tubes. Comparisons were made with a few selected correlations which are well-known and find wide use. The three correlations examined are that of Vreedenberg [5], Gel'perin et al. [14], and modified Vreedenberg as proposed by Andeen and Glicksman [12]. The value of average bed void fraction ($\bar{\alpha}$) is required in these correlations. This quantity could have been measured experimentally during the test runs. However, in design applications, one would normally calculate $\bar{\alpha}$ by some standard correlation since it would not be known a priori. Consistent with this practice, the following equation of Staub and Canada [59] was used to calculate $\bar{\alpha}$ for use in the heat transfer correlations.

$$\frac{U_{sg}}{\bar{\alpha}} = c_o U_{sg} + \frac{(1-\bar{\alpha}_{mf})}{\bar{\alpha}_{mf}} U_{mf} \tag{2}$$

where c_o is termed a distribution parameter or slope of velocity plot. The value of c_o shows a weak dependence on particle size and operating pressure. Based on data for particle sizes of 650 µm and 2600 µm and at pressures of 101.3, 506.5 and 1013 kPa, Staub and Canada suggest a median value of 1.05 for c_o when the gas velocity (U_{sg}/U_t) does not exceed 0.55. The value of $\bar{\alpha}$ at minimum fluidization $(\bar{\alpha}_{mf})$ was computed from a relation given by Leva et al. [60]

$$\frac{0.005\ \psi_s^2 \bar{\alpha}_{mf}^3}{(1-\bar{\alpha}_{mf})} = 0.0007\ Re_{mf}^{-0.0625} \qquad \text{for } Re_{mf}<5.0 \tag{3}$$

In cases where Re_{mf} exceeds 5.0, a value of 0.40 was assigned to $\bar{\alpha}_{mf}$, in the absence of a more accurate relationship.

Vreedenberg's Correlation

Vreedenberg [5] proposed the following correlation

$$\left(\frac{\bar{h}D}{k_g}\right) = 0.66 \left(\frac{c_{ps}\mu_g}{k_g}\right)^{0.3} \left[\left(\frac{GD\rho_s}{\rho_g\mu_g}\right) \frac{(1-\bar{\alpha})}{\bar{\alpha}}\right]^{0.44}$$

$$\text{for } Re_G < 2050 \tag{4}$$

$$\left(\frac{\bar{h}D}{k_g}\right) = 420 \left(\frac{c_{ps}\mu_g}{k_g}\right)^{0.3} \left[\left(\frac{GD\rho_s}{\rho_g\mu_g}\right) \left(\frac{\mu_g^2}{\bar{d}_p^3\rho_s^2 g}\right)\right]^{0.3}$$

$$\text{for } Re_G > 2550 \tag{5}$$

An arithmetic average of $\bar{h}$ calculated from these two equations is recommended for $2050 < Re_G < 2550$.

In order to encompass all the data in one graph, the results are plotted in terms of the coordinates ($Nu_{exptal}/Nu_{Vreedenburg}$) and Re. Comparison of data with correlation is shown in Figure 21. The predictions are unsatisfactory, with rather large deviations from the experimental data. Examination of numerical results show the disagreement to be especially pronounced for either small particles ($\bar{d}_p$ of 125 μm, 245 μm) or for large particles ($\bar{d}_p$ of 1580 μm).

Correlation of Gel'perin et al.

Gel'perin et al. [14] proposed a correlation of the form

$$\left[Nu \frac{\bar{\alpha}}{6(1-\bar{\alpha})} \right] = 0.73 \left[\frac{Re}{6(1-\bar{\alpha})} \right]^{0.32} \tag{6}$$

The experimental data plotted in terms of the parameters ($Nu_{expt}/Nu_{Gel'perin}$) and Re are shown in Figure 22. Again, the correlation turns out to be unsatisfactory, with a general tendency to overpredict the data. However, for large particles this correlation seems to be in better agreement with these data than the other two correlations.

Modified Vreedenberg's Correlation

Andeen and Glicksman [12] have suggested a modified form of Vreedenberg's correlation

$$\left[\frac{(\bar{h}D/k_g)}{(1-\bar{\alpha})Pr^{0.3}}\right] = 900 \left[\left(\frac{GD\rho_s}{\rho_g \mu_g}\right)\left(\frac{\mu_g^2}{\bar{d}_p^3 \rho_s^2 g}\right)\right]^{0.326}$$

$$\text{for } Re_G > 2550 \qquad (7)$$

Figure 23 compares the data with this correlation. It is observed that a consistent and significant underprediction exists. Examination of Figures 21 and 23 also indicates that the modified equation does not fare any better than the correlation proposed by Vreedenberg.

Thus, the conventional approach of relating heat transfer coefficients and operating parameters by means of empirical correlations seems to be inadequate. The complex trend found for the variation of local heat transfer coefficients with variations in circumferential position, particle size, gas flow rate, and system pressure indicates a need for mechanistic modeling of the heat transfer process.

3.3 Fluidization Data

As stated earlier, the capacitance probe was used to measure transient bed-surface contact behavior. The capacitance sensed by the probe is proportional to the dielectric constant of the fluidized medium local to the probe electrodes. The dielectric constant in turn depends on the local void fraction. Thus, a capacitance trace versus time can be directly related to the variations in local solids density at the tube surface. The measured capacitance signals were calibrated relative to an upper bound corresponding to the capacitance measured when the probe is immersed in a loosely packed static bed of particles, and a lower bound corresponding to the capacitance sensed when the probe is fully exposed to air. The intermediate capacitances measured in the fluidized conditions were normalized with respect to these two limits such that a value of 1.0 represents a state identical to a loosely packed static bed and a value of zero corresponds to that of a gas void. It is assumed that intermediate values are directly proportional to the local void fraction.

Examples of typical capacitance signals obtained with an instrumented horizontal tube immersed in a fluidized bed of small particles ($\bar{d}_p = 245$ μm) are shown in Figures 24 and 25. These data were obtained for fluidization at atmospheric pressure. From Figure 24 it is seen that at low gas flow rates, the top surface of the tube remains covered by a stagnant cap of densely packed particles with very long contact times and no apparent displacement by passing bubbles. One would expect that in this regime heat transfer would be dominated by conductive transfer with some enhancement due to ventilation flow of gas through the interstitial spaces. At the sides of the tube, a renewal type of contact with distinct periodic variations in the emulsion density is found. Another distinctly different behavior is observed at the bottom of the tube. The capacitance traces showed that this segment encountered a relatively light density emulsion with little fluctuation in the instantaneous density. One would expect that for this flow regime a dilute phase convective transport mechanism would be appropriate.

The qualitative behavior outlined above undergoes a change with the operating conditions, as can be seen, for instance in Figure 25. With an increase in the gas flow rate, the top of the tube experiences increasingly more effective scrubbing by passing bubbles until the stagnant cap is periodically replaced by packets of particles. The sides of the tube encounter more and more of lean phase, while the bottom portion of the tube experiences renewal type of contact with the dense-phase contribution becoming important. The observations of this section are consistent with those reported in [51, 56-58].

In order to quantitatively describe the measured fluidization characteristics, it was decided to differentiate between a "dense phase" and a "lean phase" contact at the tube surface. This binary classification required that a suitable criterion be selected as a demarcation between the two phases. Three different criteria based on normalized capacitance signals of 1/3, 1/2 and 2/3 (corresponding to average void fractions of 0.8, 0.7 and 0.6) were used in an attempt to find a suitable criterion. The first criterion (1/3; void fraction of 0.8) was found to give the most consistently meaningful interpretation of the contact characteristics. Besides, the observations of [17, 61] lend support to the choice of 0.8 as a cut-off value for the void fraction. At this value of bed voidage, the gas phase is said to become continuous i.e. bubbles disappear according to [17], while the flow is considered to be disperse by [16] for average bed void fractions exceeding 0.8. The details of the analysis of the capacitance signal are presented in Appendix A.

Using the procedure cited above, it was possible to determine the contact residence times (θ_D,θ_L) of the dense and the lean phases at the probe surface, as indicated in Figure 62. For data obtained over sufficiently long sample times, it was also possible to compute the average void fractions of the dense and the lean phases (α_D,α_L). Likewise, the fraction of the total time exposed to each phase (f_L, $1-f_L$) could be determined. It is shown in Chapter 4 that the value of a quantity termed "root-square-average residence time of the dense phase" ($\bar{\theta}_D$) is required as input for model prediction. Hence, this quantity was computed from residence time (θ_D) data for each test run, as detailed in Appendix A.

The fluidization data ($\bar{\theta}_D$, f_L, α_D, α_L) obtained in this investigation are furnished in Tables 8 through 13.

Fluidization Data for a Single Tube

The plots of the fluidization parameters $\bar{\theta}_D$, f_L, α_D, and α_L as functions of the normalized velocity parameter (U_N), for three angular positions ($\beta = 0°$, 90° and 180°), are shown in Figures 26 through 29. The data shown were obtained with a medium size particle (GT-3) and at a system pressure of

202.6 kPa. From Figure 26, it is seen that the top of the tube ($\beta = 0°$) is initially in contact with a stagnant cap of densely packed particles. With an increase in gas flow rate beyond the minimum fluidization condition, this cap is increasingly disturbed by bubbles passing nearby. Thus, renewal type mechanism gradually sets in and diminishes $\bar{\theta}_D$. At the sides and bottom of the tube, the surface renewal mechanism controls and $\bar{\theta}_D$ does not exhibit any dramatic change over the tested flow rate range. At the top of the tube, f_L increases continuously from a value of zero at minimum fluidization, as shown in Figure 27. At the sides of the tube, initially with an increase in the gas flow rate, more lean phase comes into contact with the tube surface. This is probably due to increased bubble-activity. With further increase in the flow rate, f_L at first decreases due to enhanced particulate loading and particle circulation; but later with the onset of slug flow regime, f_L shows an increasing trend. The bottom of the tube exhibits a variation in f_L somewhat analogous to that at the sides of the tube, but the changes are less pronounced at this location.

Near minimum fluidization conditions, the cap at the top of the tube remains unfluidized and so the dense-phase void fraction (α_D) has a value close to that of a packed bed (Figure 28). It increases rapidly at first and more slowly later with increments in U_N. The value of α_D at the sides of the tube is rather high (0.7-0.8), but it does not undergo any significant change over the flow rate range. With an increase in the gas flow rate, α_D decreases at the bottom of the tube from a value of 0.8 at minimum fluidization conditions. This is due to increased particulate loading and bubble-induced circulation. As the transition from bubbly to slug flow regime occurs, α_D at the bottom of the tube recovers and begins to increase with flow rate. From Figure 29, it is seen that the lean phase void fraction (α_L) at the top of the tube has a value of 0.8 at U_{mf}; this is because no lean phase contact occurs at minimum fluidization conditions. α_L rises rapidly in the bubbly flow regime and increases more slowly with further increments in the gas flow rate. At the sides and bottom of the tube, the changes in α_L are less pronounced.

The effect of system pressure on the fluidization parameters is exhibited for a small size particle (GT-2) in Figures 30 through 33, and for a large size particle (GT-6) in Figures 34 through 37. From Figure 30, it is seen that $\bar{\theta}_D$ values at 405.3 kPa are generally lower than those at 101.3 kPa for all three angular positions ($\beta = 0°$, 90° and 180°), except at low values of U_N. The change in $\bar{\theta}_D$ due to pressure is especially pronounced for the top location ($\beta = 0°$), with higher residence times at low values of U_N and much lower contact times at other U_N values. At atmospheric pressure, the $\bar{\theta}_D$ values for the three angular positions are distinctly different from one another. But at 405.3 kPa, the residence time ($\bar{\theta}_D$) distribution tends to become uniform around the tube for reasonably large gas flow rates ($U_N > 0.25$). Figure 31 indicates that the values of f_L

at the elevated pressure are higher for the top location ($\beta = 0°$) and generally lower for the side position ($\beta = 90°$), as compared to those at atmospheric pressure. But the bottom location ($\beta = 180°$) exhibits a radically different behavior. At atmospheric pressure, contact with the lean phase occurs most of the time; but at 405.3 kPa, more dense phase contact occurs initially and the fractional contact time of the lean phase increases with gas flow rate. From Figure 32, it is seen that the values of α_D are generally higher and the dense phase is more loosely packed at the higher pressure, for both the top and side positions ($\beta = 0°$ and $90°$). But the bottom location experiences contact with a considerably denser medium at the higher pressure, especially at low gas flow rates. Figure 33 indicates that the lean phase is less dilute and the values of α_L are somewhat lower at 405.3 kPa, in contrast with the results at atmospheric pressure, for all three angular positions. Thus it seems that in the case of small particles (GT-3), the contributions of both the dense phase and the lean phase mechanisms to heat transfer increase with pressure. The dense phase contribution is enhanced by shorter contact times, while the increased lean phase contribution results primarily from the gas density scaling effect.

From Figures 34 through 37, it is seen that in the case of large particles (GT-6) the fluidization parameters are affected only to a small extent by pressure. Figure 34 indicates that $\bar{\theta}_D$ values are slightly lower at 405.3 kPa, for all three angular positions. More lean phase contact with the tube surface occurs (larger f_L values) at the higher pressure, for the top and bottom locations; very little change in f_L occurs at the side position (Figure 35). From Figures 36 and 37, it is apparent that pressure has little effect on the void fractions (α_D,α_L) over the flow rate range tested. Thus it seems that in the case of large particles (GT-6), the improvement in the local heat transfer coefficients with pressure occurs mainly due to the increment in the lean phase contribution. The enhanced lean phase transfer, in turn, is attributable to the gas density scaling effect. Hence, for large particles convective transport becomes more and more important with an increase in the operating pressure.

The effect of particle size ($\bar{d}_p$) on the fluidization parameters at atmospheric pressure is shown in Figures 38 through 41. Each plot corresponds to a velocity parameter (U_N) value of 0.10. Figure 38 indicates that particle size has a considerable influence on $\bar{\theta}_D$ for the top location ($\beta = 0°$). Surface renewal seems to occur more often at the top of the tube, for large particles rather than for small particles. This serves to explain the high degree of nonuniformity observed in the local heat transfer coefficient distribution around the tube, for small particles at low gas flow rates. The values of $\bar{\theta}_D$ for the side and bottom locations are little affected by particle size. The curve for the side position exhibits a decreasing trend, while that for the bottom location shows a rising characteristic. It is seen from Figure 39 that $\bar{d}_p$ has a sizable influence on f_L. For the top location, f_L steadily increases from almost 0 to 1 as the particles are changed from GT-2 to GT-6. The curves for the side and bottom positions exhibit increasing and decreasing trends respectively. Thus with an increase in particle size, the fractional contact time of the lean phase (f_L) increases for the top and side positions while dense phase fractional contact time increases for bottom location. Figure 40 indicates that with an increase in $\bar{d}_p$, the dense phase that comes into contact with the top and side positions is more dilute or loosely-packed; and the medium that contacts the bottom location is more dense. It is seen from Figure 41 that the void fraction of the lean phase (α_L) shows an increasing trend with particle size for all three angular positions. In summary, the values of the fluidization parameters ($\bar{\theta}_D$, f_L, α_D, α_L) are altered by particle size ($\bar{d}_p$); the nature and extent of the variation, however, depends on the angular position (β).

Fluidization Results for Tube Bundle

Fluidization data were obtained by placing an instrumented tube at two different positions within a ten-row bare-tube bundle (Figure 9). Measurements were obtained with glass particles SG (see Table 1) and at atmospheric pressure. The results are furnished in Tables 12 and 13.

The plots of $\bar{\theta}_D$, f_L, α_D and α_L as functions of normalized velocity, with angular position β as a parameter, are shown in Figures 42 through 45. The data pertain to location 2 in the tube array. For clarity, only the data points that correspond to the angular positions of $\beta = 45°$ and 90° are exhibited. In all cases, the curves drawn through the data points over the data span have been shown as solid lines and in the extrapolated region as dotted lines.

From Figure 42, it is apparent that just beyond minimum fluidization conditions, the top portion of the tube ($\beta = 0°$ and 45°) remains covered by a stagnant cap of densely packed particles. With an increase in gas flow rate, this cap is more increasingly disturbed by passing bubbles. Consequently, $\bar{\theta}_D$ diminishes and the renewal type mechanism gradually sets in. The bottom segment of the tube ($\beta = 135°$ and 180°) initially is in contact with a gas void and $\bar{\theta}_D$ evidently is zero. With a rise in gas flow, increased particulate loading and circulation occurs. The dense phase contribution and $\bar{\theta}_D$ increase steeply before slowly declining at very high velocities. At the sides of the tube, the renewal mechanism controls and $\bar{\theta}_D$ does not undergo any significant change over most of the flow range.

For $\beta = 0°$, 45° and 90°, f_L increases steadily from 0 to 1, as can be seen in Figure 43. At the bottom of the tube, near minimum fluidization velocity, only the lean phase is present, and hence f_L has a value of unity. With an increase in the gas flow rate, more dense phase comes into contact with the tube surface due to bubble-induced circulation and decreases f_L; but with the onset of slug flow regime, f_L starts to increase and approaches unity.

Near minimum fluidization conditions, the cap at the top of the tube ($\beta = 0°$ and 45°) remains unfluidized and so the dense-phase void fraction (α_D) has a value close to that of a packed bed (Figure 44). It approaches a value of 0.8--the reference level for cut-off between the phases--as the U_N parameter approaches unity. α_D decreases at the bottom of the tube with an increase in the gas flow rate from the minimum fluidization conditions, due to increased particulate loading and particulate circulation. As the transition from bubbly to slug flow regime occurs, α_D at the bottom of the tube recovers and should slowly approach ~0.8 at very high flow rates.

There is no lean phase present at the top of the tube at U_{mf} and so the void fraction α_L has a value of 0.8. With an increase in gas flow rate, α_L rises rapidly in the bubbly flow regime, as shown in Figure 45. At the sides and bottom of the tube, the change in α_L is not pronounced. But in all the cases, α_L approaches unity as the U_N parameter tends to 1, as required by physical considerations.

The family of curves indicate that the fluidization behavior is complex in the bubbly flow regime but becomes more ordered in the slug and turbulent flow regimes, as velocity is increased.

Fluidization data-sets obtained at location 1 (Row 3) within the tube bundle were complete for β values of 0°, 45°, and 90° and incomplete for 135° angular position. No data were obtained at the bottom position ($\beta = 180°$) owing to probe failure.

The parameters $\bar{\theta}_D$ and f_L obtained for both locations at a U_N value of 0.069 are shown in Figure 46. It is seen that for the top portion of the tube at location 1, the $\bar{\theta}_D$ values are lower and the f_L values somewhat higher than those for the tube at location 2. This indicates more effective scrubbing by passing bubbles and in turn more frequent surface renewal at the inner-row position. At the sides and bottom of the tube, $\bar{\theta}_D$ values are slightly higher and the f_L values are lower for location 1 as compared to those for location 2. This denotes increased dense phase contact with the tube at the inner-row position.

The void fractions of the dense phase (α_D) and the lean phase (α_L) assume values that are comparable for both locations (Tables 12 and 13). Thus at all angular positions (β), the dense phase contribution is relatively larger for the internal tube (location 1) as compared to that for the tube in the bottom-row (location 2).

4. PHENOMENOLOGICAL MODEL

4.1 Formulation

It is apparent from capacitance probe measurements (Section 3.3) that the surface could experience alternating contact with a dense emulsion phase and a lean void phase. The criterion for demarcation between the dense and the lean phases is somewhat arbitrary, but the dense phase is envisaged as a fairly close-packed matrix of solid particles ($\alpha_D \sim 0.4$ to 0.8) and the lean phase is regarded as a gaseous medium with some entrained particles ($\alpha_L \sim 0.8$ to 1.0). If the contribution due to radiation is negligible, the local heat flux at the tube surface can be written as

$$q = q_L + q_D \tag{8}$$

where

q_L = heat flux during lean phase contact
q_D = heat flux during dense phase contact

The local heat transfer coefficient (h) can then be expressed as a weighted average of the dense and the lean phase transfer coefficients,

$$h = f_L h_L + (1-f_L)h_D \tag{9}$$

where

f_L = fraction of the total time the lean phase is in contact with the surface

h_L = effective heat transfer coefficient in the lean phase

h_D = effective heat transfer coefficient in the dense phase

It is now necessary to derive relations for the transport coefficients in each phase. It is suggested that lean-phase heat transfer occurs primarily by turbulent convection and dense-phase heat transfer by transient conduction due to surface renewal. As discussed in the previous section, the dense phase contribution is significant at low gas flow rates and for small particles. The lean phase contribution becomes more and more important at high gas flow rates, for large particles and for elevated pressure operation.

4.2 Dense-phase Heat Transfer

When dense phase contact of the renewal type occurs at the exchange surface, heat is transferred by unsteady state conduction. However, for very long residence times the process becomes one of steady state; the fluid flowing through the interstices between particles acts as the transfer medium and finite heat transfer results due to the ventilation effect. It is now postulated that the effective heat transfer coefficient in the dense phase (h_D) can be expressed in terms of two components, one due to surface renewal of a medium with stagnant fluid (h_s) and the other due to fluid flow (h_f):

$$h_D = h_s + h_f \tag{10}$$

The well-known packet theory [26,27,36] can be used to estimate the unsteady state component:

$$h_s = 2\sqrt{\frac{k_e C_{pe}}{\pi \bar{\theta}_D}} \tag{11}$$

for constant wall temperature boundary condition. Here, k_e and C_{pe} are respectively the thermal conductivity and the volumetric specific heat of the two-phase medium that contacts the surface. $\bar{\theta}_D$ is the "root-square-average" residence time of the dense-phase packets. Over I occurrences of dense-phase contact (I packets), each with a different residence time of θ_{D_i}, the root-square-average residence time is defined as

$$\bar{\theta}_D \equiv \left[\frac{\sum_{i=1}^{I} \theta_{D_i}}{\sum_{i=1}^{I} \sqrt{\theta_{D_i}}}\right]^2$$

It has been shown in [36,49] that the above root-square-average is the correct mean to use for the effective residence time. The expression given for h_s (equation 11) corresponds to the case of constant wall temperature. But in practice, the physical condition lies in between constant wall heat flux and constant wall temperature, especially for low thermal capacity heaters.

The physical properties (k_e, C_{pe}) should correspond to effective values for the dense phase in the region adjacent to the heat transfer surface. For long residence times, where the heat wave penetrates several particle diameters deep into the medium, these properties can be assigned the "bulk" values for the dense phase:

$$k_D = k^\circ$$

$$C_{pD} = \rho_s(1-\alpha_D)c_{ps} + \rho_g\alpha_D c_{pg} \tag{12}$$

where

k° = thermal conductivity in a packed medium with motionless fluid

α_D = void fraction of the dense phase

k_D = thermal conductivity of the dense phase

C_{pD} = volumetric specific heat of the dense phase

ρ_s, c_{ps} = density and specific heat of the particles

ρ_g, c_{pg} = density and specific heat of the fluid

There exist several models for the determination of k° [15, 62-64]. The method proposed by Bauer and Schlünder [64] has been selected for use in this study, due to its versatility and its completeness. In addition to the particle and fluid thermal properties, it accounts for the influence of temperature, pressure, particle shape, size-distribution and porosity, oxide layer and finite contact surface area on the thermal conductivity of the two-phase medium. For closely-sized spherical particles and for operation at room temperature and gas pressure of 1 atmosphere or above, the thermal conductivity of the medium could be estimated from

$$k^{o} = k_g \left[\left(1 - \sqrt{1-\alpha_D}\right) + \sqrt{1-\alpha_D}\left(\frac{k'}{k_g}\right) \right] \tag{13}$$

with

$$\frac{k'}{k_g} = \frac{2}{\left(1 - B\frac{k_g}{k_s}\right)} \left[\frac{\left(1 - \frac{k_g}{k_s}\right) B}{\left(1 - B\frac{k_g}{k_s}\right)^2} \ln\left(\frac{k_s}{Bk_g}\right) - \left(\frac{B+1}{2}\right) - \frac{(B-1)}{\left(1 - B\frac{k_g}{k_s}\right)} \right]$$

and

$$B = 1.25 \left(\frac{1-\alpha_D}{\alpha_D}\right)^{10/9}$$

where k_g and k_s are the thermal conductivities of the gas and the solid respectively.

For cases of short residence times where the Fourier modulus is small $[F_o \equiv (k_D\bar{\theta}_D/C_{pD}\bar{d}_p^2) < 1]$, the effective zone for transient conduction in the dense phase is of the order of a fraction of a particle-diameter in depth. Since it is known that in the first particle layer the local void fraction is greater than α_D [35, 36, 65, 66], the effective values k_e and C_{pe} ought to be less than the respective bulk values k_D and C_{pD}. It is suggested that simple correction factors c_1 and c_2 be used to account for this effect:

$$\begin{aligned} k_e &= c_1 \cdot k_D \\ C_{pe} &= c_2 \cdot C_{pD} \end{aligned} \tag{14}$$

where c_1 and c_2 are expected to be bounded in magnitude between 0 and 1. The values of these two factors would depend upon the parameters that influence the penetration depth. Thus, c_1 and c_2 are likely to vary with the Fourier modulus and the conductivity ratio (k_D/k_g); they ought to have the following limits, based on physical considerations

$$\lim_{F_o \to 0} c_i = 0 \qquad \text{for } i = 1,2 \qquad \lim_{F_o \to \infty} c_i = 1 \tag{15}$$

By substituting relations (14) in equation (11) and defining an effective correction factor $(C \equiv \sqrt{c_1 \cdot c_2})$, the following relation is obtained

$$h_s = 2C\sqrt{\frac{k_D C_{pD}}{\pi \bar{\theta}_D}} \tag{16}$$

Thus, the transient conduction component (h_s) could be evaluated by multiplying the packet theory limit solution with a correction factor (C).

It is now necessary to determine the functional dependence of C on F_o and (k_D/k_g). This is accomplished by matching the solution (16) with a theoretical solution. The latter is obtained by solving the governing equations for transient conduction into the dense phase by a numerical scheme. The details of problem formulation and solution procedure are given in Appendix B. Herein, the concept of property boundary layer, proposed by Kubie and Broughton [35], has been employed to account for the wall effect. Numerical solutions were obtained, as a function of Fourier modulus (F_o), for seven different values of the conductivity ratio ($k_D/k_g = 1.4$, 2.21, 4.0, 6.03, 11.0, 20.0 and 34.7). Figure 47 shows the variation of Nusselt number ($Nu_s' = h_s'\bar{d}_p/k_D$) with Fourier modulus ($F_o$) for three different solid-fluid combinations--slag spheres/helium ($k_D/k_g = 2.21$), glass beads/air ($k_D/k_g = 6.03$) and steel shots/freon-12 ($k_D/k_g = 20.0$). The limit solution obtained from the packet theory is also included. It is seen that the numerical solutions approach the limit solution for large values of the Fourier number ($F_o > 100$), but depart appreciably from the limit solution at small values of F_o (<1). Also the extent of deviation increases with the conductivity ratio (k_D/k_g). The numerical solutions obtained in this investigation exhibit trends that are in general agreement with those reported by Kubie and Broughton [35]. The variation of the correction factor (C), determined by matching the solution (16) with the numerical solution, is shown in Figure 48. It is seen that C increases with increasing F_o and approaches 0 and 1 in the limits of zero and infinite F_o respectively. Also, for a given Fourier number larger values of C are obtained for smaller conductivity ratios. The ensuing correlation was obtained for Ċ by regression analysis,

$$C = \exp\left[-\frac{a_1}{F_o^{\,a_2 + a_3 \ln F_o}}\right] \tag{17}$$

with

$a_1 = 0.213 + 0.117\ w + 0.041\ w^2$

$a_2 = 0.398 - 0.049\ w$

$a_3 = 0.022 - 0.003\ w$

$w = \ell n\ (k_D/k_g)$

$F_o = k_D\bar{\theta}_D/C_{pD}\bar{d}_p^2$

It was earlier seen in Chapter 3 that near minimum fluidization conditions, the top surface of the tube remains covered by a stagnant cap of densely packed particles with very long contact times. The unsteady state component would approach zero for this case, whereas heat transfer measurements indicate a small but finite value for the local heat transfer coefficient. This may be attributed to the effect of fluid flow, as outlined earlier. Since the two-phase theory of fluidization [67] indicates that the dense phase could be considered as an emulsion at the incipiently fluidized state, it is proposed that the component h_f that accounts for the ventilation effect approach the following limits

$$\lim_{F_o \to 0} h_f = 0 \qquad\qquad (18)$$

$$\lim_{F_o \to \infty} h_f = h_{mf}$$

where

h_{mf} = heat transfer coefficient at minimum fluidization condition for no replacement

The ventilation effect is visualized as a secondary process and heat transfer is envisaged to occur from the particles to the fluid by convection. This prompts the use of a weighting factor that depends on the depth of heat penetration. By using a simple relation for the weighting factor that approaches the limits given by equation (18), h_f is expressed as

$$h_f = \left[1 - \exp\left(-\frac{x_p}{\bar{d}_p}\right)\right] h_{mf} \tag{19}$$

where

x_p = the depth of heat penetration

If x_p is defined as the depth at which the normalized temperature difference $[(T-T_B)/(T_w-T_B)]$ attains a value of 0.01, the use of semi-infinite layer approximation yields

$$x_p/\bar{d}_p \simeq 3.6\sqrt{F_o} \tag{20}$$

Here, the effect of conductivity ratio (k_D/k_g) on the penetration depth is disregarded, for the sake of simplicity.

Some data and correlations for h_{mf} are reported in the literature for vertical tubes. These however cannot be used in equation (19), because the fluidization data obtained in this investigation (Section 3.3) indicate packet renewal and lean phase contact to occur at the sides of the tube ($\beta = 90°$) near minimum fluidization conditions. Hence, as a first approximation, the values of the local heat transfer coefficient (Section 3.1) obtained for the top location ($\beta = 0°$) have been used to derive a curve-fit relation (Figure 49)

$$\frac{h_{mf}D}{k_g} = 0.26\ Ar^{0.31} \tag{21}$$

where

Ar = Archimedes number = $\bar{d}_p^3 g \rho_g (\rho_s - \rho_g)/\mu_g^2$

D = Diameter of the tube

Thus, the effective heat transfer coefficient in the dense phase (h_D) could be estimated by using equations (10), (12), (13), (16), (17), (19), (20) and (21).

4.3 Lean-phase Heat Transfer

Heat transfer during lean phase contact is hypothesized to occur by turbulent convection. The lean phase is conceptually visualized as a dilute mixture of entrained solid particles in gas. It is stipulated that the heat transfer process between this flowing lean mixture and the tube surface could be considered similar to that of solid-gas mixtures in pneumatic transport.

Data and correlations for heat transfer coefficient have been reported in the literature [68-74] for the flow of gas-solid suspensions in pipes. The equations are in general of the form

$$\frac{h_L}{h_g} = f\left(\frac{G_s}{G_g}, \frac{c_{ps}}{c_{pg}}\right) \tag{22}$$

where

h_L = heat transfer coefficient for gas-solid flow

h_g = heat transfer coefficient for gas flow alone

G_s, G_g = superficial mass velocities of solid and gas respectively

c_{ps}, c_{pg} = specific heat of solid and gas respectively

The quantity G_s/G_g is usually termed as solids mass loading ratio.

Depew and Kramer [71] attribute the improvement in heat transfer to the reduction in the thickness of the viscous sublayer and the increase in the volumetric specific heat of the flow. Shrayber [72] claims the higher heat transfer coefficient to result primarily from transverse particle migration. The mechanism that causes transverse migration is said to be eddy diffusion in the case of moderate size particles (~30 to 500 μm @ ρ_s/ρ_g ~ 1000) and collisions in the case of large particles. The presence of particles tends to distort the velocity field of the gas stream and the solids seem to affect the flow structure near the wall in a complex manner [73]. It is possible to carry out an analysis if the velocity field and the shear stress at the boundary of gas-solid flow are known [71,74]. Such treatment, however, becomes elusive for cylinders in cross-flow due to the occurrence of boundary layer separation. Hence a semi-empirical approach is indicated. Some investigators [61, 70,73] have advocated the use of a relation of the form

$$\frac{h_L}{h_g} = f(1 + E\,\frac{G_s}{G_g}\,\frac{c_{ps}}{c_{pg}}) \qquad (23)$$

where E is a coefficient that depends on system parameters

This expression is obtained by employing Reynolds' analogy and hence is valid for the flow of fluids with a Prandtl number (Pr) of unity. Since gases in general have a value of Pr close to 1.0, this relation could be applied to gas-solid flows.

For lean phase flow along the heat transfer surface, in a local sense, the ensuing equation can be written

$$\frac{G_s}{G_g} = \frac{\rho_s U'_{ss}}{\rho_g U'_{sg}} = \left(\frac{\rho_s}{\rho_g}\right)\left(\frac{1-\alpha_L}{\alpha_L}\right)\left(\frac{U_{rs}}{U_{rg}}\right)$$

$$= \left(\frac{\rho_s}{\rho_g}\right)\left(\frac{1-\alpha_L}{\alpha_L}\right)\left(\frac{1}{S}\right) \qquad (24)$$

where

U'_{ss}, U'_{sg} = local superficial velocities of solid and gas respectively

U_{rs}, U_{rg} = real velocities of solid and gas respectively

$S = (U_{rg}/U_{rs})$ = slip parameter

Substitution of equation (24) in (23) yields

$$\frac{h_L}{h_g} = f\left[1 + F\left(\frac{\rho_s}{\rho_g}\right)\left(\frac{1-\alpha_L}{\alpha_L}\right)\left(\frac{c_{ps}}{c_{pg}}\right)\right] \qquad (25)$$

where

$$F \equiv E/S$$

The parameter F should ideally account for slip between the phases, make allowance for the effect of solids on the velocity field in the vicinity of the tube surface, and incorporate the influence of particles on the eddy diffusivities for heat (ε_H) and momentum (ε_M). It is obvious that some basic studies need to be conducted in order to develop a relation for F. Due to lack of information, an empirical approach is adopted here.

It is known that particle transverse motion or the interaction of the particles with turbulent eddies near the wall is an important feature of the convective process. It is now postulated that for the most effective particle-fluid interaction in the transverse direction to occur, the particles ought to be in a state of mechanical equilibrium in the axial direction. Thus for vertical upward flow, the dynamic balance between inertia force and gravitational force becomes important. The relevant quantity then is a ratio of inertia force to gravitational force $[(\rho_g U_{sg}^2/\bar{d}_p)/g(\rho_s-\rho_g)]$. Since a net force in the direction of flow is likely to impair the interaction process, the quantity E can be expressed as

$$E = f\left[\left(\frac{g\bar{d}_p}{U_{sg}^2}\right)\left(\frac{\rho_s-\rho_g}{\rho_g}\right)\right] \tag{26}$$

where

g = acceleration due to gravity

It is now necessary to account for slip between the two phases. In gas-liquid flows, the density ratio (ρ_s/ρ_g) finds wide use in correlations for slip. Hence it seems reasonable to include the same ratio for gas-solid flows. In addition, it is suggested that the slip parameter (S) is likely to be influenced by the operating gas velocity (U_{sg}) and a characteristic particle velocity such as $\bar{U}_t$ (free-fall or terminal velocity for particle of size $\bar{d}_p$). It is anticipated that slip would be greater for larger values of the velocity ratio, ($\bar{U}_t/U_{sg}$). Thus, the ensuing relation can be written for the slip parameter

$$S = f\left[\left(\frac{\rho_s}{\rho_g}\right), \left(\frac{\bar{U}_t}{U_{sg}}\right)\right] \tag{27}$$

The parameter F then becomes

$$F \equiv \frac{E}{S} = f\left[\left(\frac{g\bar{d}_p}{U_{sg}^2}\right), \left(\frac{\rho_s-\rho_g}{\rho_g}\right), \left(\frac{\rho_g}{\rho_s}\right), \left(\frac{U_{sg}}{\bar{U}_t}\right)\right] \tag{28}$$

For gas-solid flows where $\rho_s >> \rho_g$, we can let

$$\frac{\rho_s-\rho_g}{\rho_g} \simeq \frac{\rho_s}{\rho_g}$$

Data obtained in this study that correspond to substantial lean phase contact indicate a satisfactory correlation with F, if it is expressed in the form

$$F = b_1 \left(\frac{g\bar{d}_p}{U_{sg}\bar{U}_t}\right)^{n_1} \tag{29}$$

where

b_1, n_1 = empirical constants

Incidentally, this form for F enables to correctly predict the variation of (h_L/h_g) with particle size $(\bar{d}_p)$ and Reynolds number (Re), as reported in the literature for gas-solid flow through pipes [68-74].

Ideally, in computing h_L by equation (25) for different circumferential positions (β), the local values of h_g for the corresponding locations around the tube should be used. But due to lack of sufficient <u>local</u> information for single phase flow, the value of circumferentially-averaged heat transfer coefficient has to be used instead. Thus, the heat transfer coefficient for gas flow alone (h_g) is estimated from standard correlations for single-phase flow across tubes

$$\left(\frac{h_g D}{k_g}\right) = b_2 \left(\frac{\rho_g U_{gm} D}{\mu_g}\right)^{n_2} (Pr)^{1/3} \tag{30}$$

where

U_{gm} = gas velocity based on minimum flow area

The constants b_2 and n_2 for single tube configuration have been taken from [75] and for the case of ten-row bare tube bundle from [76].

A correlation for (h_L/h_g) can now be obtained through regression analysis, by using paired curve-fit values from local heat transfer and local fluidization measurements. Due to lack of adequate data that pertain to mostly lean phase contact, data that correspond to f_L values larger than 0.4 have been used to derive a correlation. The procedure employed was as follows:

i) with curve-fit values of $\bar{\theta}_D$ and α_D, calculate the dense phase heat transfer coefficient (h_D) by equations given in Section 4.2;

ii) with curve-fit values of the local heat transfer coefficient (h) and the fraction of the total time that lean phase is in contact (f_L), compute the lean phase heat transfer coefficient (h_L) by equation (9);

iii) calculate h_g by equation (30) and then the value of (h_L/h_g);

iv) using the values of α_L, U_N and the physical properties, evaluate the quantities,

$$x_1 = \left(\frac{g\bar{d}_p}{U_{sg}\bar{U}_t}\right) \quad \text{and} \quad x_2 = \left(\frac{\rho_s}{\rho_g}\right)\left(\frac{1-\alpha_L}{\alpha_L}\right)\left(\frac{c_{ps}}{c_{pg}}\right) \quad ;$$

v) by means of regression analysis, determine the relationship between (h_L/h_g), x_1 and x_2 in the manner of equation (25).

A satisfactory curve-fit was obtained (multiple correlation coefficient of ~0.7 for 302 data points) with the relation

$$\frac{h_L}{h_g} = \left[1 + 194.0 \left(\frac{g\bar{d}_p}{U_{sg}\bar{U}_t}\right)\left(\frac{\rho_s}{\rho_g}\right)\left(\frac{1-\alpha_L}{\alpha_L}\right)\left(\frac{c_{ps}}{c_{pg}}\right)\right]^{0.5} = X^{0.5} \qquad (31)$$

if we let

$$X = 1 + 194.0 \left(\frac{g\bar{d}_p}{U_{sg}\bar{U}_t}\right)\left(\frac{\rho_s}{\rho_g}\right)\left(\frac{1-\alpha_L}{\alpha_L}\right)\left(\frac{c_{ps}}{c_{pg}}\right)$$

Figure 50 indicates the degree of correlation between this equation and data. Different symbols have been used to represent data that correspond to different angular positions (β).

4.4 Comparison of Model Predictions with Experimental Data

Local Heat Transfer Coefficients

Using curve-fit values of the experimentally determined fluidization parameters ($\bar{\theta}_D$, f_L, α_D, α_L), it was possible to compute local heat transfer coefficients by the proposed model. A sample calculation is shown in Appendix C for illustrative purposes. Comparisons of the predicted local coefficients with those measured experimentally are shown in Figures 51 through 54.

Figures 51 and 52 show plots of the local coefficients for three angular positions ($\beta = 0°$, $90°$ and $180°$) as a function of gas flow rate (U_N). Figure 51 provides the comparison for GT-2 particle ($\bar{d}_p = 245$ μm) at atmospheric pressure, while Figure 52 indicates the results for GT-5 particle ($\bar{d}_p = 950$ μm) at a system pressure of 202.6 kPa. General agreement is found between the calculated values (points) and the experimental data (curve). It is seen that at low gas flow rates ($U_N < 0.1$), the predicted values tend to be lower than the experimentally measured coefficients; but at higher flow rates, the coefficients show good agreement. In particular, the model successfully predicts the trends exhibited by the experimentally measured local heat transfer coefficients. It is noteworthy that the proposed model makes satisfactory predictions despite the changes in fluidization dynamics with circumferential position (β), gas flow rate, particle size ($\bar{d}_p$) and system pressure (P).

Figure 53 presents the results obtained in a ten-row bare tube bundle with SG particles ($\bar{d}_p = 650$ μm) and at atmospheric pressure. It is seen that the model is able to predict the variation in the local heat transfer coefficient (h) with circumferential position (β) reasonably well.

The results plotted in terms of the coordinates (h_{expt}/h_{pred}) and Re are shown in Figure 54. Different symbols represent data that correspond to different angular positions (β). The plot includes both single tube and tube bundle data and covers a wide range of test conditions, as indicated in the figure (546 data points). It is observed that the model is able to successfully predict the variation in the local heat transfer coefficient with circumferential position, gas flow rate, particle size and system pressure. This result seems to verify the basic mechanisms and their interrelationship as proposed in the phenomenological model.

In particular, it appears that the concepts of a dense-phase and a lean-phase transfer mechanism, with each mechanism playing a dominant role at different test conditions can in fact represent the heat transfer process.

In Section 3.3 it was pointed out that the contributions from and the relative importance of the two transfer mechanisms change appreciably with variations in the test conditions. Herein the effect of system parameters on the individual contributions is examined. Figures 55, 56 and 57 indicate the influence of operating pressure on the effective heat transfer coefficients in the dense phase (h_D) and in the lean phase (h_L). Figure 55 presents the results obtained at the top of the tube ($\beta = 0°$), with small particles ($\bar{d}_p = 245$ μm) and at a U_N parameter value of 0.24. It is evident that the dense-phase transient conduction mechanism predominates in this case. Although both h_D and h_L exhibit increasing trends, it is the dense-phase coefficient that changes significantly with pressure (P) and thereby increases the local heat transfer coefficient (h). The h_D and h_L values computed for the side location ($\beta = 90°$) are shown in Figure 56, for the case of large particles ($\bar{d}_p = 950$ μm) and at a normalized velocity of 0.20. The dense-phase coefficient exhibits a decreasing trend, whereas the lean-phase coefficient shows a rising characteristic. At atmospheric pressure, the two coefficients are comparable in magnitude with a slightly higher value for h_D. This disposition quickly reverses with an increase in pressure, and the value of

h_L becomes increasingly greater than that of h_D. Thus the lean-phase convective mechanism provides the basis for the improvement in the local heat transfer coefficient (h) with pressure. Another distinctly different behavior is observed at the bottom of the tube (Figure 57). The data correspond to medium size particles ($\bar{d}_p = 610$ μm) and a flow-rate parameter value of 0.23. It is seen that the values of h_D are considerably higher than those of h_L. But the dense-phase coefficient shows little change, while the lean-phase coefficient increases with pressure. The end result is a slight increment in h with pressure. In this manner, the two transfer coefficients (h_D and h_L) change both in magnitude and in their relative importance to provide the variation in the local heat transfer coefficient (h) with test parameters.

Average Heat Transfer Coefficients

From the local heat transfer coefficients (h) calculated in the manner outlined in the previous subsection, it was simple to compute the circumferentially averaged heat transfer coefficients ($\bar{h}$). The model predictions are compared with experimentally determined average coefficients in Figures 58 through 61.

Figure 58 provides a comparison of the results for three different particle sizes at atmospheric pressure. It is seen that there is general agreement between the calculated values (points) and the experimental data (curve). There is a tendency for the model to underpredict the heat transfer coefficients for small ($\bar{d}_p = 245$ μm) and medium size ($\bar{d}_p = 610$ μm) particles at low velocities. This discrepancy has been noticed before (previous subsection) and generally occurs in instances when the dense-phase conduction mechanism prevails. It seems that the deviation probably results from a mismatch in the wall boundary condition. The calculated coefficients are based on constant wall temperature boundary condition; but the measurements are likely to correspond to a physical condition somewhere between constant heat flux and constant temperature at the wall, due to the use of a low thermal capacity heat transfer probe. For the case of constant wall heat flux, the constant in equation (11) for the unsteady state component (h_S) would be $\sqrt{\pi}$, as opposed to $(2/\sqrt{\pi})$ for constant temperature boundary condition. Thus the use of an intermediate solution that corresponds to the actual physical situation is likely to provide better agreement between the model and the experimental data.

Figure 59 shows a plot of the average heat transfer coefficient ($\bar{h}$) versus particle size ($\bar{d}_p$) for a constant flow-rate parameter (U_N) and at a constant pressure (P). It is seen that the trend is well predicted and the deviation between calculated and measured coefficients is generally less than 10 percent.

Using the extrapolated correlation curves shown in Figures 42-45 for the fluidization parameters ($\bar{\theta}_D$, f_L, α_D, α_L), it was possible to calculate the average heat transfer coefficients ($\bar{h}$) beyond the range over which actual experimental measurements were obtained. The curve predicted thus for SG particles

($\bar{d}_p = 650\ \mu m$) at atmospheric pressure is shown in Figure 60. Also included in this figure are points representing experimentally measured $\bar{h}$ obtained with both General Electric Company's instrumented tube [77] (constant wall heat flux) and the instrumented test tube of this investigation (Section 2.2). These two sets of data were complementary in that the measurements obtained in this study were at low gas flow rates while the GE measurements [77] were at relatively high gas flow rates. It is seen that the model is able to predict the trend of the data reasonably well and shows fair agreement with both sets of data.

Figure 61 presents the data (145 data points) in terms of the coordinates ($\bar{h}_{expt}/\bar{h}_{pred}$) and Re. The plot includes both single tube and tube bundle results and serves to provide an overall evaluation of the model. Different particle sizes ($\bar{d}_p$) are identified by different symbols. It is seen that the proposed model is able to make satisfactory predictions despite the wide variation in the test parameters. Also an examination of Figures 21-23 and Figure 61 reveals that the proposed phenomenological model renders vastly improved predictions as compared to the empirical correlations.

5. CONCLUSIONS

Heat Transfer Characteristics

Local heat transfer coefficients around horizontal tubes in fluidized beds were found to be significantly different for different circumferential positions, particularly at low to moderate gas flow rates. The distribution of the local coefficients around the perimeter of the tube were found to be highly non-uniform for small particles ($\bar{d}_p = 125$ μm) but were relatively uniform for large particles ($\bar{d}_p = 1580$ μm). With an increase in gas flow rate beyond minimum fluidization conditions, the local coefficients were in general observed to increase at first, attain a maximum and then decrease with further increments in the flow rate. In addition, the magnitude of the local coefficients were affected by both particle size and system pressure. Likewise, the circumferentially averaged heat transfer coefficients were found to depend strongly upon these operating parameters. The average coefficients exhibited a generally increasing trend with decreasing particle size and increasing system pressure.

Some noticeable, though small, differences were found for heat transfer coefficients on tubes at different locations within a horizontal tube bundle. The results indicated a somewhat higher heat transfer coefficient for an internal tube within the bundle than for a tube in the bottom-row of the bundle. Coefficients obtained for a single tube, at comparable conditions, were seen to be bounded by the coefficients for these two positions in the tube bundle.

Comparisons of measured average coefficients with published correlations showed poor agreement, with deviations up to several hundred percent. Thus, the conventional approach of relating heat transfer coefficients and operating parameters by means of empirical correlations seemed to be inadequate. The complex trend observed for the variation of the local heat transfer coefficient with variations in angular position, gas flow rate, particle size, and system pressure strongly indicated a need for mechanistic modeling of the heat transfer process.

Fluidization Dynamics

Capacitance probe measurements on the surface of horizontal tubes showed that local bed-surface contact dynamics depend strongly upon gas flow rate and circumferential position. In general, it was observed that at flow rates close to minimum fluidization conditions, the top portion of the tube remains covered by a dense emulsion, the sides of the tube experience a renewal type of contact with alternating voids and dense packets, and the bottom portion of the tube tends to be continuously washed by a gaseous medium with some entrained particles. These circumferential differences were seen to diminish with increasing flow rate.

From the test results, the dense phase void fraction was found to vary from 0.4 to 0.8, while the lean phase void fraction was found to range from 0.8 to 1.0. In contrast, the values of the dense phase residence time and the fractional contact time of the lean phase were observed to vary significantly with gas flow rate and circumferential position. The data indicated that the contact characteristics are complex in the bubbly flow regime but become more ordered in the slug and turbulent flow regimes, as the flow rate is increased. In addition, the magnitude of the fluidization parameters were affected by both particle size and system pressure.

Capacitance data obtained with an instrumented tube at two different locations within a tube bundle indicated dense phase contact to occur more often for a tube at the inner-row position than for a tube in the bottom-row of the bundle.

Phenomenological Model

With a knowledge of the fluidization characteristics around horizontal tubes, a general model was developed for the local heat transfer coefficient based on combined dense phase and lean phase transfer mechanisms. Using empirical correlation curves for the fluidization parameters, the model was able to successfully predict both local and average heat transfer coefficients for a wide range of test conditions. The trends exhibited by the model predictions were also observed to be in general agreement with those found for the variation of the experimentally measured heat transfer coefficients with gas flow rate, particle size and system pressure.

The dense phase contribution was found to be significant at low gas flow rates and for small particles. The lean phase contribution seemed to become more and more important at high gas flow rates, for large particles and for elevated pressure operation. Effective heat transfer coefficients in the dense and in the lean phases were observed to change both in magnitude and in their relative importance to predict the correct variation in the local heat transfer coefficient with test parameters.

6. RECOMMENDATIONS

i. Local heat transfer and fluidization characteristics for horizontal tubes should be investigated at higher gas flow velocities ($U_N > 0.4$), with larger particles ($\bar{d}_p > 2000\ \mu m$), for particle mixtures, and in the free-board region of the fluidized bed.

ii. Some sample studies under hot bed conditions should be carried out in order to account for the effect of radiation and extend the cold model.

iii. To avoid poor heat transfer at the top and bottom portions of horizontal tubes, fluidized bed heat exchangers should typically operate at gas velocity (U_N) values greater than 0.05.

iv. The use of steam is indicated for reducing static charge effects on instrumentation. It is also suggested that the Techtran Cassette System be replaced by a 7-track Magnetic Tape Drive to facilitate faster data acquisition and to effect direct storage.

v. By acquiring additional data and by conducting some scoping studies, the correlation for the effective heat transfer coefficient in the lean phase (h_L) should be improved.

vi. More data should be obtained to develop general correlation functions for the fluidization parameters.

vii. Experiments should be carried out with different gas/solid combinations in order to fully verify the proposed heat transfer model.

Table 1 Properties of test particles

Designation	Mean Size $\bar{d}_p$(μm)	Size Range (μm)	U_{mf}(m/s)			U_t(m/s)		
			Pressure (kPa)			Pressure (kPa)		
			101.3	202.6	405.3	101.3	202.6	405.3
GT-1	125	105-149	0.024			0.83		
GT-2	245	210-297	0.051	0.051	0.050	1.66	1.32	1.07
GT-3	610	500-707	0.280	0.254	0.231	3.91	3.10	2.46
GT-5	950	707-1190	0.430	0.337	0.267	5.56	4.41	3.37
GT-6	1580	1410-1679	0.801		0.512	9.47		4.74
SG	650	595-707	0.31			4.6		

Material: Soda Lime Glass

Density ρ_s: 2480 kg/m^3

Specific heat c_{ps}: 753 J/kg K

Thermal conductivity k_s: 0.89 w/m K

TABLE 2

SINGLE TUBE HEAT TRANSFER DATA

Particle: GT-1 ($\bar{d}_p$ = 125 μm) , Pressure: 101.3 kPa

	$h(w/m^2\text{-}K)$ @ angle β								$\bar{h}$
U_N	0^o	45^o	90^o	135^o	180^o	225^o	270^o	315^o	$(w/m^2\text{-}K)$
0.0045	104.0	100.8	316.6	320.2	311.7	320.2	316.6	100.8	236
0.0121	108.1	106.2	342.8	356.9	302.4	386.0	361.4	102.3	258
0.0212	133.7	129.3	286.3	341.7	221.8	334.4	270.4	133.2	231
0.0310	173.7	196.4	215.3	335.6	233.7	321.7	210.3	216.3	238
0.0420	209.9	214.8	251.6	320.2	433.0	305.2	243.2	234.9	277
0.0537	217.0	204.9	369.5	365.7	512.9	350.2	360.7	185.8	321
0.0655	181.6	213.7	444.5	426.7	547.2	407.2	431.0	193.3	356
0.0791	158.6	161.2	432.9	444.9	584.4	425.0	420.6	162.2	349
0.0954	159.3	200.7	436.1	473.7	586.2	452.8	424.0	187.4	365
0.1177	160.9	203.0	496.0	541.4	595.5	517.2	481.7	180.4	397
0.1427	176.2	204.1	484.9	522.4	569.6	498.1	469.4	171.2	387
0.1669	154.9	233.7	478.3	539.4	565.7	514.3	462.7	188.7	392
0.1976	172.8	220.3	505.2	549.3	560.9	522.6	486.6	193.9	401
0.2525	181.4	216.0	505.6	588.7	571.7	560.7	488.2	192.3	413
0.3297	180.0	239.7	513.8	633.7	640.0	606.5	500.6	197.7	439

TABLE 3

SINGLE TUBE HEAT TRANSFER DATA

Particle: GT-2 ($\bar{d}_p$ = 245 μm)

$h(w/m^2\text{-}K)$ @ angle β

U_N	0°	45°	90°	135°	180°	225°	270°	315°	$\bar{h}$ $(w/m^2\text{-}K)$
P = 101.3 kPa									
0.0013	108.5	126.6	271.4	206.7	200.1	247.4	292.1	131.7	198
0.0059	143.7	143.1	278.3	211.8	208.1	251.3	293.4	161.7	211
0.0102	150.2	146.2	302.7	224.2	223.2	265.6	312.4	168.0	224
0.0159	156.6	127.9	311.9	237.2	212.8	255.0	312.7	154.6	221
0.0228	148.5	126.1	316.9	237.2	233.5	260.2	302.9	138.3	220
0.0303	160.5	120.9	329.2	255.4	226.5	244.2	296.4	132.2	220
0.0402	156.7	163.2	327.6	266.7	224.8	233.4	293.9	152.1	227
0.0518	203.4	186.5	316.3	249.1	197.7	209.8	279.8	172.3	227
0.0643	209.0	200.1	300.5	253.8	207.3	209.0	300.5	192.4	234
0.0755	244.3	255.0	308.8	250.5	213.8	226.8	308.8	257.2	258
0.0941	263.3	258.4	278.0	235.3	196.0	210.4	278.0	256.3	247
0.1126	234.4	242.2	275.8	230.3	207.0	223.1	275.8	262.2	244
0.1411	241.6	238.9	251.9	220.4	212.5	223.4	251.9	251.0	236
0.1709	231.8	213.7	251.3	220.3	236.9	232.0	251.3	234.2	234
0.2063	268.6	267.7	253.0	255.3	248.3	228.3	253.0	280.2	257

TABLE 3 (Continued)

U_N	h $(w/m^2\text{-}K)$ @ Angle β								$\bar{h}$
	0^o	45^o	90^o	135^o	180^o	225^o	270^o	315^o	$(w/m^2\text{-}K)$
P = 202.6 kPa									
0.0056	69.1	88.5	268.1	198.9	159.6	198.9	268.1	88.5	167
0.0127	109.9	121.8	280.4	207.4	188.2	207.4	280.4	121.8	190
0.0210	128.0	134.6	295.2	221.0	205.7	221.0	295.2	134.6	204
0.0300	155.4	149.4	313.6	243.0	194.4	228.7	276.1	176.0	217
0.0420	170.7	151.3	287.1	210.8	145.2	188.1	259.4	170.5	198
0.0550	204.7	194.0	343.9	285.0	198.3	203.0	343.9	198.6	246
0.0740	312.5	271.8	338.3	324.5	250.4	254.0	338.3	263.4	294
0.0970	333.8	308.9	382.3	360.8	316.1	310.3	382.3	319.4	339
0.1250	383.5	349.5	356.6	331.6	300.4	317.3	356.6	336.2	341
0.1480	492.4	353.9	354.0	385.5	447.1	418.6	354.0	353.9	395
0.1920	353.7	371.7	358.6	360.7	373.0	436.0	358.6	328.9	380
0.236	337.3	363.9	327.4	384.1	470.9	427.1	327.4	293.9	367

TABLE 3 (Continued)

$h(w/m^2-K)$@ Angle β

U_N	0^o	45^o	90^o	135^o	180^o	225^o	270^o	315^o	$\bar{h}_2$ (w/m^2-K)
				P = 405.3 kPa					
0.0088	10.3	59.5	356.6	262.6	127.1	262.6	356.6	59.5	187
0.0106	51.9	92.7	420.9	319.3	174.7	319.3	420.9	92.7	237
0.0148	74.2	118.8	439.5	320.3	187.1	320.3	439.5	118.8	252
0.0216	115.5	165.0	493.5	357.8	210.4	357.8	493.5	165.0	295
0.0296	146.1	238.2	544.5	431.0	280.3	431.0	544.5	238.2	357
0.0418	190.9	279.1	542.5	469.8	322.8	469.8	542.5	279.1	387
0.0599	190.6	238.5	390.0	339.2	256.9	339.2	390.0	238.5	298
0.0776	296.1	307.1	397.6	364.7	322.3	364.7	397.6	307.1	345
0.0921	317.9	301.3	329.0	334.4	339.8	292.2	318.3	304.8	317
0.1449	435.2	356.4	313.9	383.1	440.9	376.5	360.6	395.5	383
0.1666	433.8	328.6	266.7	349.5	435.6	370.5	317.0	369.8	359
0.2573	473.5	352.8	241.7	347.8	494.0	347.8	241.7	352.8	356
0.3146	527.4	405.9	268.7	395.5	563.6	395.5	268.7	405.9	404
0.3850	562.1	433.0	270.8	389.9	585.3	389.9	270.8	433.0	417

TABLE 4

SINGLE TUBE HEAT TRANSFER DATA

Particle: GT-3 ($\bar{d}_p$ = 610 μm) Pressure: 101.3 kPa

	$h (w/m^2-K)$ @ angle β								$\bar{h}$
U_N	0°	45°	90°	135°	180°	225°	270°	315°	(w/m^2-K)
0.0036	10.9	42.7	135.7	119.0	89.7	115.4	135.8	49.3	87
0.0112	75.9	101.3	197.8	131.0	111.7	124.8	190.7	106.5	130
0.0189	142.6	126.6	211.3	148.0	125.3	140.6	203.0	146.2	155
0.0285	219.5	181.8	216.6	163.9	144.8	155.5	207.7	186.8	185
0.0395	258.3	211.5	221.5	171.0	152.7	162.3	212.4	217.7	201
0.0529	279.1	228.9	220.9	179.8	162.5	170.7	211.8	228.9	210
0.0679	296.2	230.9	214.4	180.8	168.0	171.4	205.1	223.7	211
0.0843	273.8	213.1	193.8	173.2	166.1	164.2	185.4	188.8	195
0.1036	287.4	221.1	200.9	191.4	186.3	182.0	193.4	199.9	208
0.1408	301.0	222.1	198.5	192.8	192.0	182.8	189.9	190.0	209
0.2219	280.9	198.6	174.9	186.7	194.5	174.5	162.4	172.9	193

TABLE 4 (Continued)

SINGLE TUBE HEAT TRANSFER DATA

Particles: GT-3 ($\bar{d}_p$ = 610 μm) Pressure: 202.6 kPa

	$h(w/m^2\text{-}K)$ @ angle β								$\bar{h}$
U_N	0°	45°	90°	135°	180°	225°	270°	315°	$(w/m^2\text{-}K)$
0.0154	30.5	90.9	153.6	136.4	114.6	137.1	167.8	94.4	116
0.0228	19.1	71.5	167.4	136.8	122.7	134.1	182.2	92.2	116
0.0153	26.8	81.8	153.7	137.0	116.4	138.2	170.8	122.2	118
0.0281	55.7	78.4	180.0	139.5	134.2	137.0	186.6	107.2	127
0.0372	118.8	124.3	190.6	141.3	138.8	140.0	194.3	155.7	151
0.0462	168.7	156.4	191.4	141.2	142.3	143.0	191.0	179.9	164
0.0568	213.3	180.6	201.1	144.4	145.0	144.0	190.0	204.2	170
0.0685	200.9	189.0	208.2	152.8	154.6	155.0	203.2	200.1	183
0.0804	215.2	201.4	220.6	161.2	160.3	161.3	204.1	206.8	101
0.0980	249.0	238.6	287.8	210.3	211.5	220.1	270.5	224.7	230
0.1132	239.1	204.0	202.9	162.1	160.4	164.4	180.2	196.3	191
0.1338	243.7	199.9	201.4	167.3	173.3	164.5	186.8	190.1	191
0.1559	244.2	186.9	190.0	171.4	184.8	173.0	183.6	178.0	189
0.1824	230.1	178.5	178.0	167.4	191.9	156.1	182.2	173.3	182
0.2043	235.1	179.0	171.2	155.0	206.6	162.2	178.5	171.9	182
0.2335	242.3	181.4	176.0	126.9	187.3	156.2	199.6	162.0	179

TABLE 4 (Continued)

SINGLE TUBE HEAT TRANSFER DATA

Particles: GT-3 ($\bar{d}_p$ = 610 μm) Pressure: 405.3 kPa

U_N	h(w/m^2-K) @ angle β 0°	45°	90°	135°	180°	225°	270°	315°	$\bar{h}$ (w/m^2-K)
0.0037	12.3	71.4	160.3	160.2	134.7	150.6	162.1	76.4	117
0.0104	14.8	94.1	202.1	168.3	136.7	157.4	177.5	102.5	132
0.0150	10.2	92.8	207.4	166.7	135.8	155.6	178.7	83.6	129
0.0218	30.5	98.4	215.7	166.4	139.4	154.6	182.8	100.5	136
0.0287	61.4	122.1	226.8	166.5	143.4	150.6	185.7	135.9	149
0.0380	120.4	159.8	242.8	171.9	152.6	151.2	194.3	170.8	170
0.0511	180.4	193.4	242.8	175.6	157.5	153.8	20.13	196.9	188
0.0676	219.5	218.4	243.8	187.5	175.0	167.3	209.6	221.5	205
0.0855	237.7	228.5	240.3	196.3	184.8	175.6	209.5	222.5	212
0.1058	246.9	222.0	233.3	202.8	195.6	186.1	208.8	218.2	214
0.1293	248.8	208.4	220.8	205.1	204.6	190.7	203.2	204.8	211
0.1610	251.3	202.9	211.4	212.1	214.9	199.5	202.1	203.3	212
0.1964	253.2	196.7	204.9	221.0	221.6	204.6	202.9	201.8	213
0.2122	261.5	201.8	204.5	232.0	233.7	212.2	189.6	203.7	217
0.2321	260.2	199.5	197.2	231.2	236.6	209.1	186.9	203.0	215
0.2560	271.3	218.0	201.1	249.2	251.8	217.0	176.4	201.4	223

TABLE 5

SINGLE TUBE HEAT TRANSFER DATA

Particles: GT-5 ($\bar{d}_p$ = 950 μm) Pressure: 101.3 kPa

U_N	h(w/m^2-K) @ angle β 0°	45°	90°	135°	180°	225°	270°	315°	$\bar{h}$ (w/m^2-K)
0.0037	28.22	78.03	183.37	110.34	97.33	109.11	136.05	103.22	100
0.0090	23.24	51.80	159.18	110.92	104.28	107.13	156.72	65.27	97
0.0130	51.43	76.35	161.19	113.62	107.57	111.42	149.81	88.82	109
0.0212	116.79	128.75	168.94	120.33	117.72	120.34	170.62	139.73	135
0.0306	171.71	162.59	179.79	127.67	129.16	129.07	177.63	176.03	157
0.0422	207.16	186.57	192.54	141.16	139.07	141.43	181.92	193.00	173
0.0515	223.75	195.56	198.58	159.45	160.03	157.84	184.91	194.11	184
0.0688	221.06	181.71	185.16	162.32	164.28	161.87	175.10	172.15	178
0.0870	207.01	165.41	170.23	161.36	167.10	180.10	145.12	156.93	169
0.1062	203.35	156.37	160.94	158.96	156.48	158.96	135.24	165.28	162
0.1223	193.15	147.26	150.69	158.14	164.53	158.14	134.37	157.75	158
0.1429	194.45	144.10	147.03	166.61	172.05	166.61	124.10	154.06	159
0.1630	195.97	146.19	139.58	162.06	168.30	162.06	120.17	154.04	156
0.1897	201.06	156.55	146.50	171.51	174.68	171.51	146.50	148.47	165

TABLE 5 (Continued)

SINGLE TUBE HEAT TRANSFER DATA

Particles: GT-5 ($\bar{d}_p = 950\ \mu m$) Pressure: 202.6 kPa

	$h(w/m^2\text{-}K)$ @ angle β								$\bar{h}$
U_N	0°	45°	90°	135°	180°	225°	270°	315°	$(w/m^2\text{-}K)$
0.0050	24.4	109.2	159.9	141.8	126.7	137.2	156.9	113.3	121
0.0094	40.6	101.0	171.8	142.8	137.7	139.2	174.1	116.9	128
0.0145	106.1	135.5	192.7	146.6	144.3	143.1	193.3	161.3	153
0.0200	165.6	164.4	202.0	153.5	150.3	152.3	205.1	188.2	173
0.0280	212.7	198.9	220.2	163.4	165.0	167.5	210.6	208.8	193
0.0380	231.2	207.8	224.4	173.3	171.2	175.0	212.6	207.0	200
0.0530	238.5	207.3	223.3	179.0	176.2	175.5	202.8	199.2	200
0.0680	228.7	195.1	206.8	174.8	176.0	174.3	192.4	186.1	192
0.0850	222.7	181.8	194.6	180.5	183.1	179.5	186.8	173.0	188
0.1050	209.1	174.6	181.7	176.4	182.0	175.9	182.9	170.5	182
0.1230	209.3	163.7	175.1	172.4	180.1	173.1	165.7	160.0	175
0.1410	211.4	160.4	167.2	175.6	180.1	179.4	163.3	165.5	176
0.1620	207.7	161.1	168.5	172.4	184.3	175.0	152.8	165.5	173
0.1790	213.5	166.6	163.9	178.1	188.9	174.7	158.4	172.3	177

TABLE 5 (Continued)

SINGLE TUBE HEAT TRANSFER DATA

Particles: GT-5 ($\bar{d}_p$ = 950 μm) Pressure: 405.3 kPa

U_N	h(w/m^2-K) @ angle β 0°	45°	90°	135°	180°	225°	270°	315°	$\bar{h}$ (w/m^2-K)
0.0012	23.2	108.1	203.2	173.9	150.0	169.3	186.0	133.5	143
0.0047	24.3	79.1	231.6	177.3	152.0	167.0	193.9	78.2	138
0.0100	62.4	128.3	272.4	195.1	172.9	183.1	224.6	148.1	173
0.0183	135.5	209.2	304.6	218.8	198.2	195.1	242.9	228.4	217
0.0304	176.3	199.1	240.4	182.9	165.9	164.5	203.7	195.2	191
0.0422	253.3	249.0	285.2	233.6	217.1	210.2	246.0	242.4	242
0.0496	274.3	258.9	277.8	231.7	216.4	207.5	245.4	249.7	245
0.0565	286.0	263.3	208.7	274.5	259.4	238.9	291.4	261.0	273
0.0660	243.9	220.3	237.1	219.2	211.6	200.7	220.9	214.5	221
0.0758	277.6	243.9	268.2	264.2	253.6	240.0	243.4	242.0	254
0.0910	252.8	212.3	231.5	241.4	225.3	213.7	221.8	212.3	226
0.1106	239.9	201.1	211.2	24.14	234.1	216.2	220.5	208.2	222
0.1307	259.0	214.2	215.2	262.5	250.3	225.4	207.1	207.1	230

TABLE 6

SINGLE TUBE HEAT TRANSFER DATA

Particle: GT-6 ($\bar{d}_p$ = 1580 μm)

$h (w/m^2\text{-}K)$ @ Angle β

U_N	0°	45°	90°	135°	180°	225°	270°	315°	$\bar{h}$ $(w/m^2\text{-}K)$
					P = 101.3 kPa				
0.0012	27.62	100.71	132.61	121.34	122.34	117.08	127.28	118.37	108
0.0062	14.96	80.96	138.05	117.77	120.45	115.93	135.26	90.37	102
0.0114	47.35	92.82	147.38	116.97	119.57	114.21	149.10	106.81	112
0.0171	93.20	123.40	153.89	120.66	117.32	118.60	152.26	134.52	127
0.0233	116.40	142.18	164.97	125.11	119.21	122.32	156.89	147.63	137
0.0286	132.33	146.37	170.10	131.18	120.37	127.02	158.38	146.39	142
0.0362	142.40	146.04	172.75	138.81	126.16	133.46	162.74	144.07	146
0.0454	142.60	141.71	170.29	142.72	127.66	139.22	156.70	137.74	145
0.0554	141.01	138.31	168.44	144.98	134.75	147.03	154.63	137.22	146
0.0640	142.60	135.86	166.08	148.30	137.31	151.39	152.52	133.14	146
0.0760	138.11	133.54	158.05	147.10	138.76	142.36	154.83	133.15	143
0.0940	129.38	127.26	160.04	163.26	153.71	148.15	146.15	130.47	145

TABLE 6 (Continued)

$h (w/m^2-K)$ @ Angle β

U_N	0°	45°	90°	135°	180°	225°	270°	315°	$\bar{h}$ (w/m^2-K)
P = 405.3 kPa									
0.0025	20.7	124.6	180.1	164.6	169.7	158.5	177.6	140.7	142
0.0066	25.6	147.4	205.3	186.0	188.8	174.9	197.0	156.6	160
0.0167	67.3	158.7	233.0	175.0	176.8	171.1	217.1	169.0	171
0.0270	149.4	228.7	302.2	218.6	205.0	212.3	264.8	241.7	228
0.0380	204.4	281.1	353.2	263.9	235.5	249.9	303.4	280.5	271
0.0460	157.7	198.5	253.5	191.2	171.1	178.1	225.3	198.2	198
0.0540	179.6	220.5	277.2	217.9	191.2	201.4	247.6	220.4	219
0.0650	143.1	165.5	211.3	167.5	148.4	155.0	192.8	165.6	169
0.0750	222.0	248.4	313.7	265.9	234.7	248.0	288.0	251.1	259

TABLE 7

HEAT TRANSFER DATA FOR TEN-ROW BARE TUBE BUNDLE

Particle: SG ($\bar{d}_p$ = 650 μm) Pressure: 101.3 kPa

	w(2/m^2-K) @ angle β								$\bar{h}$
U_N	0°	45°	90°	135°	180°	225°	270°	315°	(w/m^2-K)
				Location 1					
0.0052	129.38	115.64	162.76	133.12	113.23	138.83	213.53	131.08	142
0.0128	240.78	227.37	185.77	159.10	138.59	159.10	185.77	227.37	190
0.0355	304.26	245.83	197.62	175.20	171.95	176.63	222.20	261.23	219
0.0512	297.05	229.78	188.29	177.47	172.10	172.84	199.09	239.63	210
0.0664	318.44	240.79	204.92	197.73	188.47	184.14	212.75	250.94	225
0.0865	294.02	200.27	169.06	176.67	180.57	167.83	173.12	207.59	196
0.1101	252.69	169.51	144.70	163.32	181.85	153.41	146.16	168.67	173
0.1469	345.88	196.76	201.66	256.07	282.88	244.69	185.89	195.87	239
0.2089	266.75	160.06	168.27	216.38	239.72	198.98	160.54	157.18	196
0.2880	296.54	176.21	153.39	198.91	224.30	183.77	152.53	178.57	196
				Location 2					
0.0067	49.32	60.86	149.09	116.17	77.67	111.87	166.91	70.12	100
0.0135	159.23	159.17	159.16	126.82	99.10	125.32	186.84	160.61	147
0.0377	250.33	217.21	145.86	119.75	128.37	134.16	183.39	235.89	177
0.0536	274.56	219.57	168.95	139.07	139.22	139.43	187.98	238.96	188
0.0696	282.40	207.50	161.86	144.62	142.68	146.43	183.14	228.63	187
0.0898	272.43	187.62	148.09	143.72	142.47	145.07	165.27	207.48	177
0.1118	263.36	171.97	144.97	144.91	146.24	145.57	161.30	190.38	171
0.1473	265.64	164.25	147.79	161.76	176.13	157.71	157.73	194.86	178
0.2131	283.08	167.82	141.85	166.65	183.90	157.36	141.80	202.85	181
0.2872	294.63	180.18	135.45	149.93	167.74	142.62	136.70	216.65	178

TABLE 8

SINGLE TUBE LOCAL FLUIDIZATION DATA

Particle: GT-2 ($\bar{d}_p$ = 245 μm)
Pressure: 101.3 kPa

U_N	$\bar{\theta}_D$(S)	f_L	α_D	α_L
		$\beta = 0^\circ$		
0.0109	35.233	0.001	0.452	0.800
0.0264	12.051	0.003	0.434	0.857
0.0527	5.451	0.008	0.457	0.861
0.1101	2.275	0.038	0.491	0.887
0.1923	0.979	0.085	0.471	0.890
0.3587	0.795	0.137	0.472	0.903
		$\beta = 90^\circ$		
0.0111	0.160	0.290	0.638	0.898
0.0266	0.373	0.209	0.630	0.901
0.0525	0.481	0.171	0.634	0.893
0.1118	0.237	0.368	0.657	0.883
0.1935	0.226	0.423	0.649	0.884
0.3596	0.144	0.500	0.678	0.889
		$\beta = 180^\circ$		
0.0129	0.063	0.987	0.765	0.896
0.0265	0.126	0.799	0.744	0.855
0.0532	0.111	0.855	0.744	0.863
0.1112	0.154	0.598	0.716	0.843
0.2025	0.102	0.820	0.655	0.885
0.3770	0.103	0.733	0.660	0.871

TABLE 8 (Continued)

Particle: GT-2($\bar{d}_p$ = 245 μm)
Pressure: 202.6 kPa

U_N	$\bar{\theta}_D$(S)	f_L	α_D	α_L
		$\beta = 0^\circ$		
0.0105	81.900	0.000	0.417	0.800
0.0278	14.015	0.002	0.439	0.839
0.0527	6.982	0.004	0.496	0.846
0.1119	1.350	0.046	0.487	0.880
0.1729	0.629	0.128	0.466	0.889
0.2628	0.410	0.220	0.480	0.877
		$\beta = 90^\circ$		
0.0103	0.270	0.197	0.678	0.878
0.0278	0.444	0.134	0.636	0.879
0.0531	0.898	0.074	0.618	0.885
0.1112	0.368	0.204	0.701	0.874
0.1723	0.201	0.340	0.683	0.874
0.2624	0.202	0.279	0.724	0.874
		$\beta = 180^\circ$		
0.0107	0.274	0.337	0.758	0.821
0.0281	0.147	0.618	0.726	0.853
0.0536	0.238	0.290	0.671	0.854
0.1127	0.104	0.518	0.741	0.895
0.1821	0.142	0.819	0.666	0.905
0.2659	0.077	0.862	0.674	0.893

TABLE 8 (Continued)

Particle: GT-2($\bar{d}_p$ = 245 μm)
Pressure: 405.3 kPa

U_N	$\bar{\theta}_D$(S)	f_L	α_D	α_L
		β = 0°		
0.0107	204.750	0.000	0.515	0.800
0.0255	44.132	0.000	0.537	0.830
0.0488	5.119	0.003	0.472	0.828
0.1129	1.106	0.050	0.498	0.869
0.2038	0.271	0.206	0.507	0.870
0.3134	0.090	0.199	0.508	0.876
		β = 90°		
0.0106	0.135	0.306	0.693	0.873
0.0257	0.148	0.299	0.690	0.877
0.0484	0.378	0.179	0.712	0.883
0.1115	0.163	0.330	0.732	0.872
0.2045	0.130	0.367	0.738	0.857
0.3139	0.100	0.400	0.742	0.859
		β = 180°		
0.0109	0.293	0.153	0.656	0.815
0.0259	0.448	0.139	0.634	0.833
0.0491	0.267	0.163	0.577	0.841
0.1131	0.190	0.251	0.556	0.835
0.2139	0.110	0.434	0.625	0.873
0.3151	0.073	0.611	0.652	0.874

TABLE 9

SINGLE TUBE LOCAL FLUIDIZATION DATA

Particle: GT-3($\bar{d}_p$ = 610 μm)
Pressure: 101.3 kPa

U_N	$\bar{\theta}_D(S)$	f_L	α_D	α_L
		$\beta = 0^o$		
0.0164	8.190	0.004	0.447	0.806
0.0264	2.985	0.146	0.552	0.822
0.0467	0.816	0.080	0.606	0.831
0.0875	0.248	0.280	0.648	0.844
0.1657	0.222	0.309	0.601	0.859
0.2221	0.137	0.550	0.637	0.866
		$\beta = 90^o$		
0.0153	0.275	0.456	0.741	0.876
0.0261	0.174	0.618	0.755	0.872
0.0450	0.445	0.802	0.719	0.883
0.0859	0.302	0.780	0.766	0.867
0.1636	0.161	0.427	0.761	0.857
0.2208	0.179	0.430	0.749	0.862
		$\beta = 180^o$		
0.0175	0.288	0.352	0.702	0.874
0.0276	0.275	0.400	0.699	0.891
0.0457	0.161	0.447	0.607	0.900
0.0895	0.189	0.484	0.586	0.915
0.1349	0.154	0.515	0.551	0.908
0.1751	0.132	0.551	0.579	0.930

TABLE 9

Particle: GT-3($\bar{d}_p$ = 610 μm)
Pressure: 202.6 kPa

U_N	$\bar{\theta}_D$(S)	f_L	α_D	α_L
		$\beta = 0^o$		
0.0107	819.000	0.000	0.463	0.800
0.0172	204.750	0.000	0.495	0.800
0.0380	3.206	0.009	0.553	0.846
0.0731	0.467	0.145	0.633	0.846
0.1383	0.320	0.279	0.623	0.867
0.2004	0.155	0.497	0.631	0.870
		$\beta = 90^o$		
0.0101	0.053	0.753	0.744	0.874
0.0166	0.074	0.734	0.765	0.868
0.0365	0.090	0.880	0.733	0.880
0.0724	0.108	0.752	0.756	0.871
0.1356	0.234	0.516	0.729	0.880
0.1959	0.177	0.458	0.738	0.868
		$\beta = 180^o$		
0.0097	0.135	0.564	0.709	0.911
0.0175	0.122	0.633	0.712	0.902
0.0388	0.130	0.566	0.664	0.898
0.0695	0.126	0.531	0.615	0.908
0.1193	0.140	0.487	0.554	0.898
0.1753	0.115	0.504	0.566	0.892

TABLE 9 (Continued)

Particle: GT-3($\bar{d}_p$ = 610 μm)
Pressure: 405.6 kPa

U_N	$\bar{\theta}_D$(S)	f_L	α_D	α_L
		$\beta = 0^o$		
0.0076	409.500	0.000	0.538	0.800
0.0152	81.900	0.001	0.548	0.824
0.0355	0.972	0.103	0.647	0.831
0.0700	1.043	0.080	0.614	0.864
0.1342	0.088	0.574	0.652	0.861
0.1925	0.122	0.480	0.634	0.874
		$\beta = 90^o$		
0.0060	0.056	0.537	0.714	0.883
0.0143	0.058	0.781	0.744	0.862
0.0350	0.076	0.804	0.723	0.881
0.0687	0.118	0.722	0.757	0.874
0.1337	0.338	0.355	0.714	0.880
0.1916	0.313	0.329	0.754	0.867
		$\beta = 180^o$		
0.0079	0.054	0.709	0.705	0.909
0.0194	0.088	0.575	0.718	0.915
0.0396	0.089	0.638	0.666	0.893
0.0690	0.117	0.537	0.618	0.905
0.1083	0.124	0.493	0.558	0.897
0.1657	0.139	0.442	0.559	0.883

TABLE 10

SINGLE TUBE LOCAL FLUIDIZATION DATA

Particle: GT-5($\bar{d}_p$ = 950 μm)
Pressure: 101.3 kPa

U_N	$\bar{\theta}_D(S)$	f_L	α_D	α_L
		$\beta = 0^o$		
0.0026	81.900	0.004	0.613	0.800
0.0118	9.314	0.173	0.643	0.831
0.0260	0.629	0.150	0.636	0.833
0.0460	0.927	0.256	0.581	0.848
0.0676	0.557	0.378	0.601	0.858
		$\beta = 90^o$		
0.0036	0.876	0.120	0.709	0.875
0.0126	0.433	0.187	0.726	0.861
0.0272	0.271	0.221	0.729	0.860
0.0481	0.340	0.203	0.686	0.859
0.0692	0.281	0.239	0.640	0.857
0.1187	0.482	0.237	0.607	0.868
		$\beta = 180^o$		
0.0035	0.088	0.453	0.715	0.864
0.0113	0.176	0.432	0.658	0.881
0.0429	0.218	0.450	0.556	0.902
0.0683	0.393	0.308	0.564	0.907
0.1094	0.210	0.353	0.584	0.911

TABLE 10 (Continued)

Particle: GT-5($\bar{d}_p$ = 950 μm)
Pressure: 202.6 kPa

U_N	$\bar{\theta}_D(S)$	f_L	α_D	α_L
		$\beta = 0^o$		
0.0174	1.571	0.106	0.630	0.830
0.0305	0.176	0.429	0.650	0.843
0.0432	0.970	0.125	0.611	0.849
0.0636	0.143	0.420	0.625	0.847
0.0982	0.265	0.334	0.581	0.869
		$\beta = 90^o$		
0.0171	0.166	0.437	0.701	0.844
0.0269	0.113	0.564	0.705	0.841
0.0427	0.144	0.454	0.691	0.842
0.0642	0.378	0.215	0.620	0.849
0.0782	0.572	0.146	0.632	0.843
0.1293	0.474	0.150	0.622	0.856
		$\beta = 180^o$		
0.0130	0.315	0.349	0.692	0.839
0.0289	0.336	0.298	0.631	0.854
0.0434	0.504	0.267	0.625	0.885
0.0649	0.532	0.263	0.631	0.893
0.0118	0.367	0.258	0.639	0.899
0.1188	0.273	0.243	0.633	0.891

TABLE 10 (Continued)

Particle: GT-5($\bar{d}_p$ = 950 μm)

Pressure: 405.3 kPa

U_N	$\bar{\theta}_D$(S)	f_L	α_D	α_L
		$\beta = 0^o$		
0.0068	204.750	0.000	0.596	0.800
0.0194	0.918	0.234	0.648	0.832
0.0304	0.158	0.373	0.664	0.868
0.0504	0.205	0.357	0.622	0.846
0.0894	0.071	0.712	0.621	0.865
		$\beta = 90^o$		
0.0067	0.125	0.406	0.708	0.853
0.0192	0.102	0.624	0.707	0.847
0.0305	0.118	0.562	0.703	0.844
0.0501	0.105	0.535	0.689	0.851
0.0907	0.424	0.143	0.648	0.847
0.1434	0.606	0.115	0.659	0.839
		$\beta = 180^o$		
0.0045	0.082	0.575	0.688	0.873
0.0184	0.159	0.435	0.688	0.888
0.0348	0.152	0.441	0.643	0.894
0.0579	0.249	0.374	0.613	0.900
0.0853	0.144	0.431	0.567	0.893
0.1260	0.119	0.445	0.563	0.905

TABLE 11

SINGLE TUBE LOCAL FLUIDIZATION DATA

Particle: GT-6($\bar{d}_p$ = 1580 μm)
Pressure: 101.3 kPa

U_N	$\bar{\theta}_D$(S)	f_L	α_D	α_L
		$\beta = 0^o$		
0.0064	41.092	0.109	0.604	0.822
0.0085	5.462	0.468	0.652	0.837
0.0133	0.945	0.949	0.669	0.891
0.0239	0.211	0.705	0.636	0.917
0.0390	0.057	0.910	0.643	0.923
0.0640	0.091	0.863	0.625	0.926
		$\beta = 90^o$		
0.0057	0.082	0.562	0.723	0.908
0.0084	0.104	0.620	0.713	0.916
0.0124	0.081	0.833	0.720	0.921
0.0238	0.061	0.769	0.717	0.935
0.0397	0.088	0.588	0.709	0.918
0.0646	0.082	0.519	0.723	0.919
		$\beta = 180^o$		
0.0057	0.347	0.472	0.746	0.841
0.0104	0.299	0.561	0.749	0.846
0.0166	0.362	0.531	0.710	0.871
0.0263	0.275	0.461	0.673	0.897
0.0417	0.324	0.469	0.662	0.912
0.0641	0.254	0.476	0.630	0.885

TABLE 11 (Continued)

Particle: GT-6 (1580 μm)
Pressure: 405.3 kPa

U_N	$\bar{\theta}_D(S)$	f_L	α_D	α_L
		$\beta = 0^\circ$		
0.0017	18.407	0.628	0.670	0.858
0.0064	40.950	0.391	0.665	0.845
0.0141	0.373	0.680	0.635	0.895
0.0300	0.056	0.876	0.636	0.932
0.0537	0.081	0.904	0.594	0.916
		$\beta = 90^\circ$		
0.0008	0.074	0.567	0.723	0.925
0.0058	0.096	0.561	0.730	0.926
0.0129	0.071	0.693	0.698	0.921
0.0300	0.058	0.688	0.726	0.927
0.0518	0.081	0.572	0.728	0.904
0.0716	0.080	0.500	0.721	0.893
		$\beta = 180^\circ$		
0.0020	0.304	0.454	0.760	0.843
0.0072	0.221	0.586	0.744	0.850
0.0149	0.195	0.560	0.726	0.877
0.0308	0.168	0.553	0.679	0.883
0.0539	0.171	0.579	0.656	0.897
0.0732	0.184	0.547	0.646	0.892

TABLE 12

LOCAL FLUIDIZATION DATA FOR TEN-ROW BARE TUBE BUNDLE

Particle: SG($\bar{d}_p$ = 650 μm)
Pressure: 101.3 kPa

Location 1, inner-row

U_N	$\bar{\theta}_D(S)$	α_D	α_L	f_L
		$\beta = 0^o$		
0.0350	1.572	0.494	0.875	0.062
0.0521	0.952	0.508	0.888	0.077
0.0667	0.827	0.518	0.908	0.105
0.0895	0.589	0.528	0.905	0.171
0.1132	0.488	0.541	0.924	0.220
0.1468	0.356	0.545	0.925	0.245
0.2131	0.296	0.552	0.927	0.307
0.2873	0.277	0.572	0.933	0.350
		$\beta = 45^o$		
0.0037	15.475	0.526	0.800	0.000
0.0149	0.350	0.539	0.840	0.035
0.0372	1.322	0.555	0.883	0.075
0.0517	1.263	0.555	0.893	0.126
0.0704	0.432	0.563	0.909	0.268
0.0913	0.413	0.594	0.913	0.299
0.1153	0.392	0.602	0.918	0.342
0.1463	0.269	0.618	0.929	0.398
0.2165	0.183	0.626	0.935	0.445
0.2916	0.190	0.632	0.945	0.484

TABLE 12 (Continued)

U_N	$\bar{\theta}_D(S)$	α_D	α_L	f_L
		$\beta = 90^o$		
0.0048	0.122	0.627	0.942	0.388
0.0147	0.189	0.609	0.951	0.427
0.0374	0.334	0.586	0.959	0.407
0.0524	0.339	0.595	0.963	0.428
0.0704	0.297	0.596	0.946	0.499
0.0911	0.222	0.595	0.944	0.560
0.1146	0.216	0.601	0.942	0.618
0.1484	0.196	0.597	0.947	0.658
0.2151	0.149	0.616	0.954	0.693
0.2900	0.135	0.634	0.960	0.727
		$\beta = 135^o$		
0.0036	0.025	0.666	0.912	0.921
0.0138	0.066	0.636	0.944	0.667
0.0380	0.178	0.624	0.944	0.499
0.0539	0.203	0.609	0.932	0.481
0.0696	0.201	0.600	0.923	0.447
		$\beta = 180^o$		
		- NO DATA -		

TABLE 13

FLUIDIZATION DATA FOR TEN-ROW BARE TUBE BUNDLE

Location 2
Bottom-row

Particle: SG($\bar{d}_p$ = 650 μm)
Pressure: 101.3 kPa

U_N	$\bar{\theta}_D(S)$	α_D	α_L	f_L
		$\beta = 0^o$		
0.0034	80.0	0.4925	0.08	0.0
0.0145	4.095	0.5321	0.8	0.0
0.0378	2.0475	0.5333	0.8	0.0
0.0538	1.692	0.5188	0.8364	0.0284
0.0695	1.584	0.5019	0.8627	0.0306
0.0899	1.398	0.5036	0.8944	0.0505
0.1136	0.795	0.5162	0.9403	0.1302
0.1474	1.037	0.5112	0.9570	0.1620
0.2090	1.122	0.5331	0.9589	0.1797
0.2879	1.683	0.5040	0.9593	0.0883
		$\beta = 45^o$		
0.0039	48.0	0.4860	0.8	0.0
0.0141	3.665	0.6383	0.8205	0.0089
0.0375	0.3345	0.7118	0.8937	0.2606
0.0532	0.3171	0.6877	0.9192	0.2663
0.0688	0.4983	0.6542	0.9445	0.2785
0.1131	0.3496	0.6361	0.9416	0.3405
0.1468	0.4277	0.6047	0.9543	0.3808
0.2132	0.1868	0.5869	0.9570	0.4119
0.2870	0.5811	0.5729	0.9626	0.3515
		$\beta = 90^o$		
0.0035	0.1061	0.6139	0.9520	0.5188
0.0143	0.2239	0.6793	0.9725	0.5244
0.0363	0.2082	0.7073	0.9682	0.5373
0.0535	0.1383	0.7202	0.9524	0.6040
0.0692	0.1597	0.6985	0.9581	0.5846
0.0898	0.1269	0.6982	0.9581	0.6868
0.1137	0.1614	0.6626	0.9508	0.6180
0.1476	0.089	0.6730	0.9430	0.7443
0.2139	0.1093	0.6382	0.9557	0.7039
0.2900	0.1242	0.6513	0.9404	0.7156

TABLE 13 (Continued)

U_N	$\bar{\theta}_D(S)$	α_D	α_L	f_L
		$\beta = 135^\circ$		
0.0033	0.0	0.8	0.9554	1.0
0.0144	0.0	0.8	0.9364	1.0
0.0363	0.010	0.7975	0.9119	0.9788
0.0534	0.051	0.7848	0.9017	0.9785
0.0689	0.0656	0.7566	0.8958	0.9474
0.0894	0.0966	0.7360	0.9007	0.9113
0.1131	0.1034	0.6328	0.9251	0.7548
0.1470	0.0924	0.6111	0.9444	0.6581
0.2082	0.0908	0.5789	0.9520	0.6489
		$\beta = 180^\circ$		
0.0035	0.0292	0.6932	0.9691	0.9644
0.0147	0.1462	0.6945	0.9558	0.7864
0.0381	0.1288	0.6876	0.9604	0.7006
0.0541	0.1754	0.6178	0.9766	0.6343
0.0706	0.1827	0.5879	0.9839	0.5987
0.0903	0.1637	0.5598	0.9829	0.5763
0.1141	0.1528	0.5495	0.9754	0.5466
0.1509	0.1709	0.5194	0.9695	0.4902
0.2098	0.1809	0.5153	0.9613	0.4581

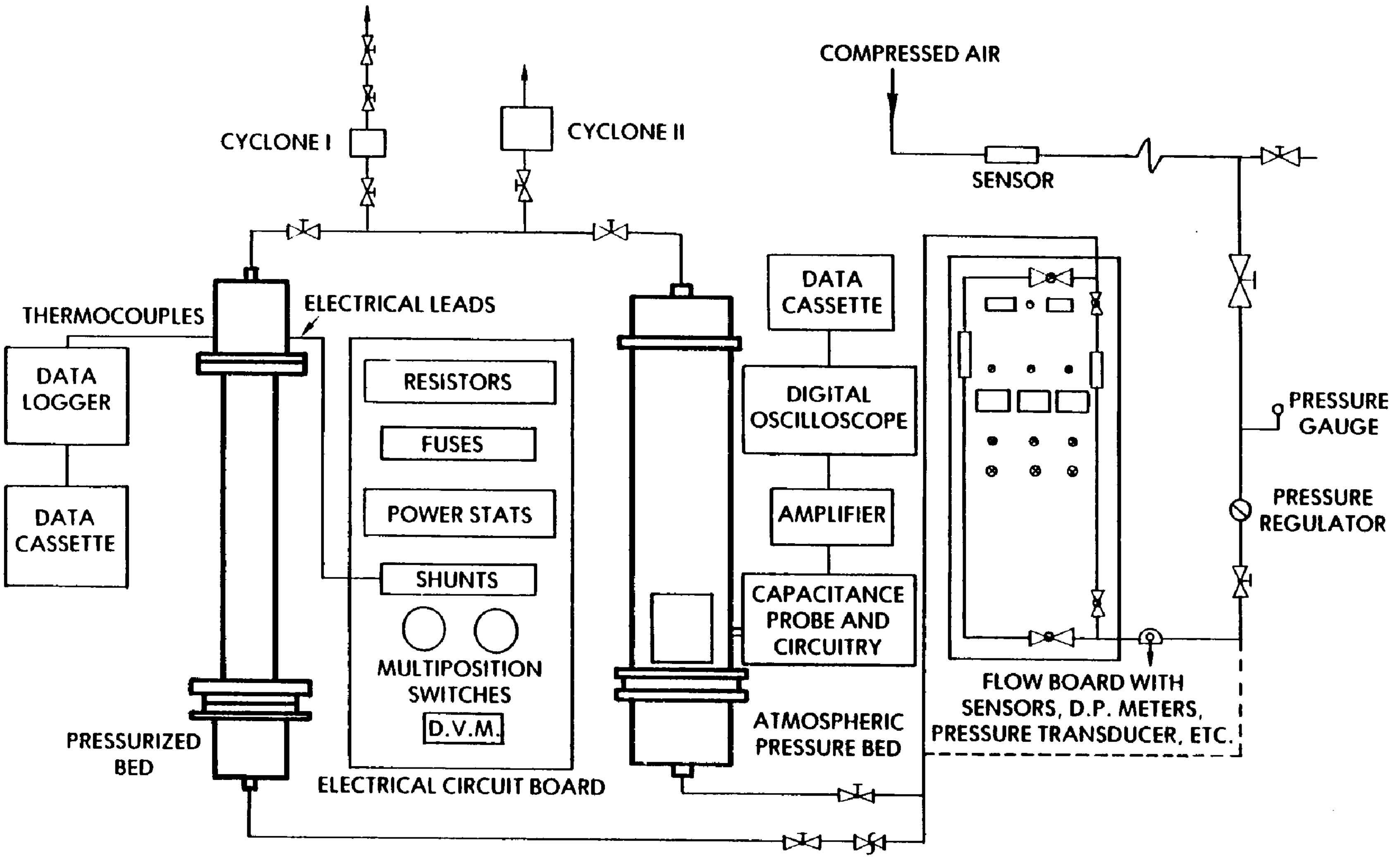

Figure 1 Fluidized bed test facility for single tube experiments

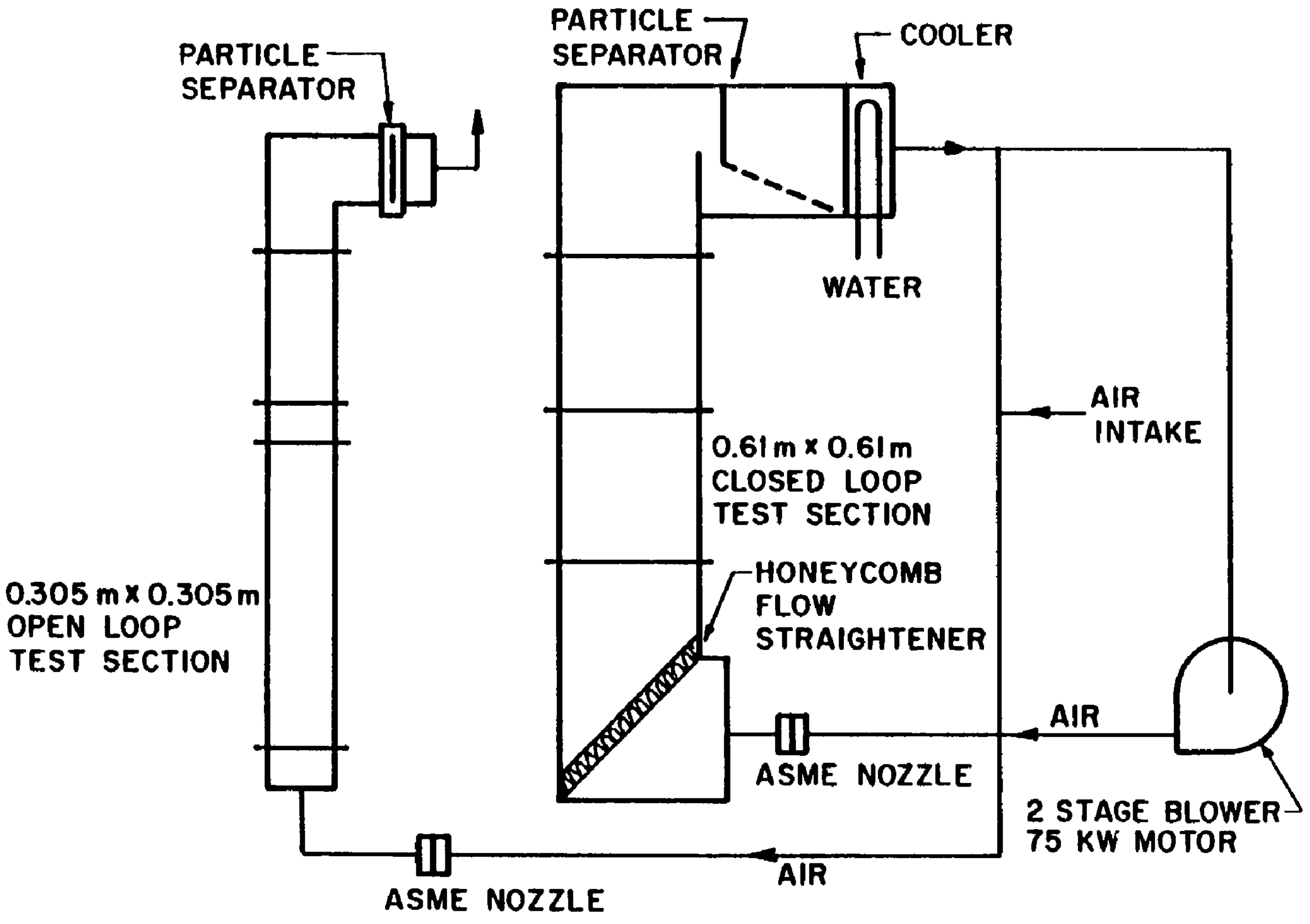

Figure 2 Fluidized bed test facility for tube bundle experiments

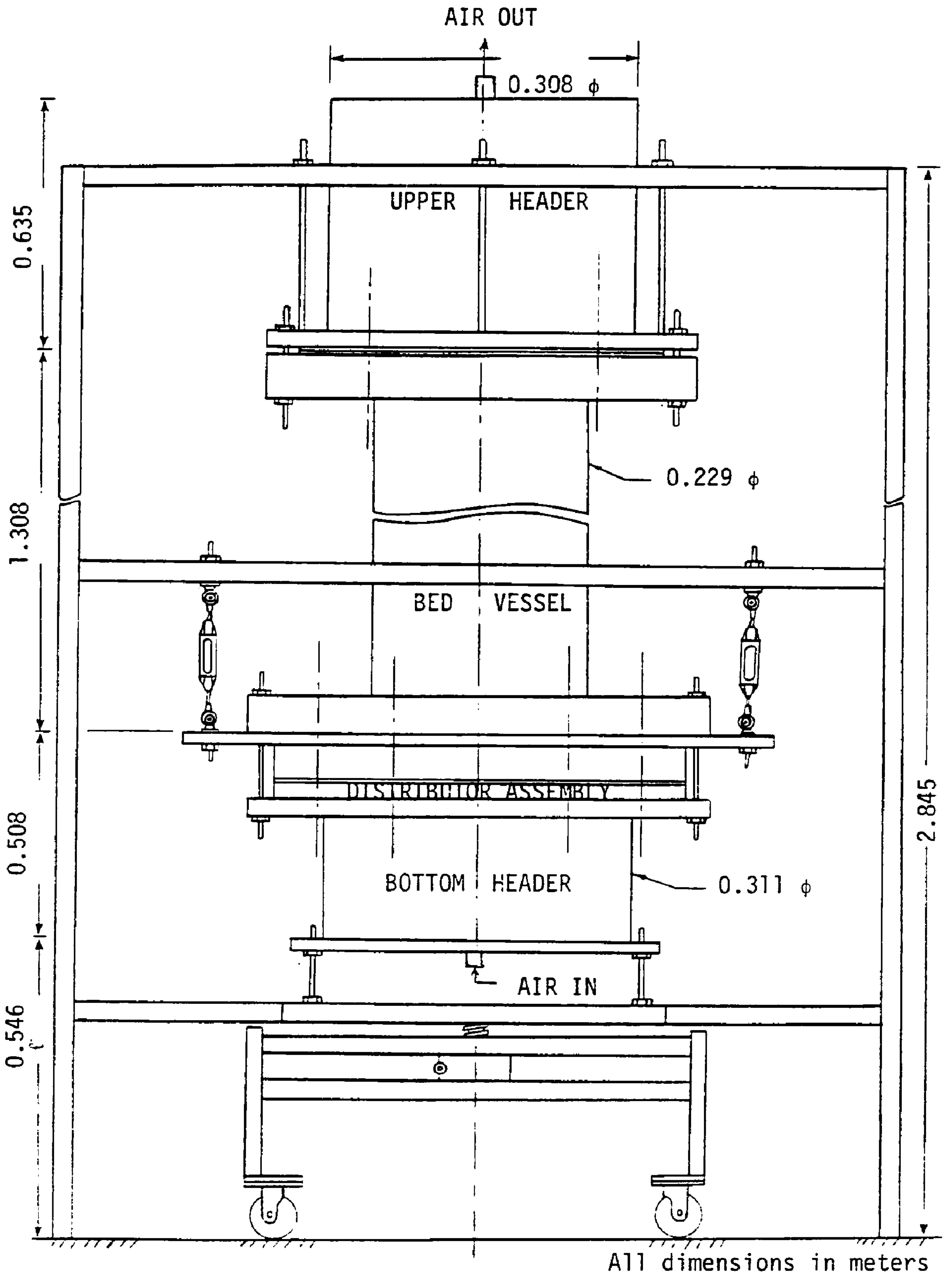

Figure 3 Sketch of pressurized-bed

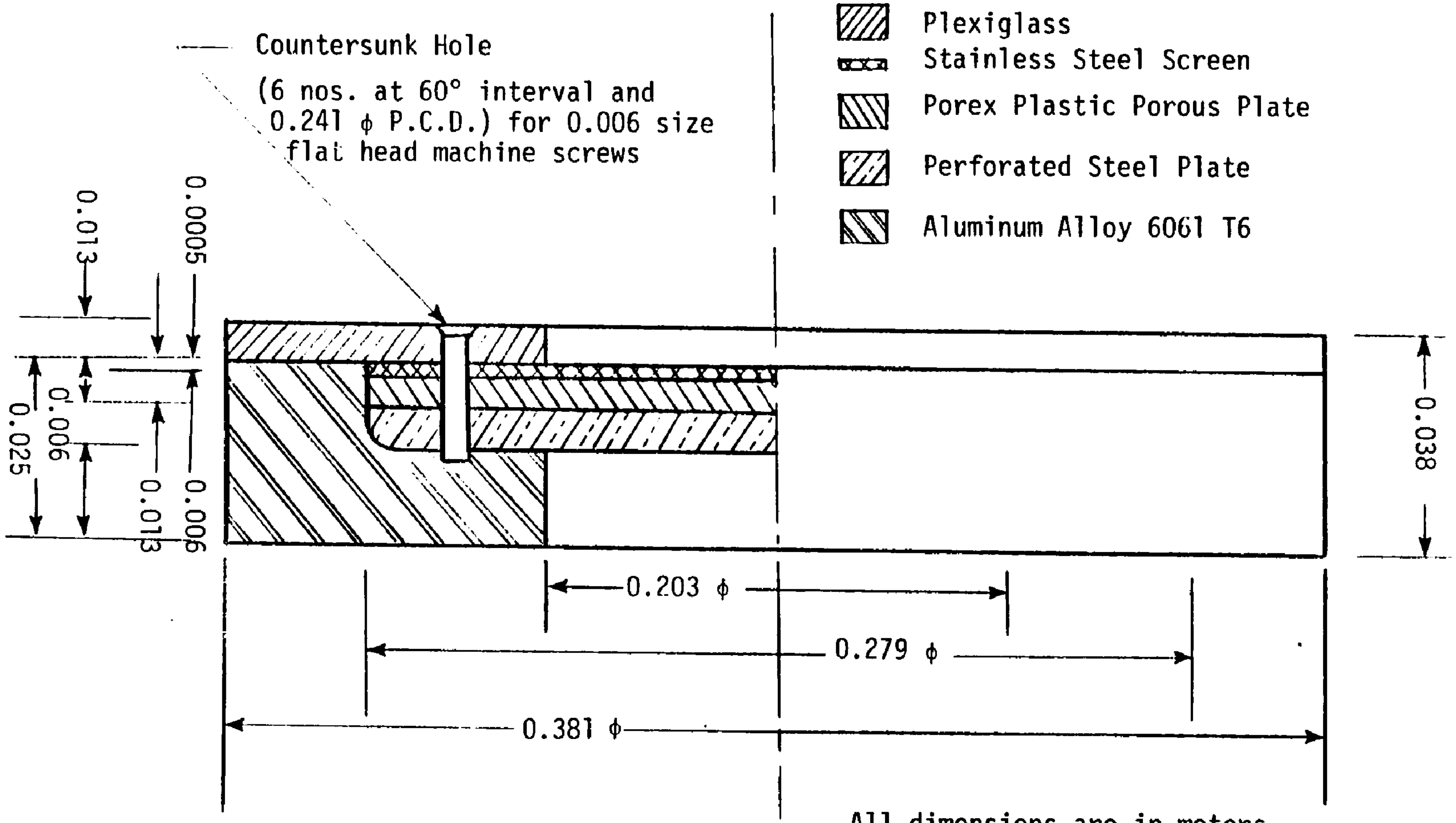

All dimensions are in meters

Figure 4 Distributor configuration

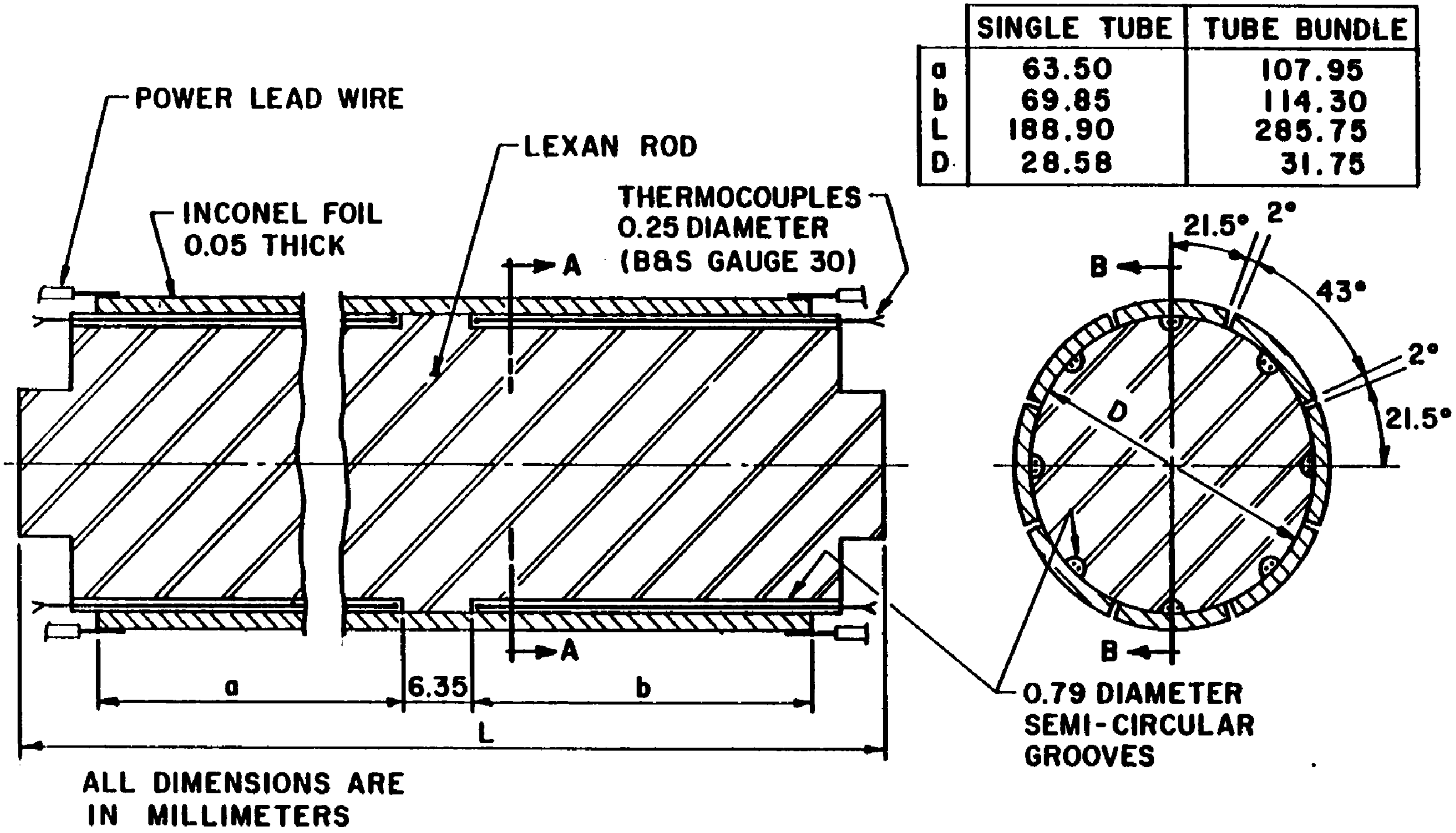

	SINGLE TUBE	TUBE BUNDLE
a	63.50	107.95
b	69.85	114.30
L	188.90	285.75
D	28.58	31.75

ALL DIMENSIONS ARE
IN MILLIMETERS

Figure 5 **HEAT TRANSFER TEST SECTION**

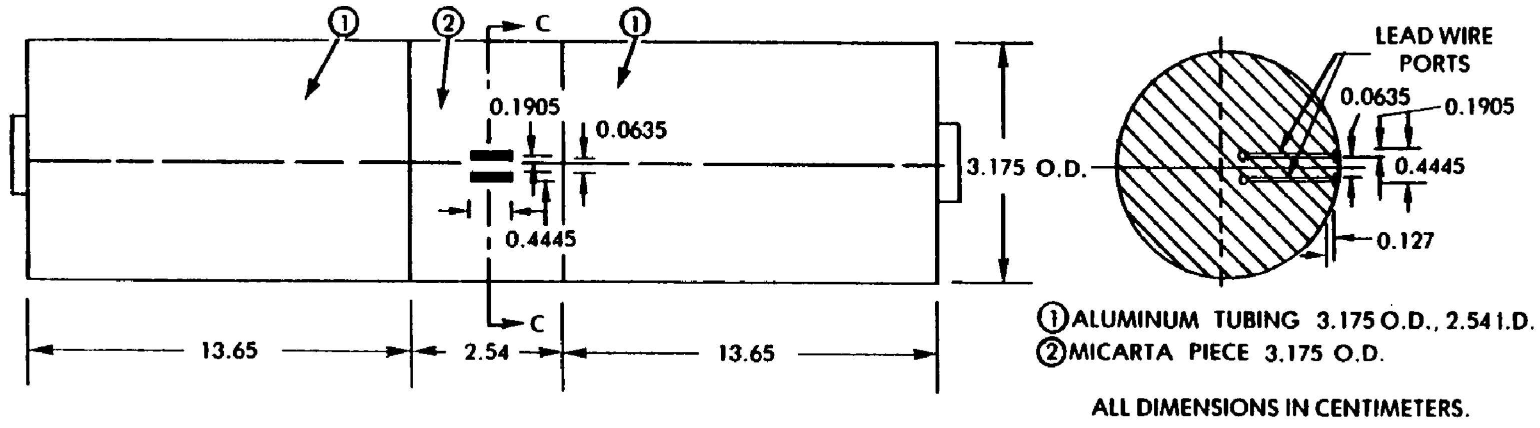

Figure 6 Capacitance test section used in tube bundle experiments

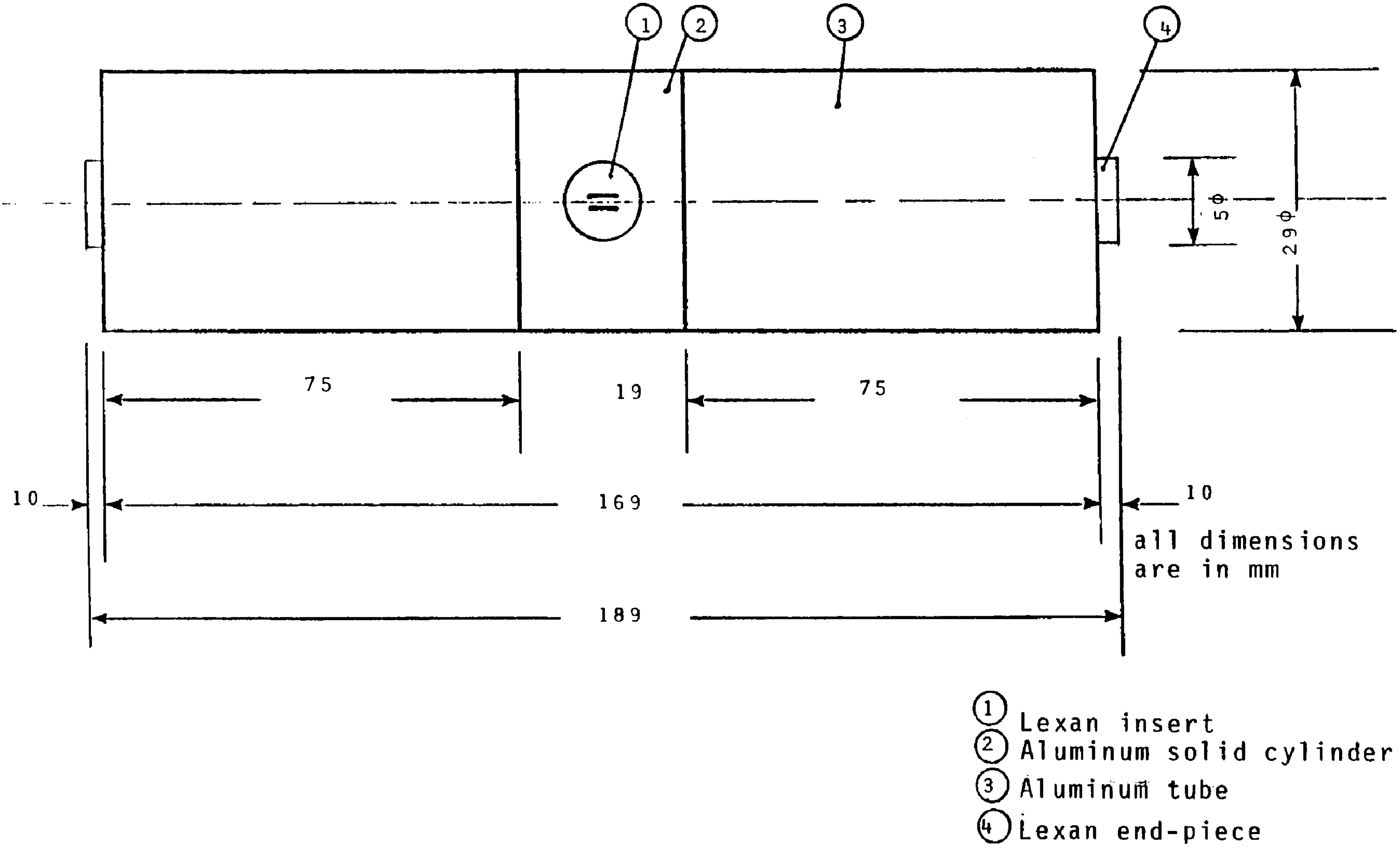

Figure 7a Capacitance test section used in single tube experiments

Part ①

Material: Lexan
Electrodes: Silver Solder Epoxy-Filled
Quantity: 2 Nos.

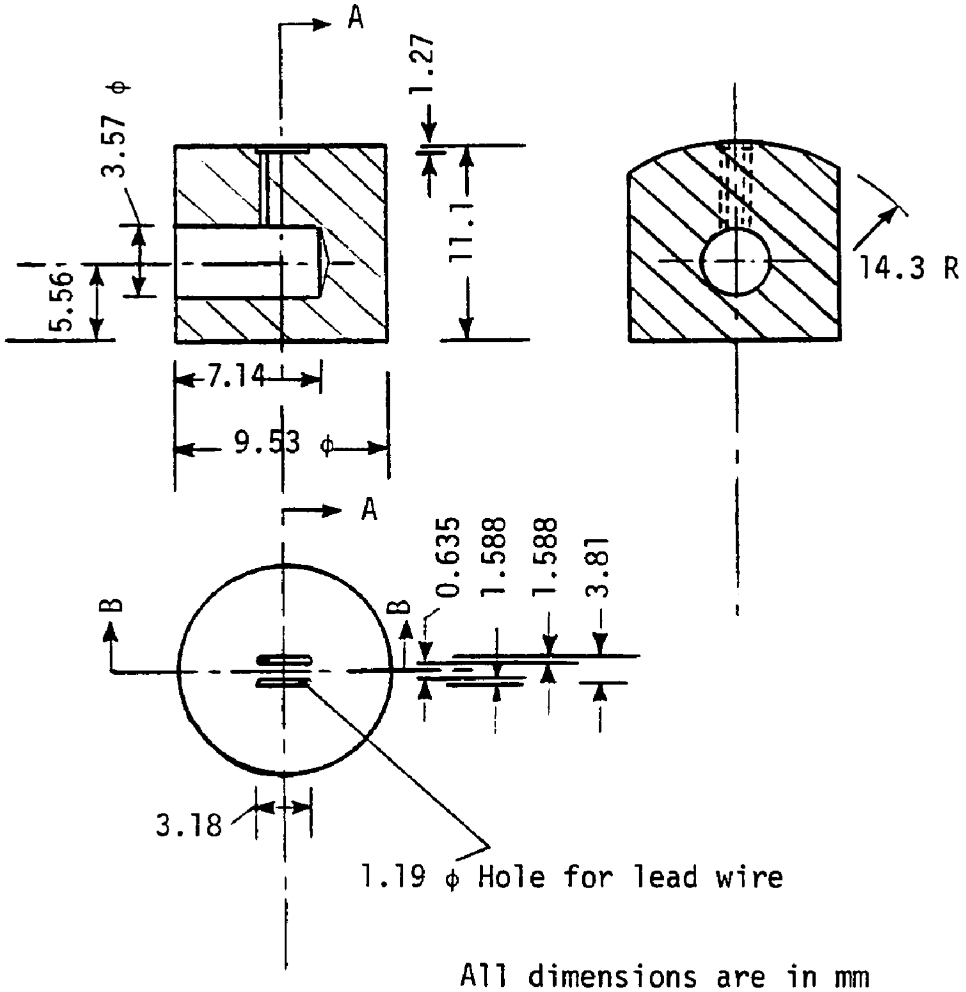

All dimensions are in mm

Figure 7b Capacitance test section used in single tube experiments

Part ②

Material: Aluminum Quantity: 1

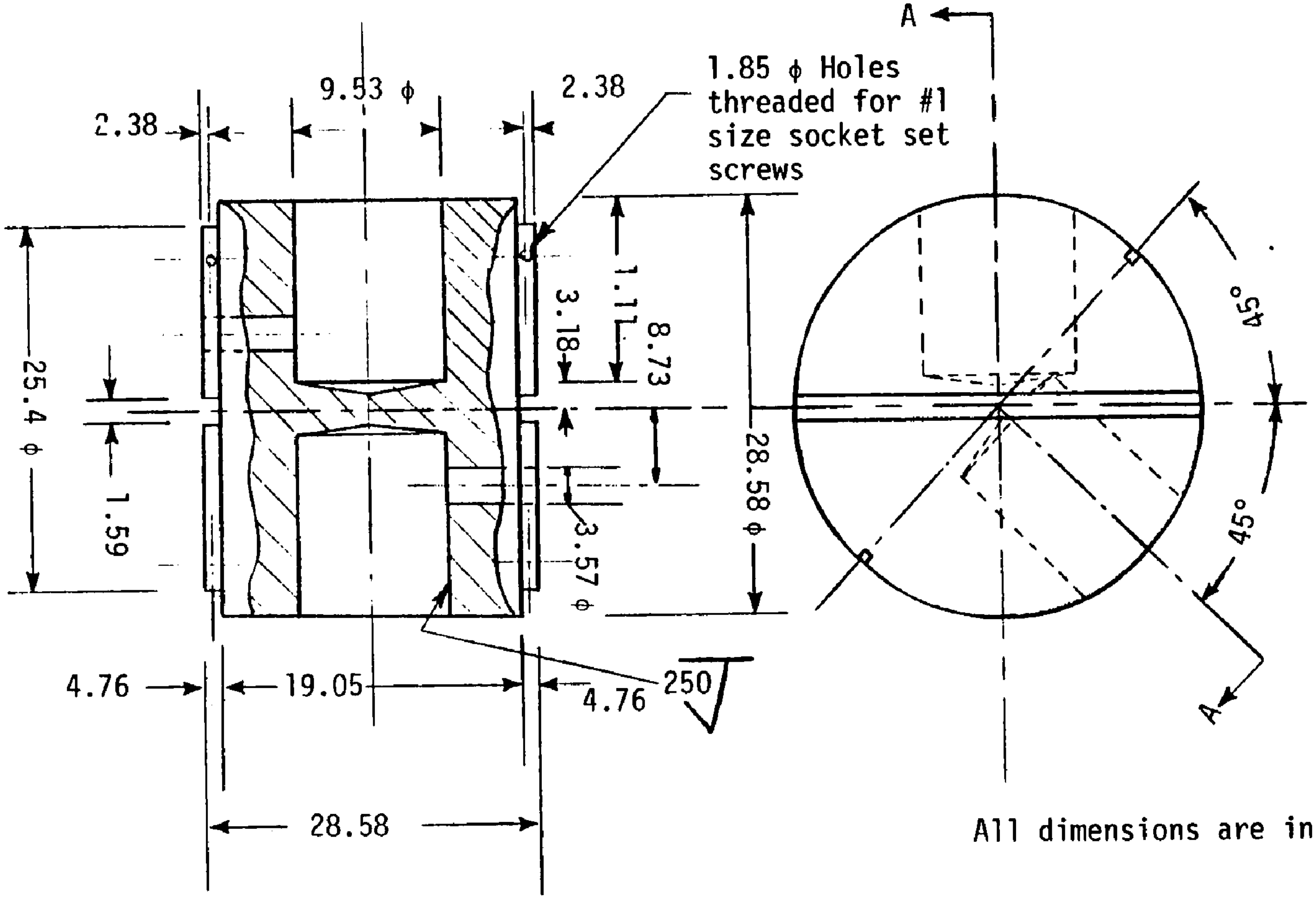

All dimensions are in mm

Figure 7c Capacitance test section used in single tube experiments

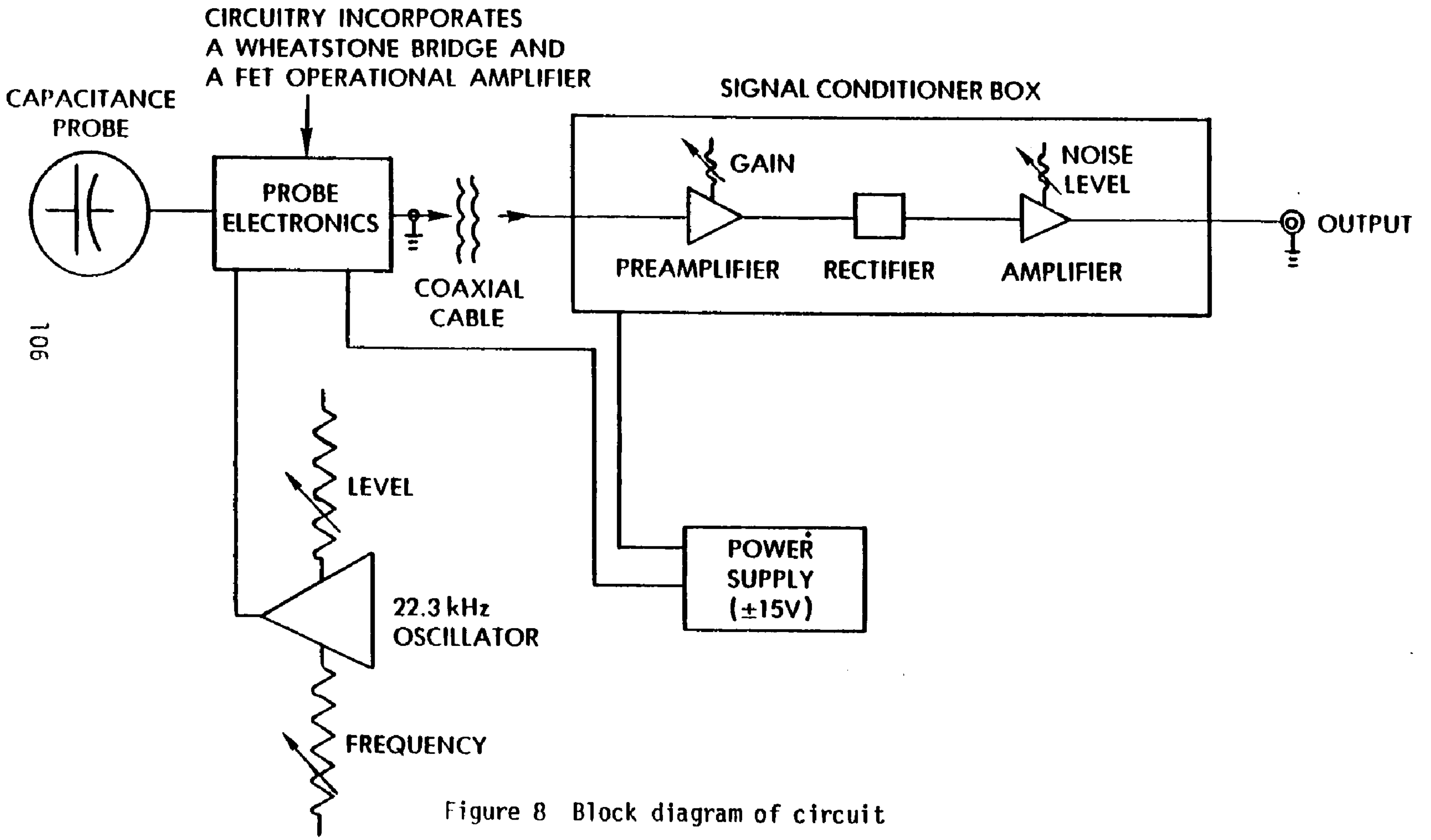

Figure 8 Block diagram of circuit

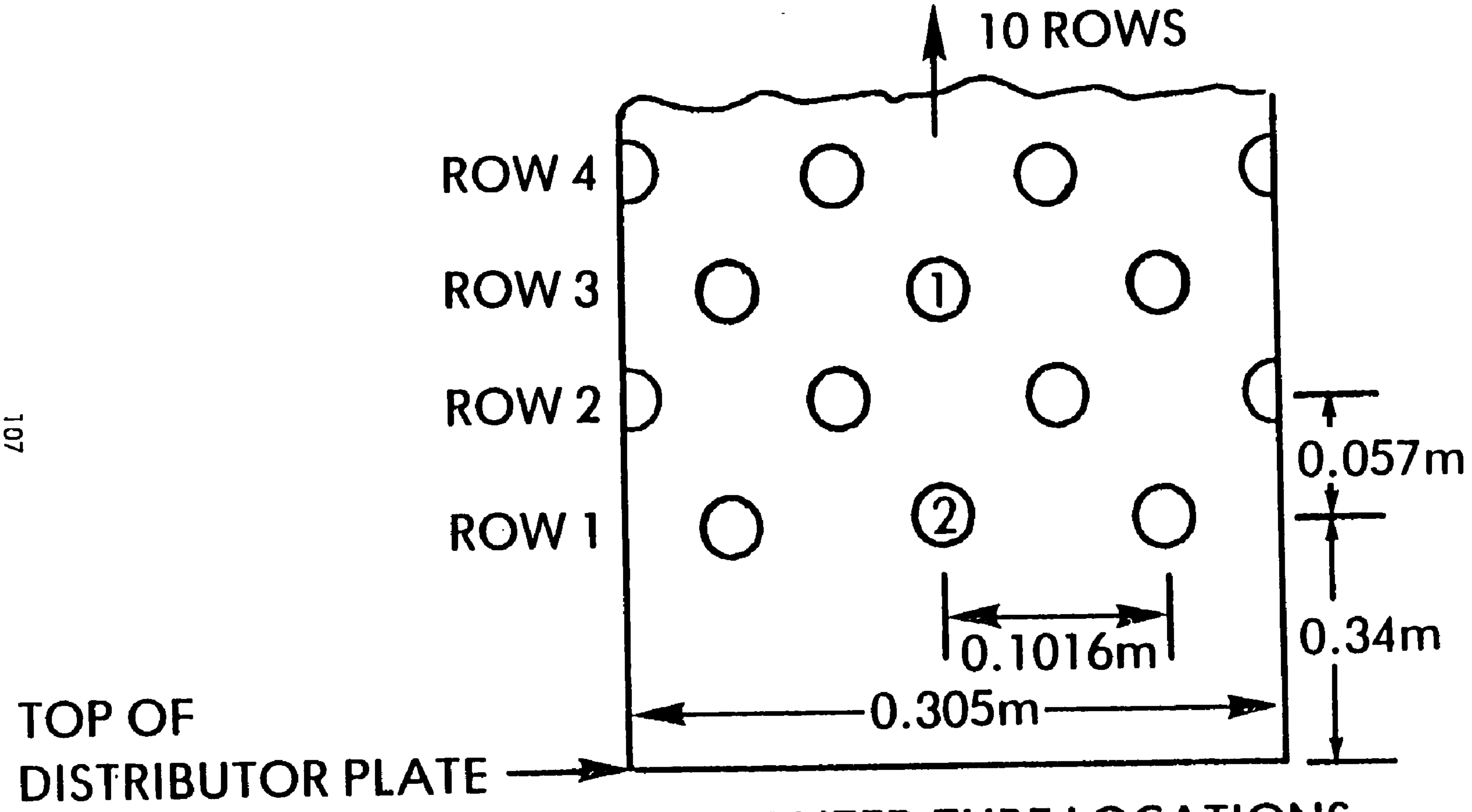

Figure 9 INSTRUMENTED TUBE LOCATIONS IN 10-ROW BARE-TUBE BUNDLE

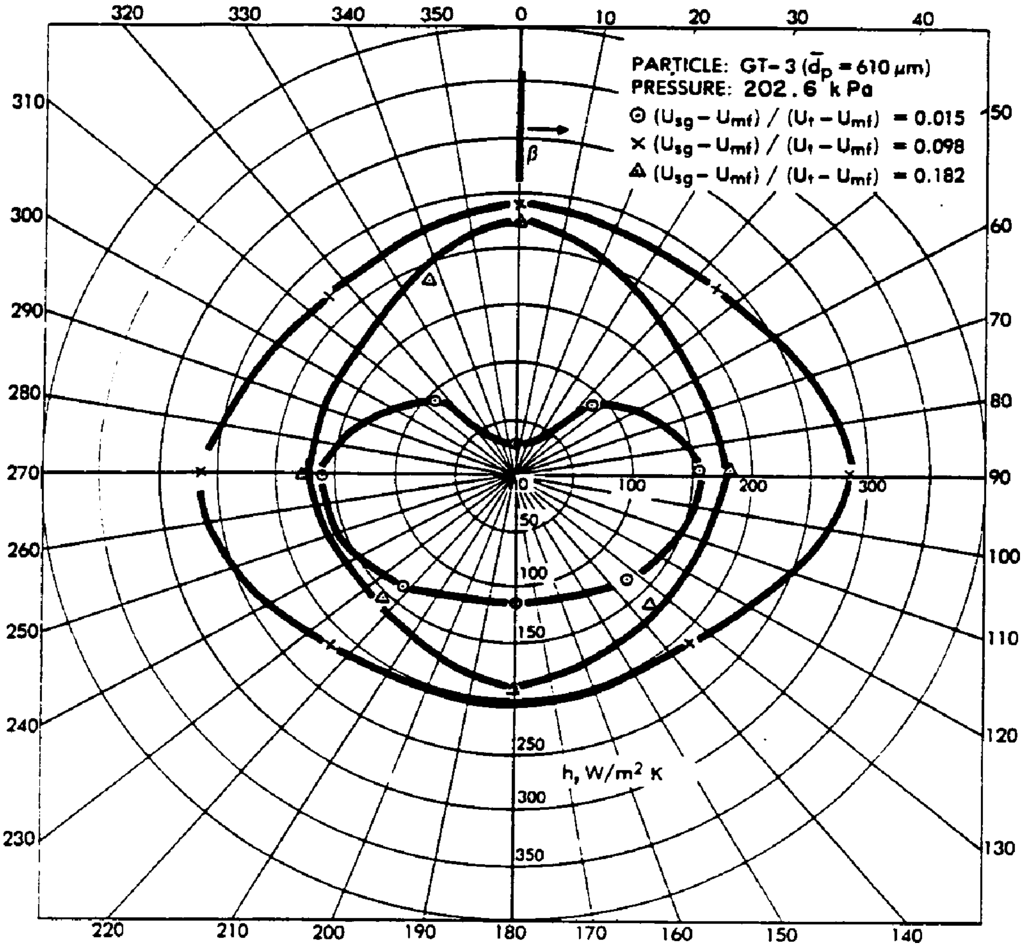

Figure 10 Local heat transfer coefficients around a single horizontal tube at different gas flow rates

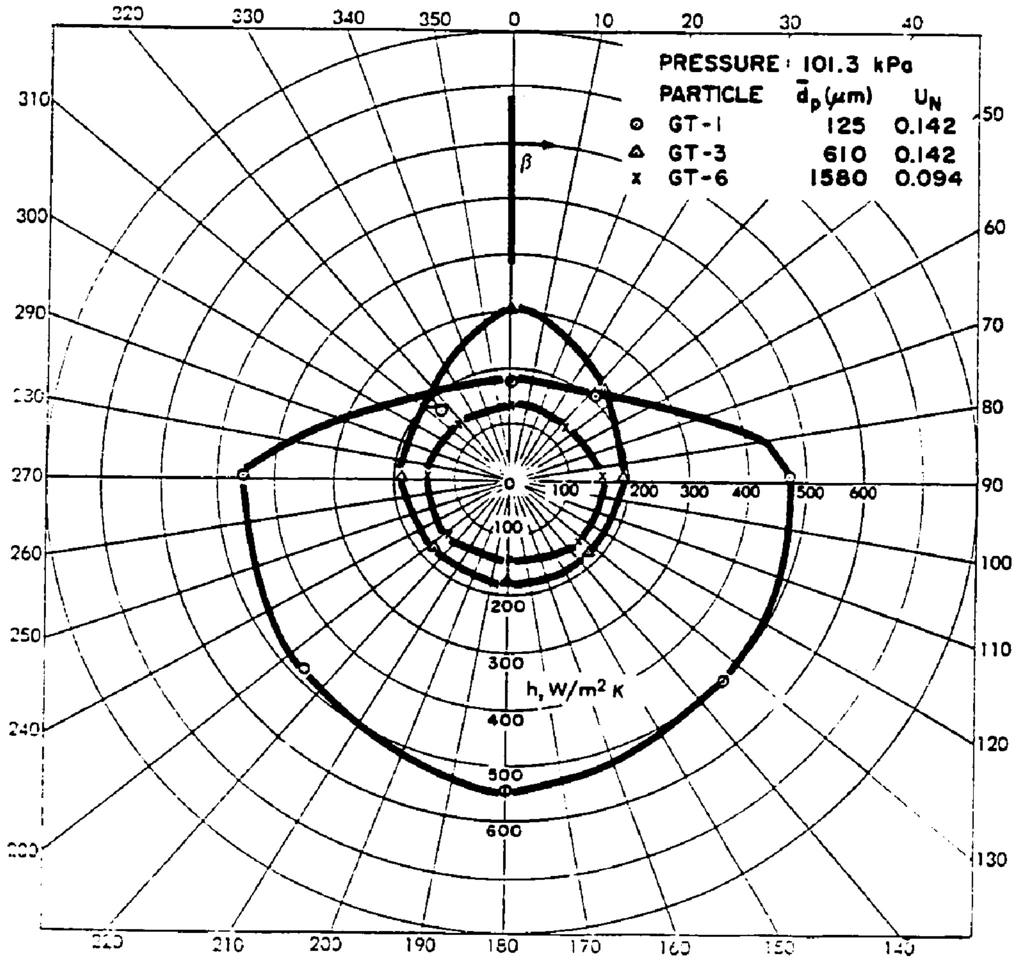

Figure 11 Local heat transfer coefficients around a single horizontal tube for different particle sizes

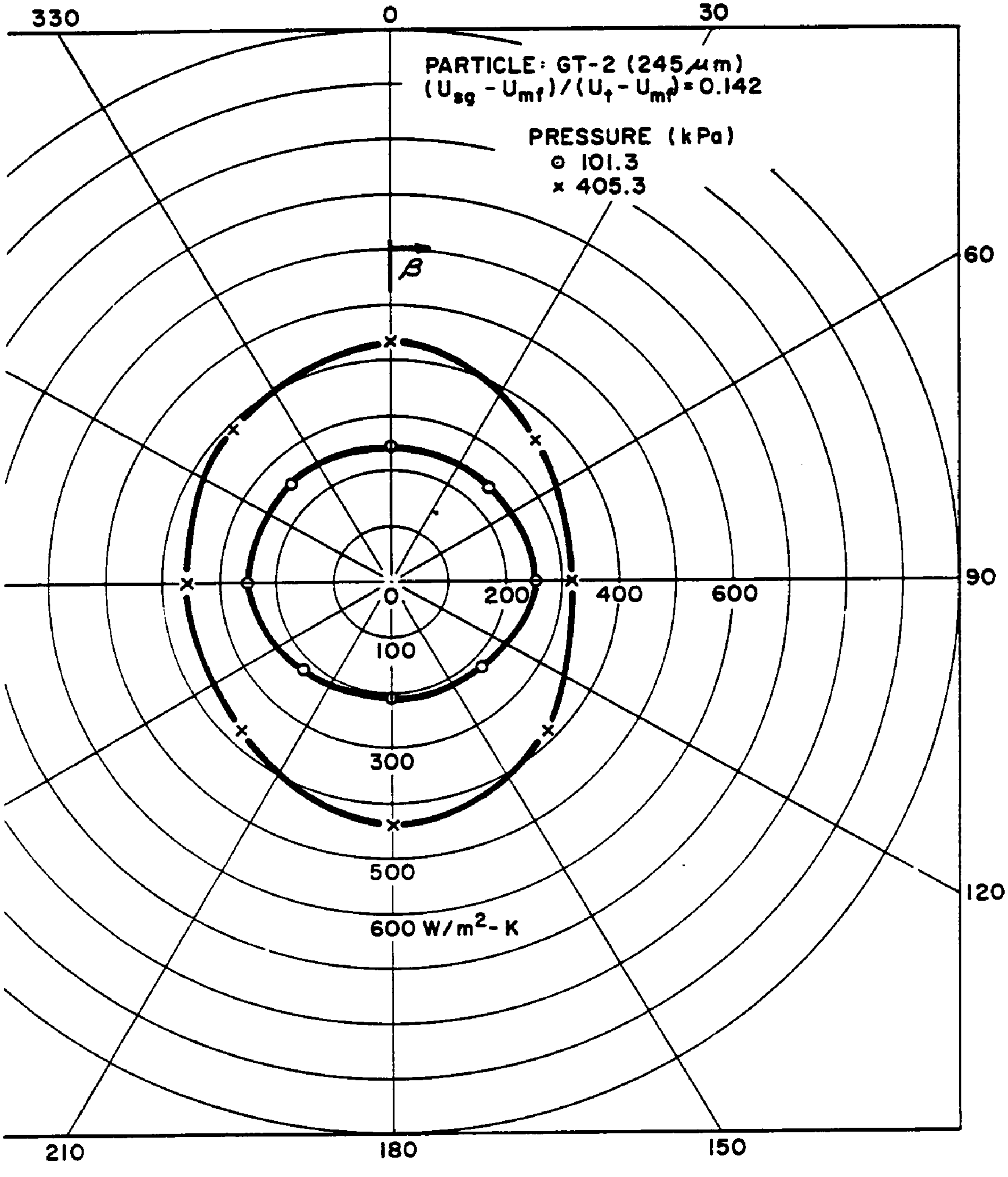

Figure 12 Effect of pressure on local coefficients for small particles

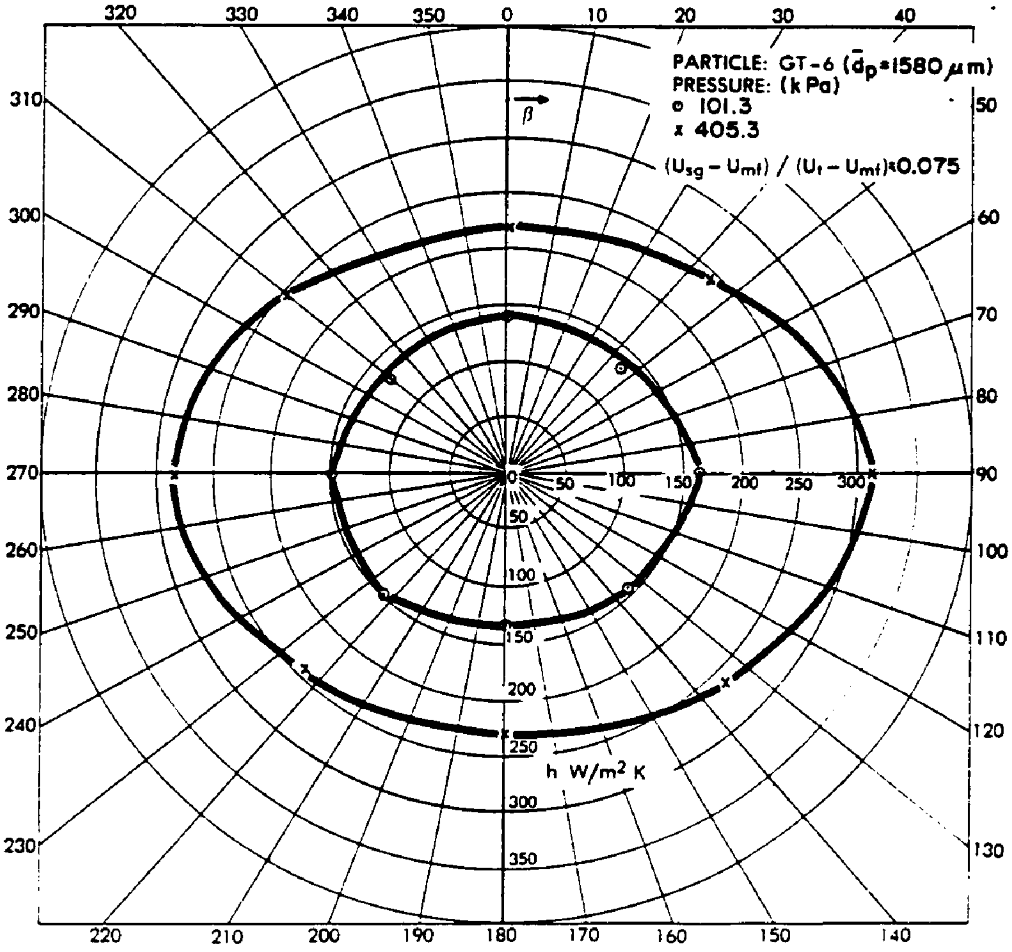

Figure 13 Effect of pressure on local coefficients for large particles

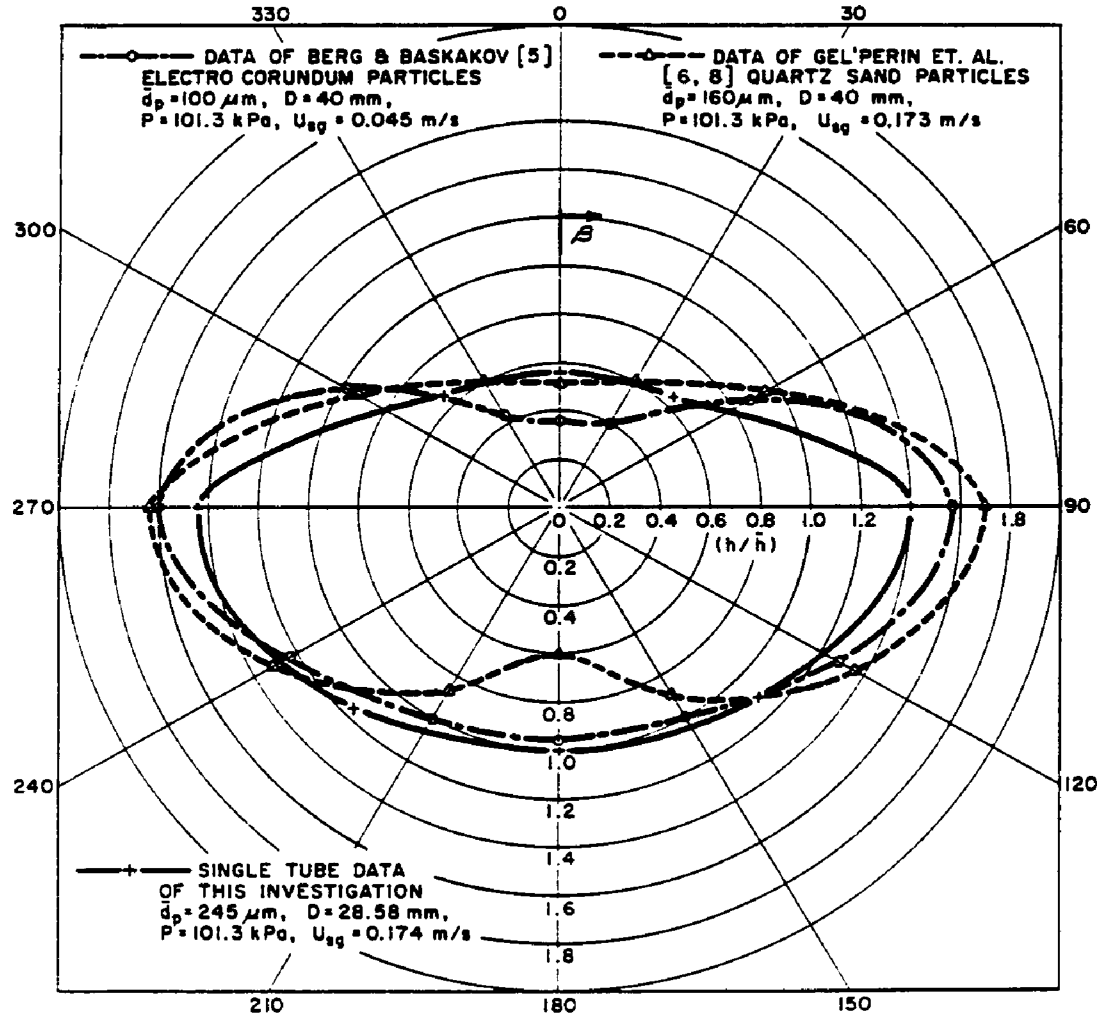

Figure 14 Relative heat transfer coefficients around a single horizontal tube

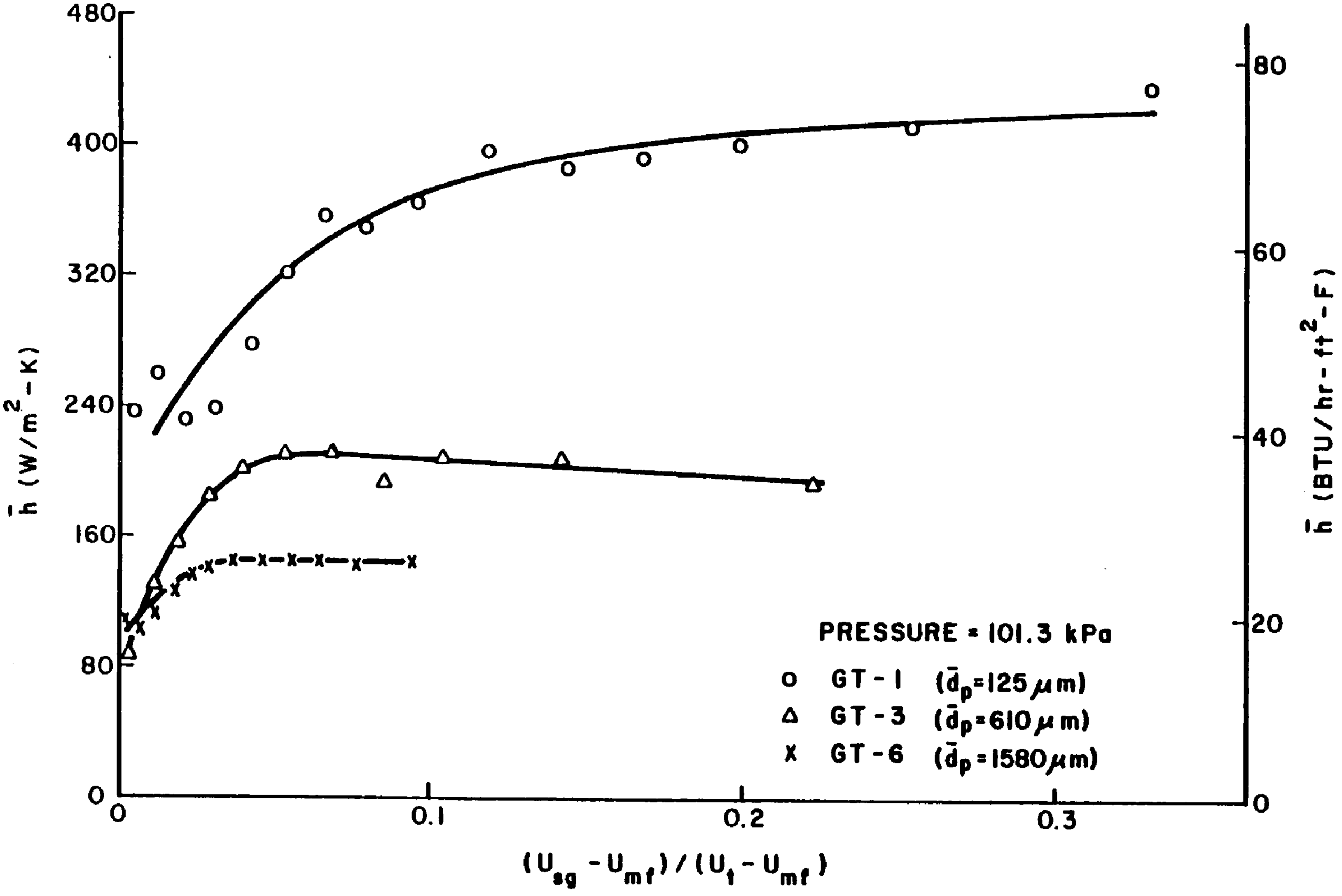

Figure 15 Average heat transfer coefficients for a single tube with particles of different sizes

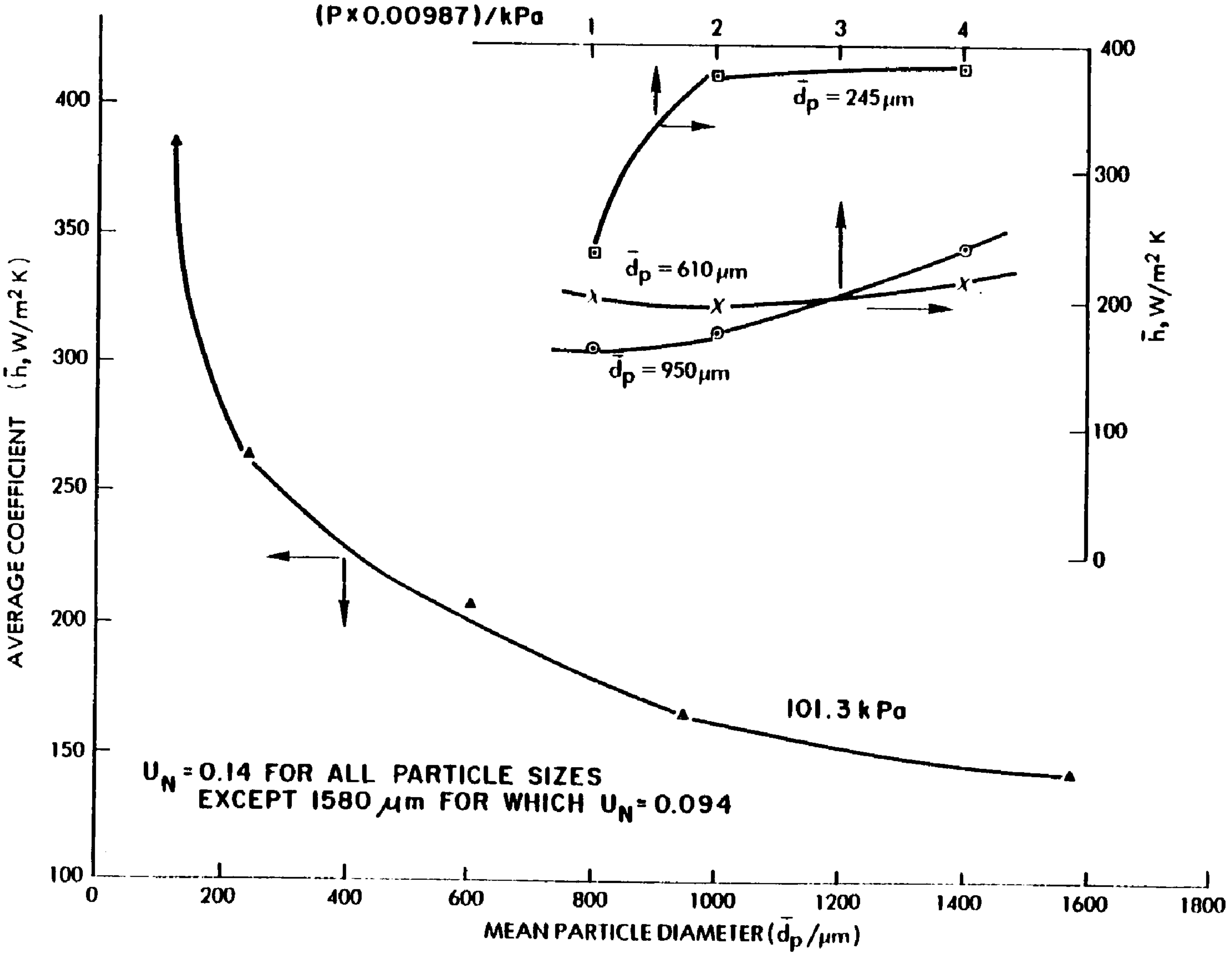

Figure 16 Effect of particle size and system pressure on average coefficients for a single tube

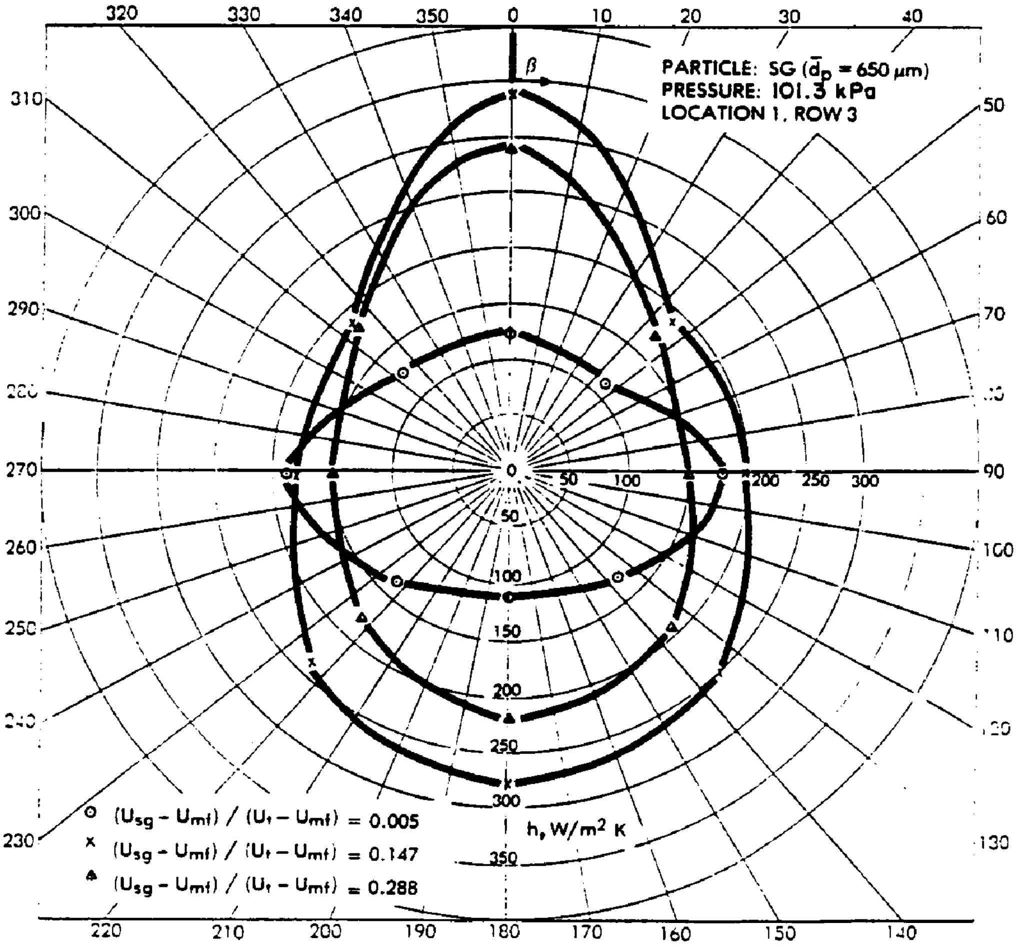

Figure 17 Local heat transfer coefficients for a tube in the inner-row position within a tube bundle

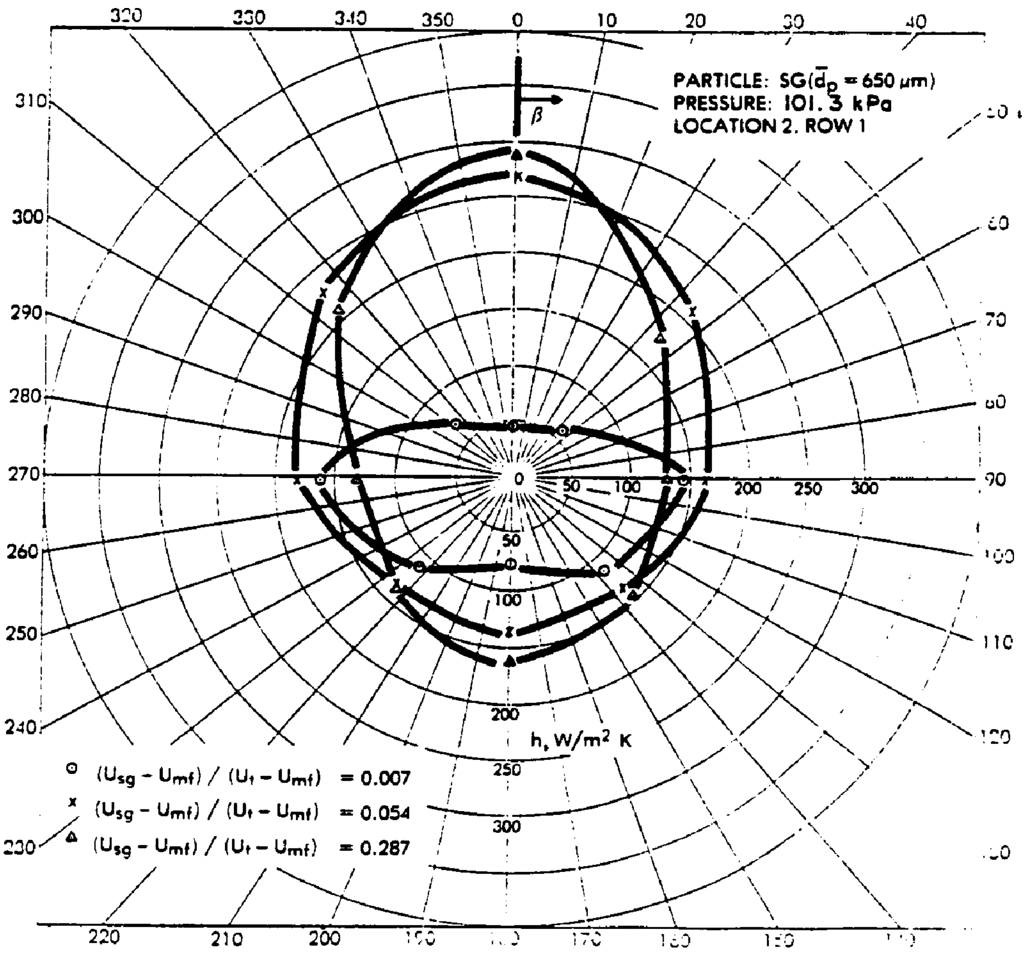

Figure 18 Local heat transfer coefficients for a tube in the bottom-row position within a tube bundle

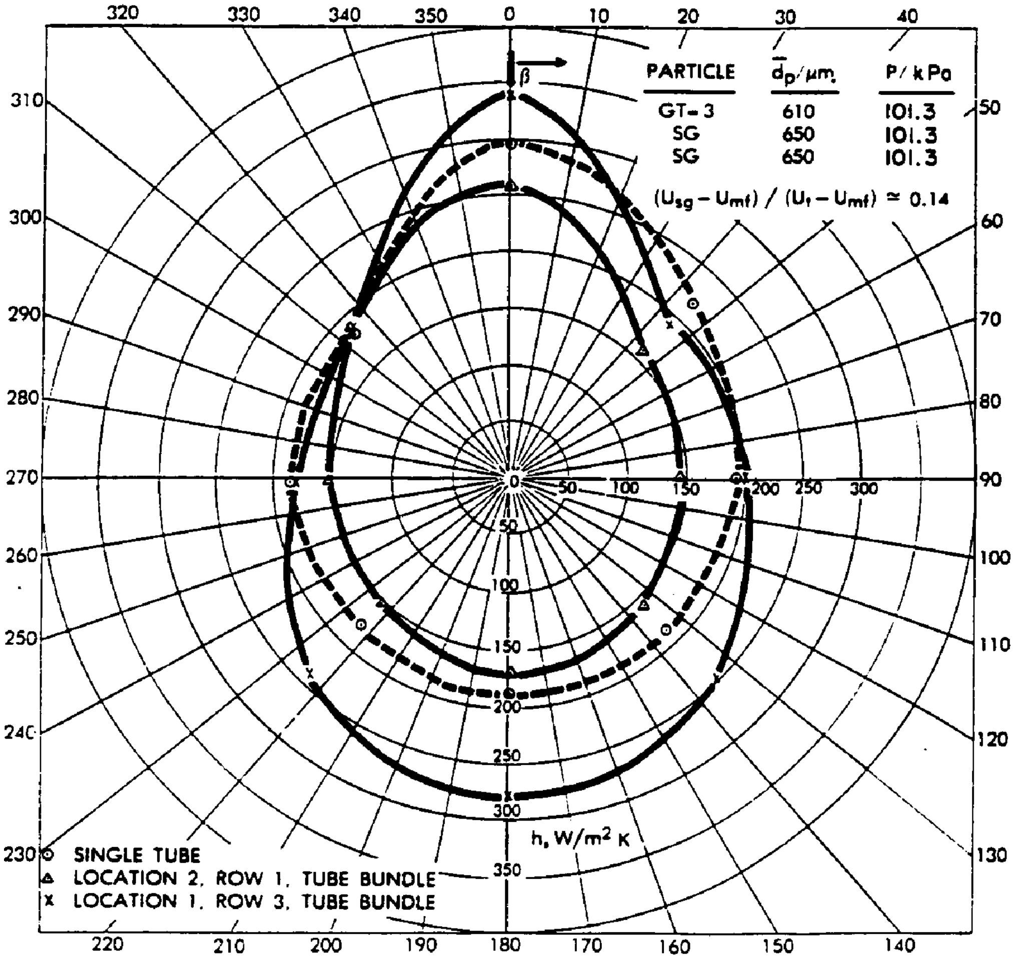

Figure 19 Local coefficients around a single tube and around a test tube at two locations within a tube bundle

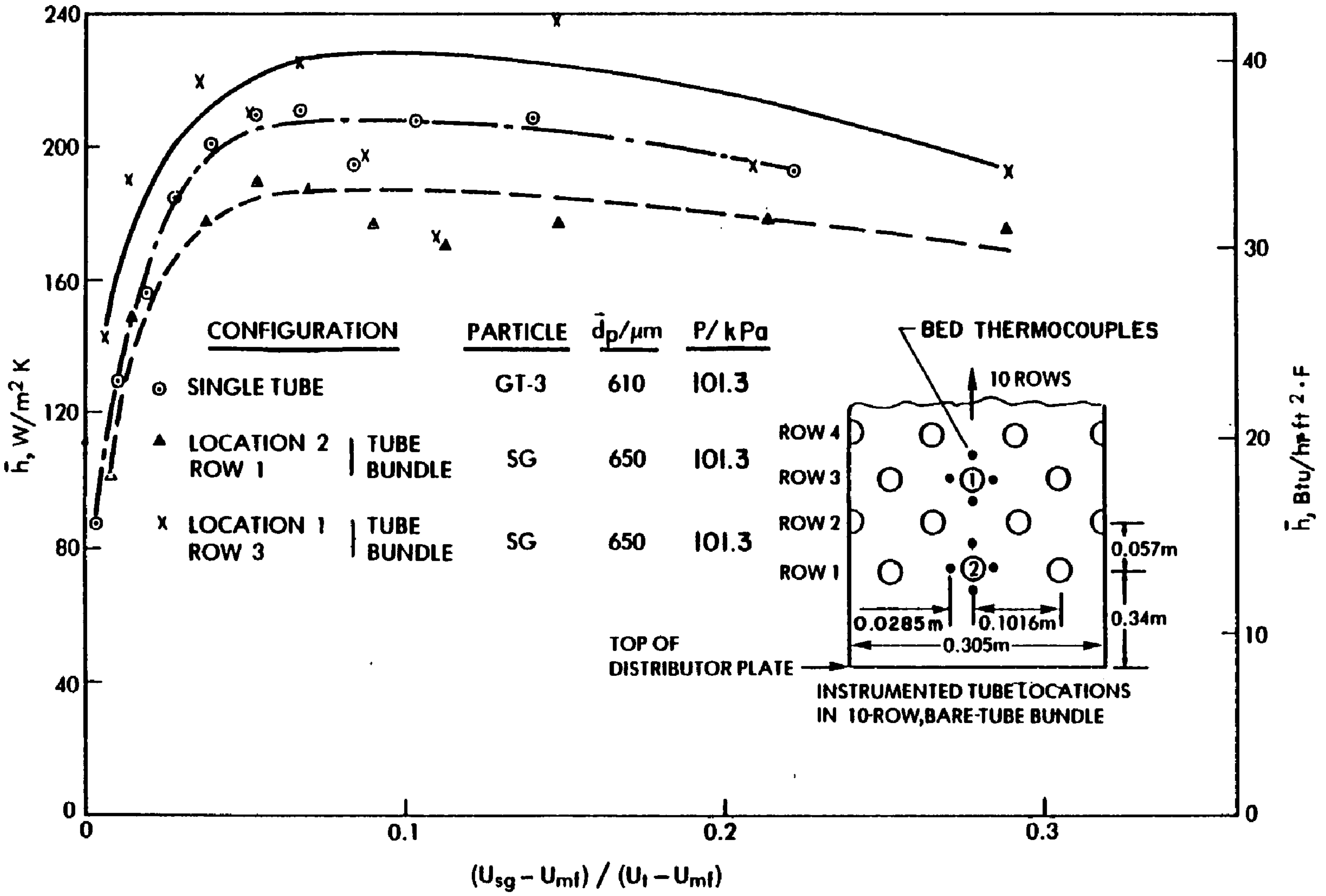

Figure 20 Average coefficients for a single tube and for a test tube at two locations within a tube bundle

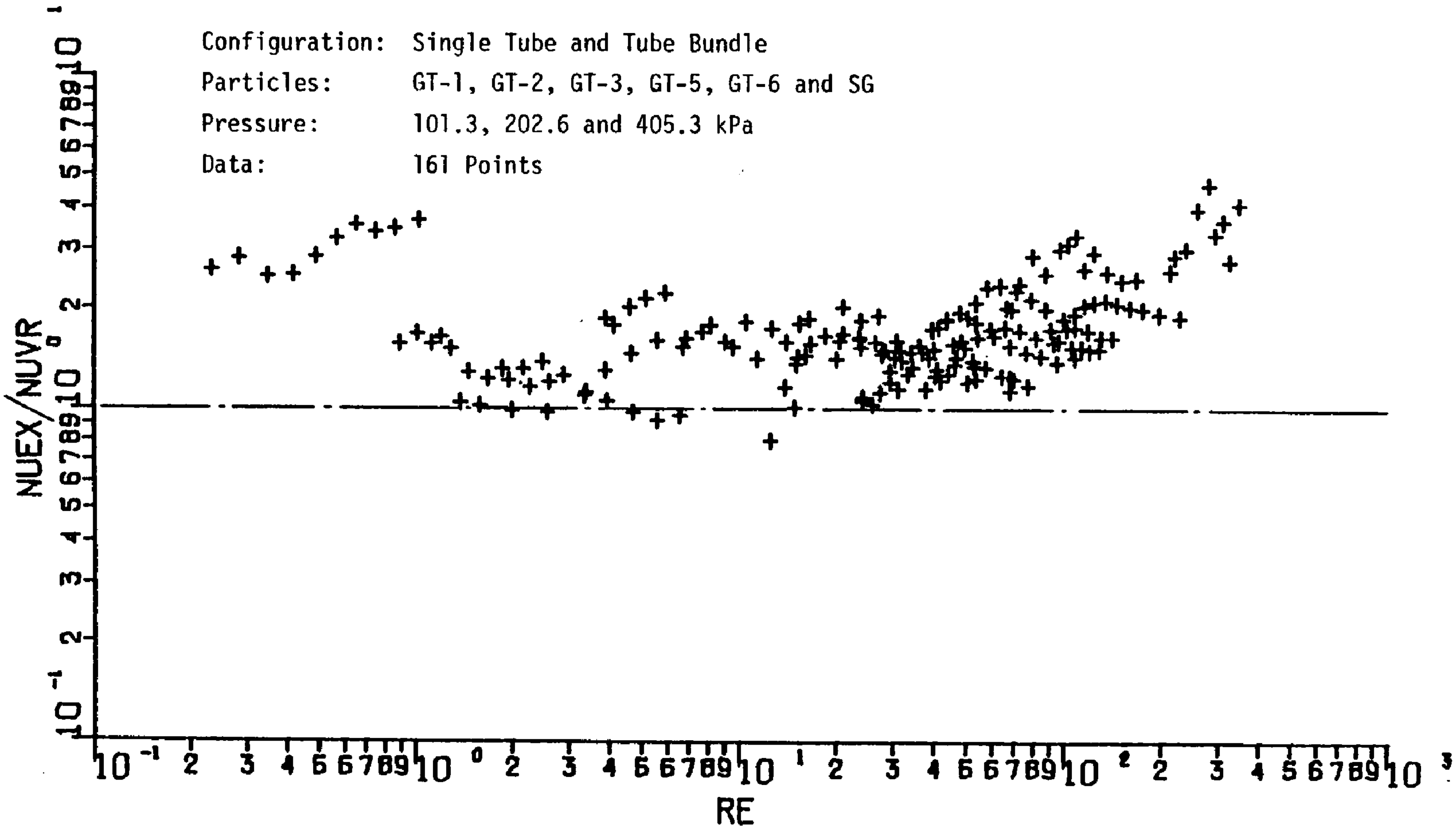
Configuration: Single Tube and Tube Bundle

Particles: GT-1, GT-2, GT-3, GT-5, GT-6 and SG

Pressure: 101.3, 202.6 and 405.3 kPa

Data: 161 Points

Figure 21 Comparison of experimental data for average heat transfer coefficient with Vreedenberg's correlation

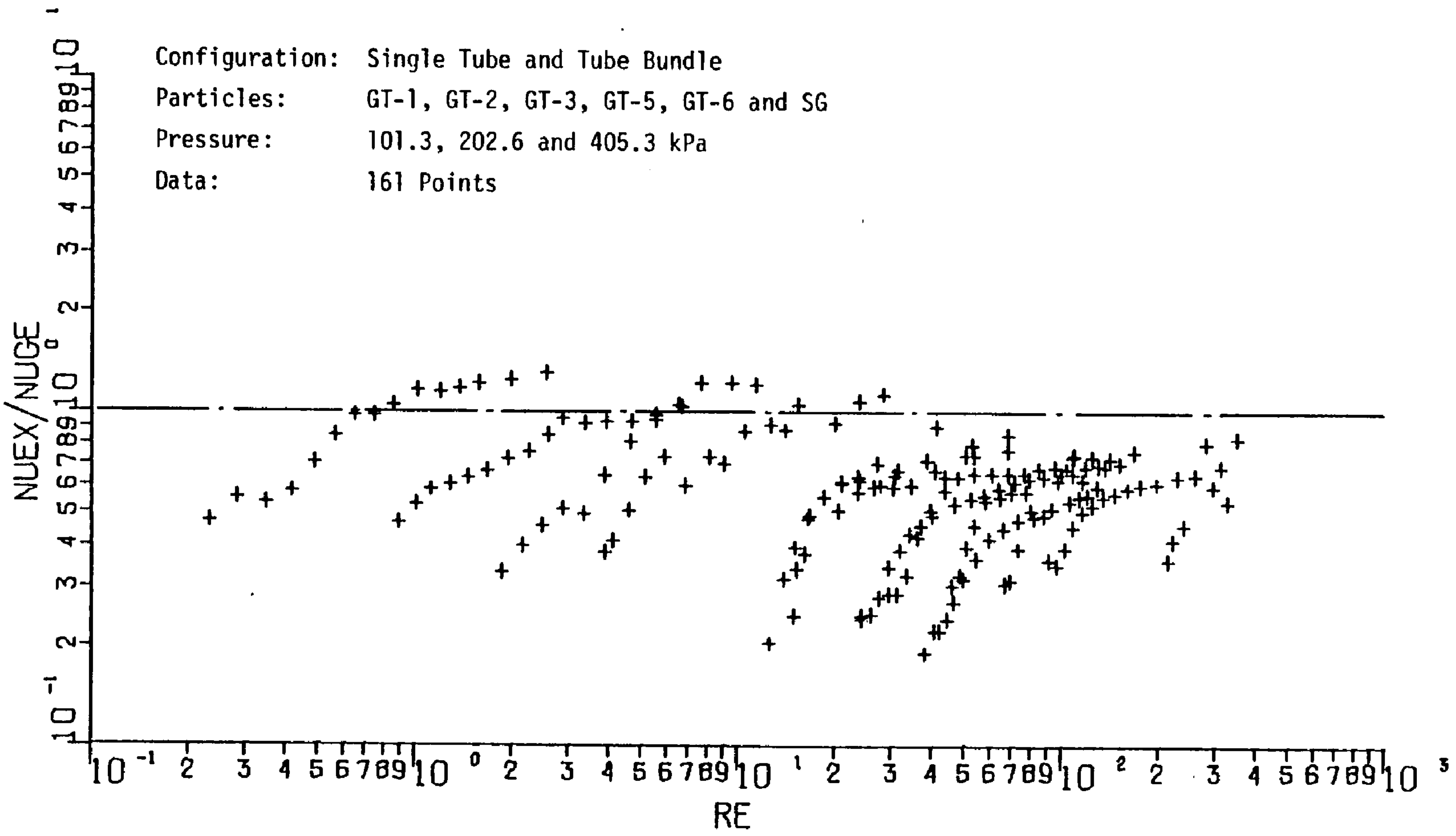

Figure 22 Comparison of experimental data for average heat transfer coefficient with the correlation of Gel'perin et al.

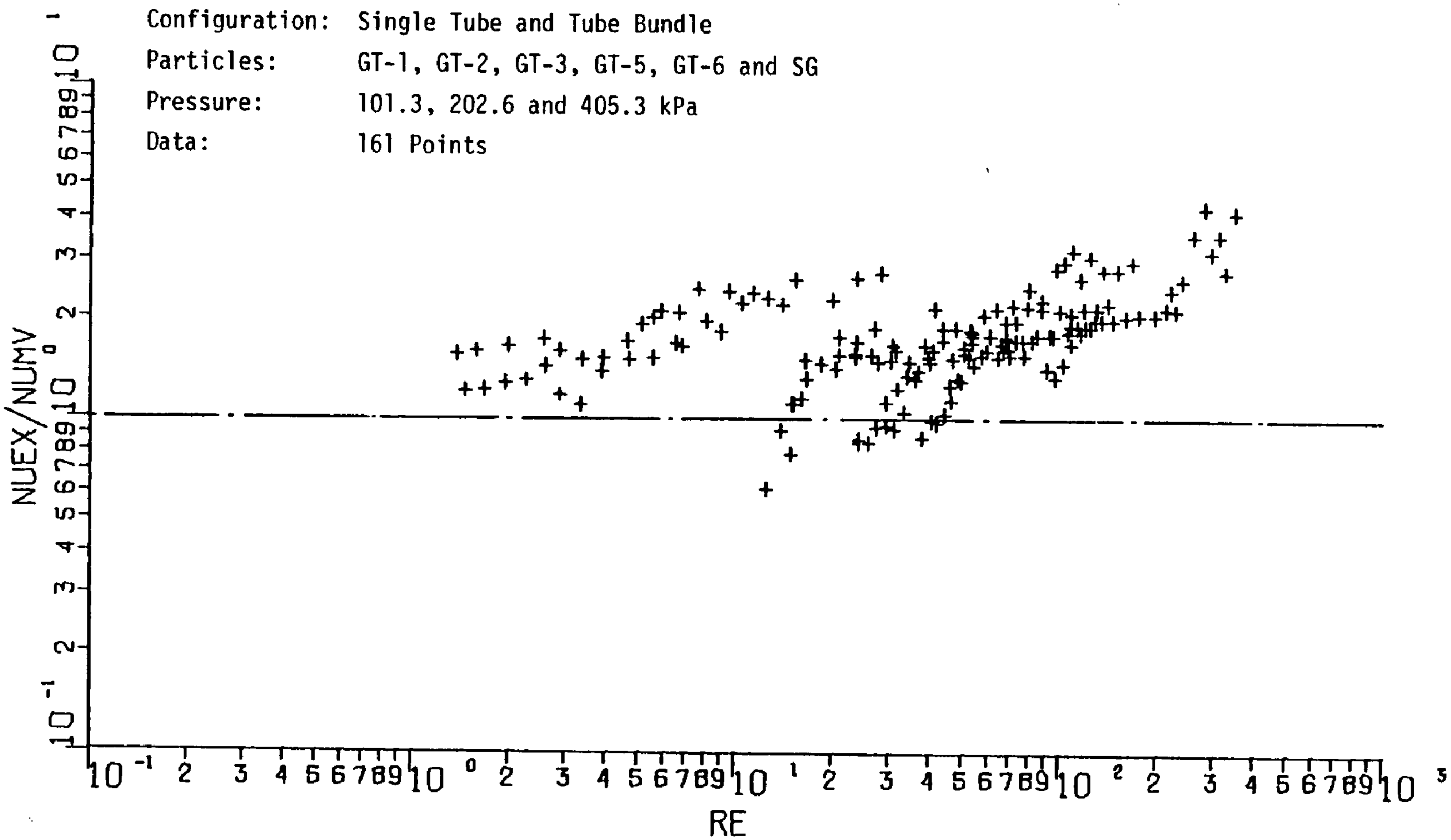

Configuration: Single Tube and Tube Bundle

Particles: GT-1, GT-2, GT-3, GT-5, GT-6 and SG

Pressure: 101.3, 202.6 and 405.3 kPa

Data: 161 Points

Figure 23 Comparison of experimental data for average heat transfer coefficient with modified Vreedenberg's correlation

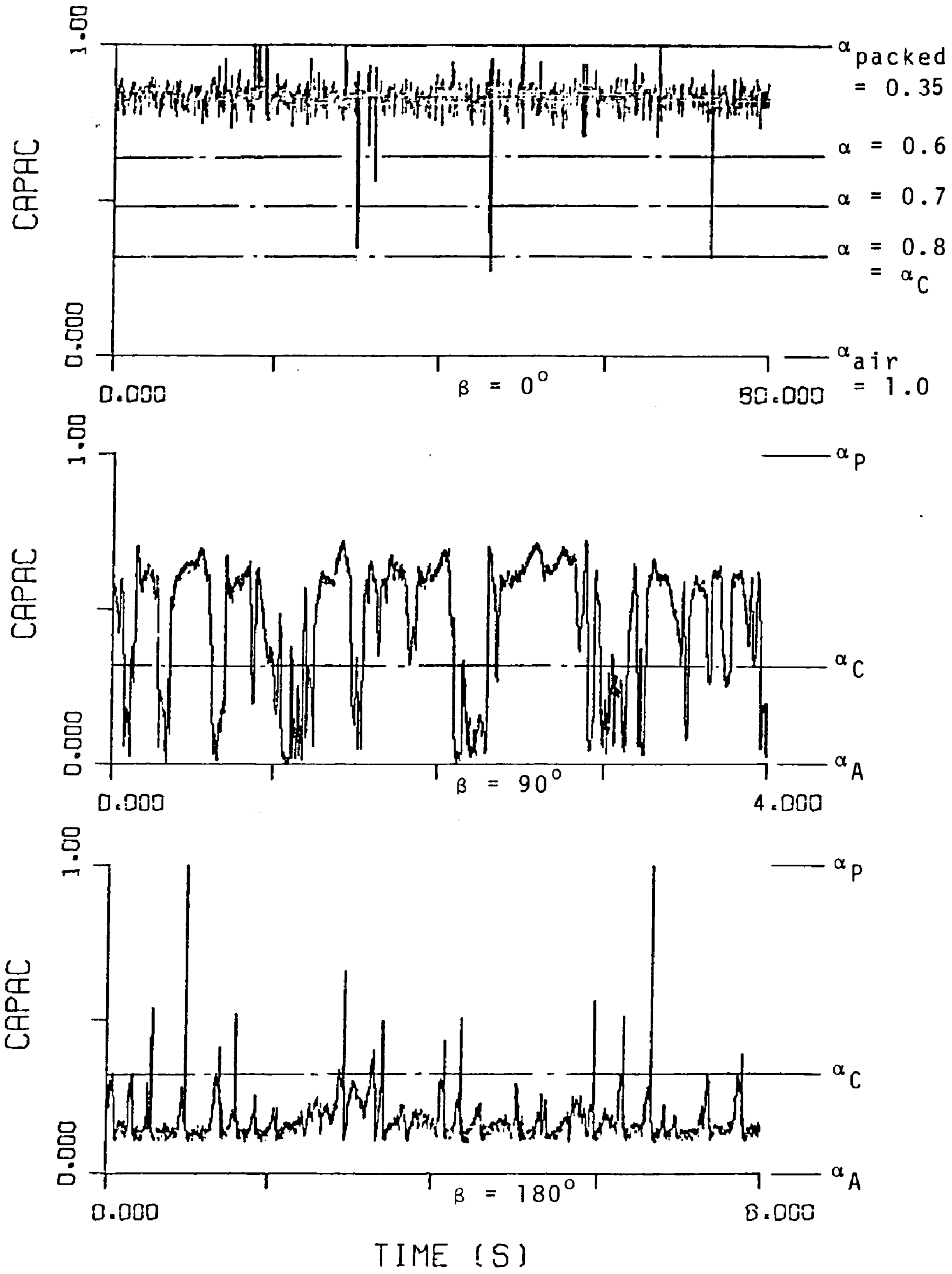

Particle: GT-2, Pressure: 101.3 kPa, $U_N \approx 0.01$
Figure 24 Capacitance traces at low gas flow rate

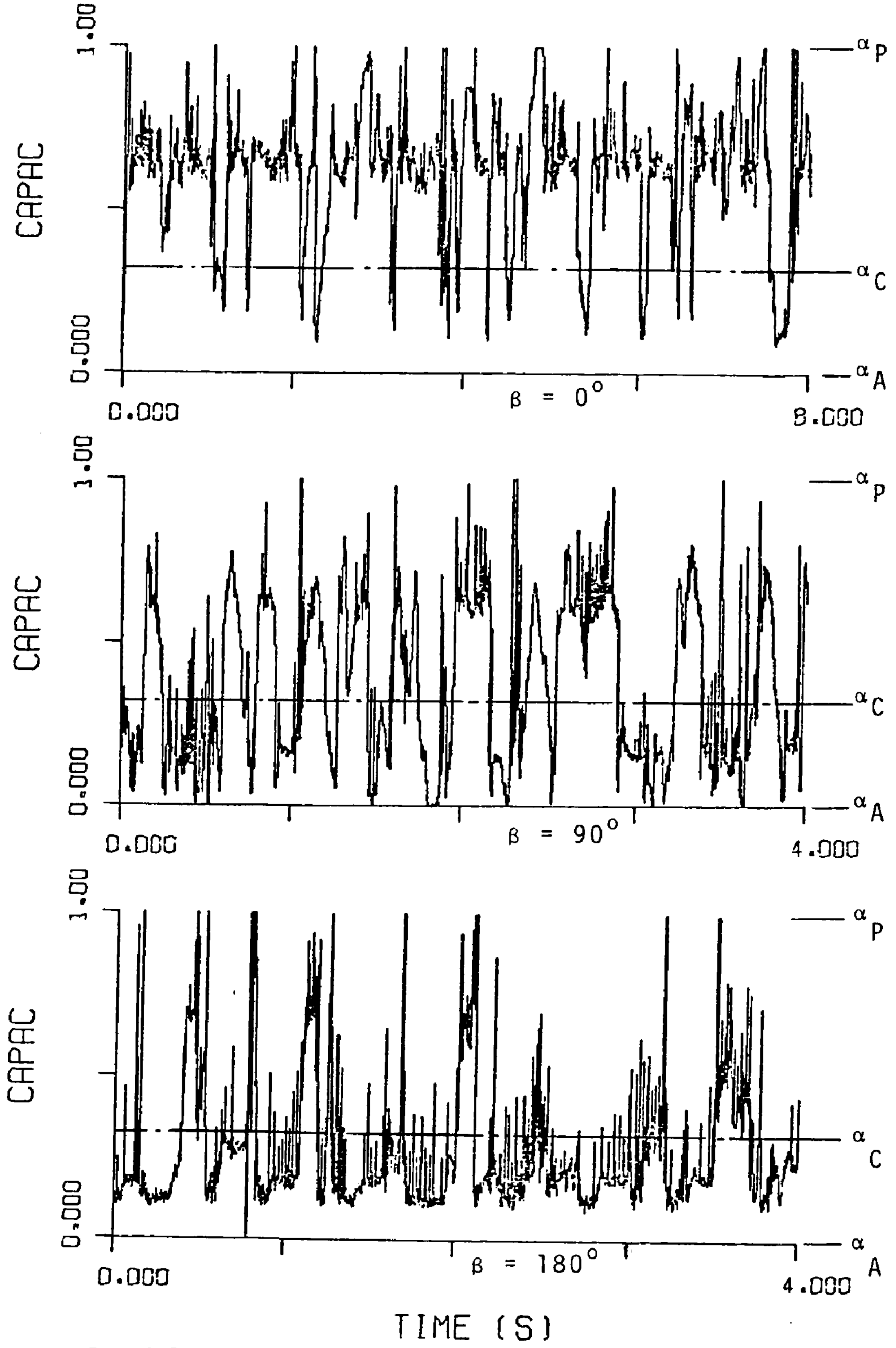

Particle: GT-2, Pressure: 101.3 kPa, $U_N \simeq 0.36$

Figure 25 Capacitance traces at high gas flow rate

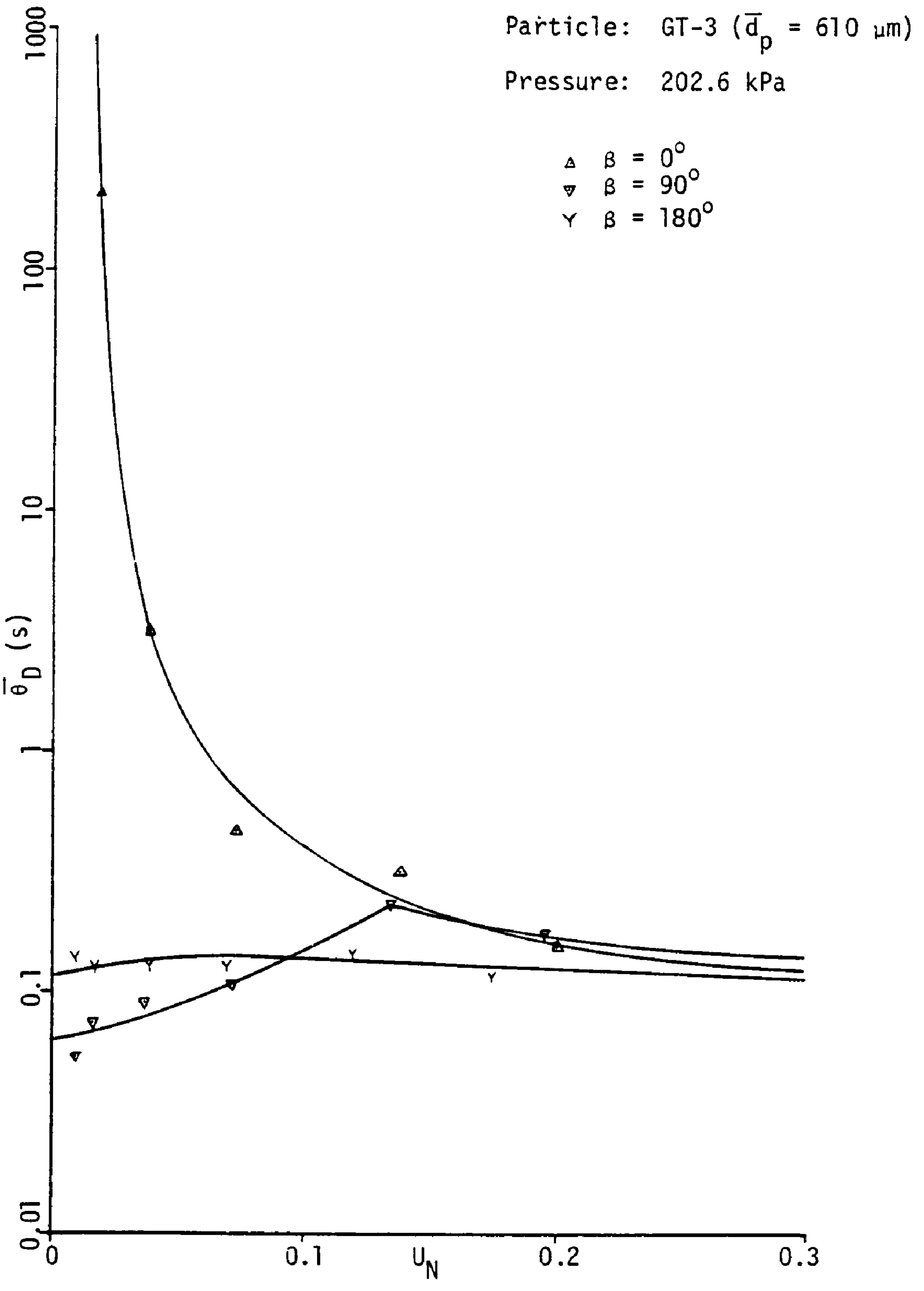

Figure 26 Effect of gas flow rate on dense phase root-square average residence time around a single tube

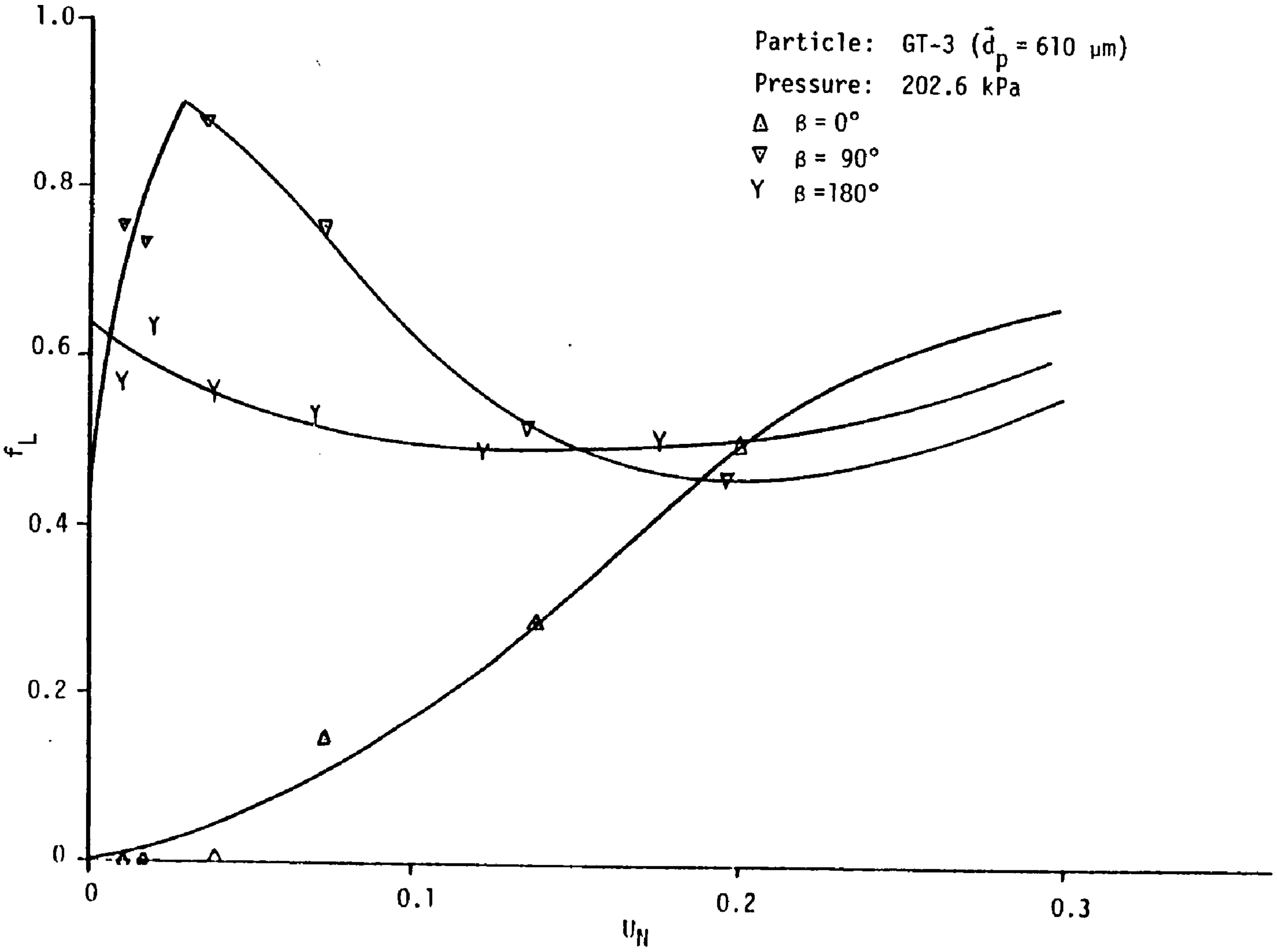

Figure 27 Effect of gas flow rate on fractional contact time of lean phase around a single tube

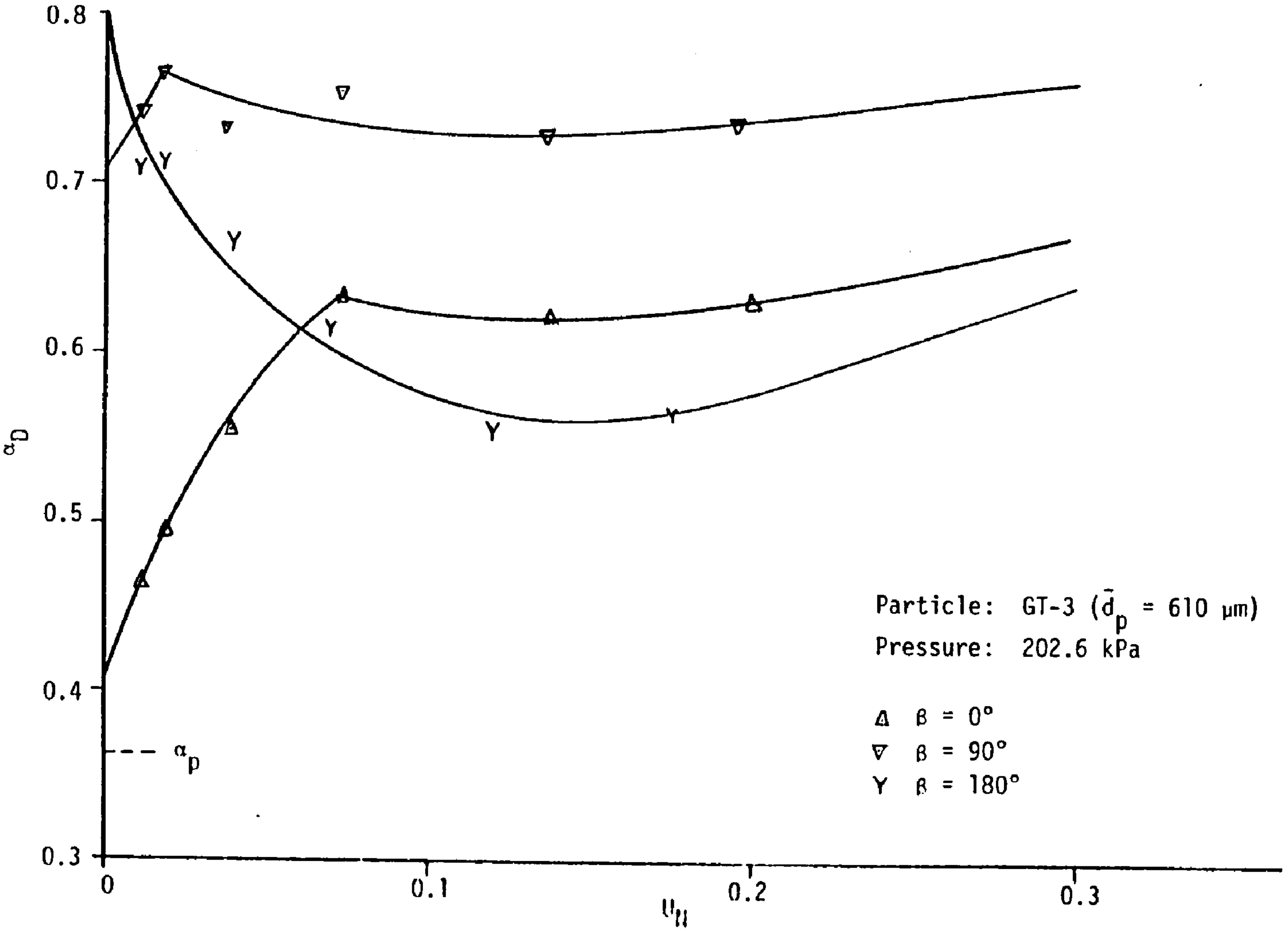

Figure 28 Effect of gas flow rate on dense phase void fraction around a single tube

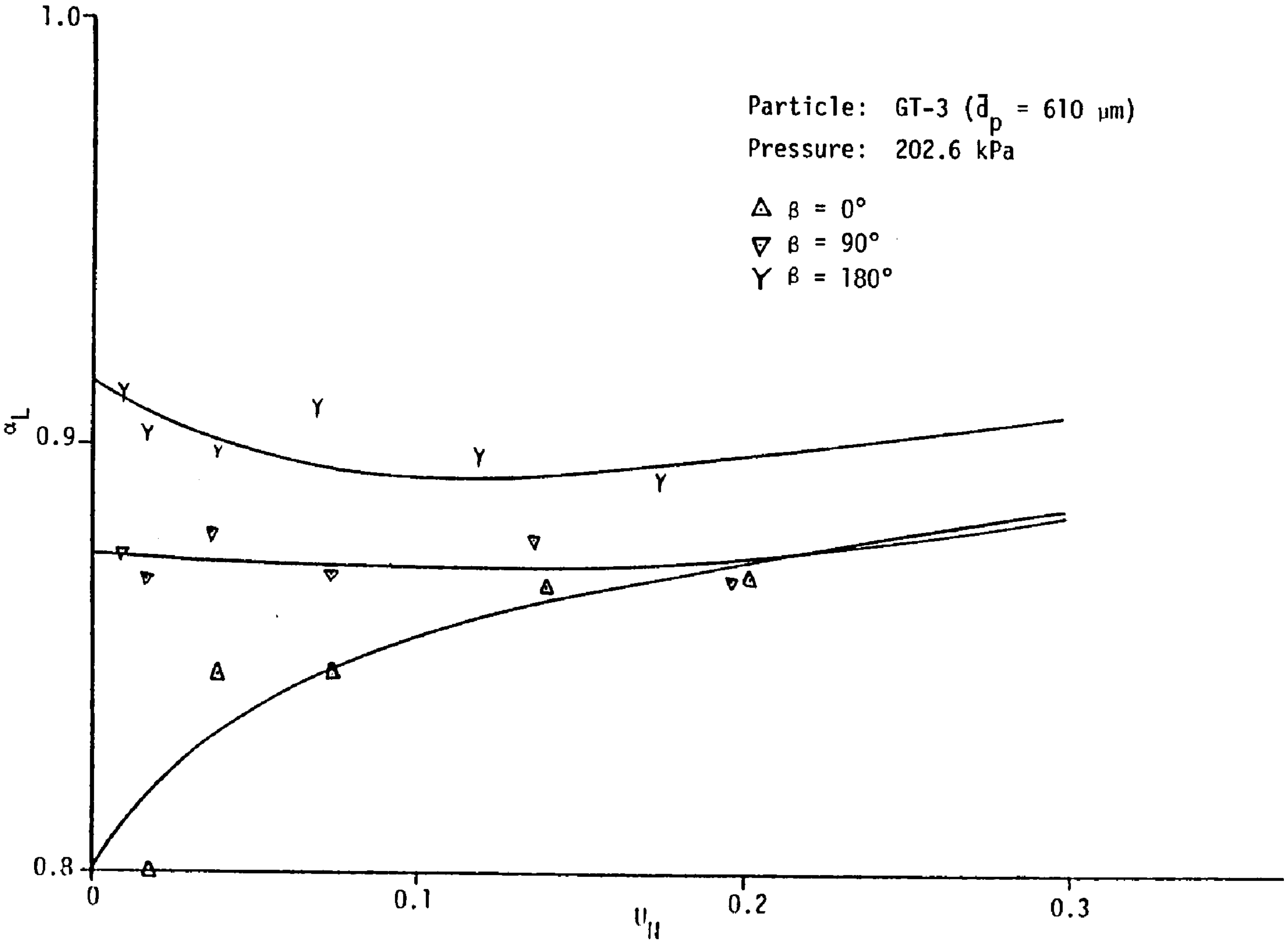

Figure 29 Effect of gas flow rate on lean phase void fraction around a single tube

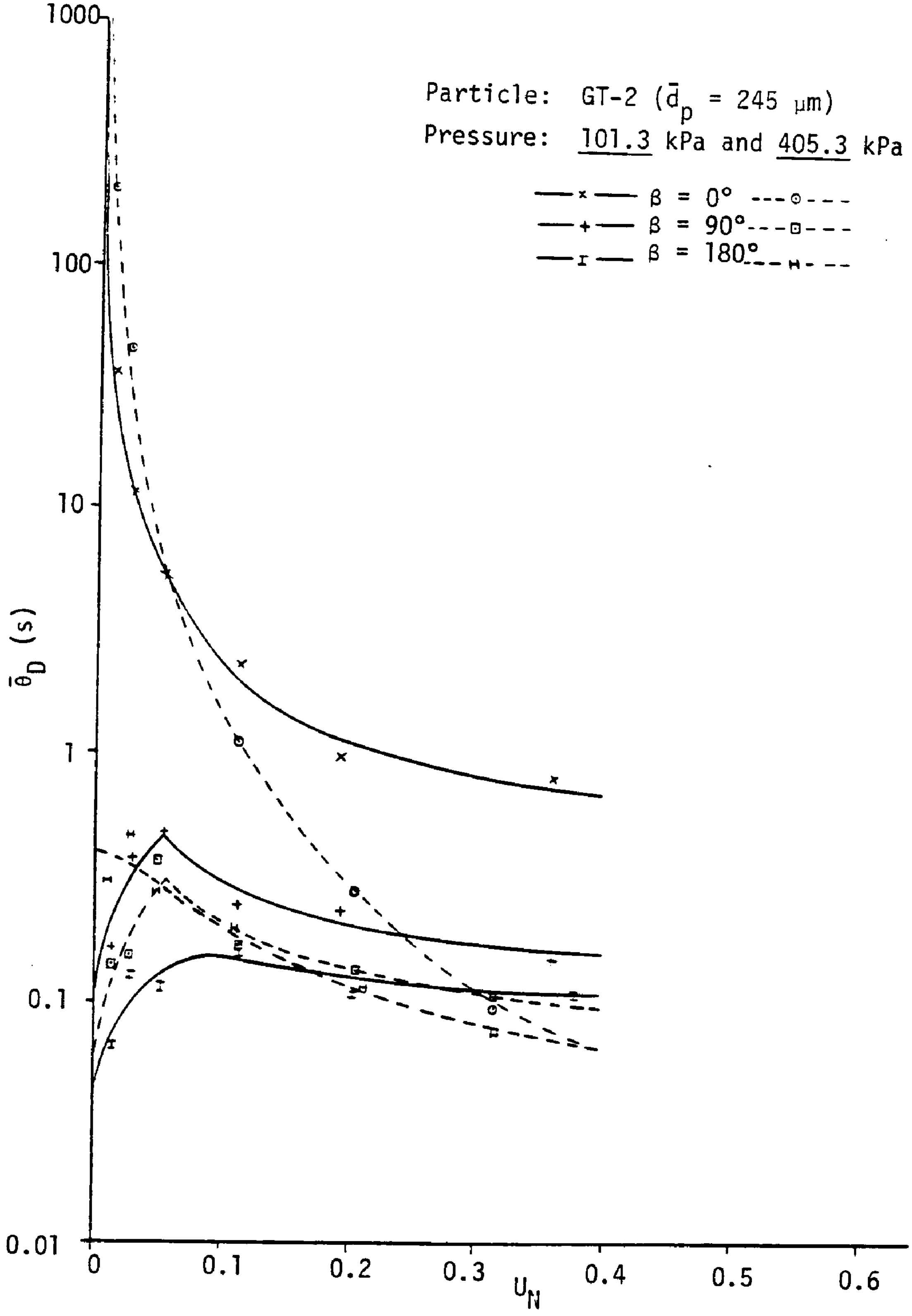

Figure 30 Effect of pressure on root-square-average residence time of dense phase for small particles

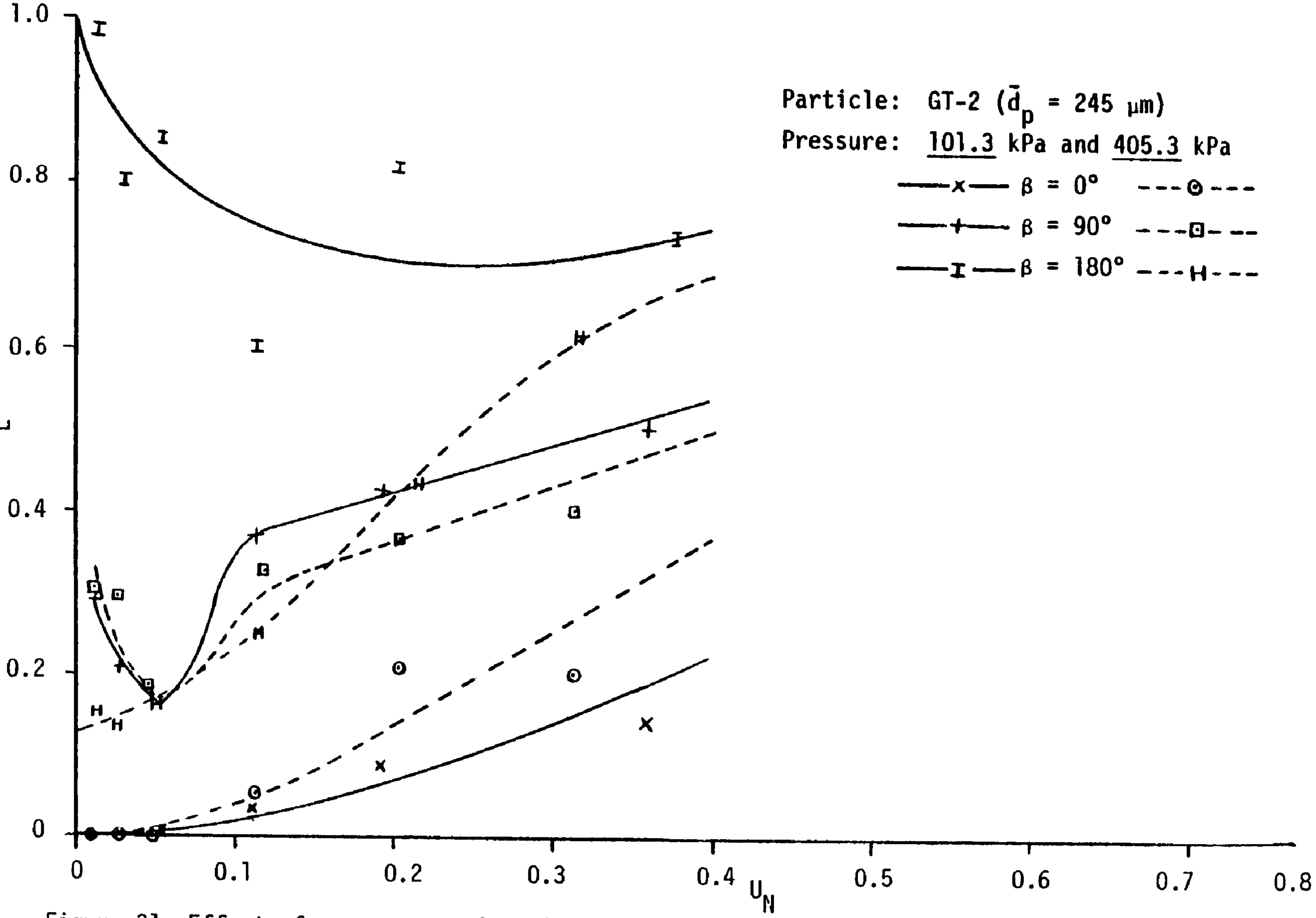

Figure 31 Effect of pressure on fractional contact time of lean phase for small particles

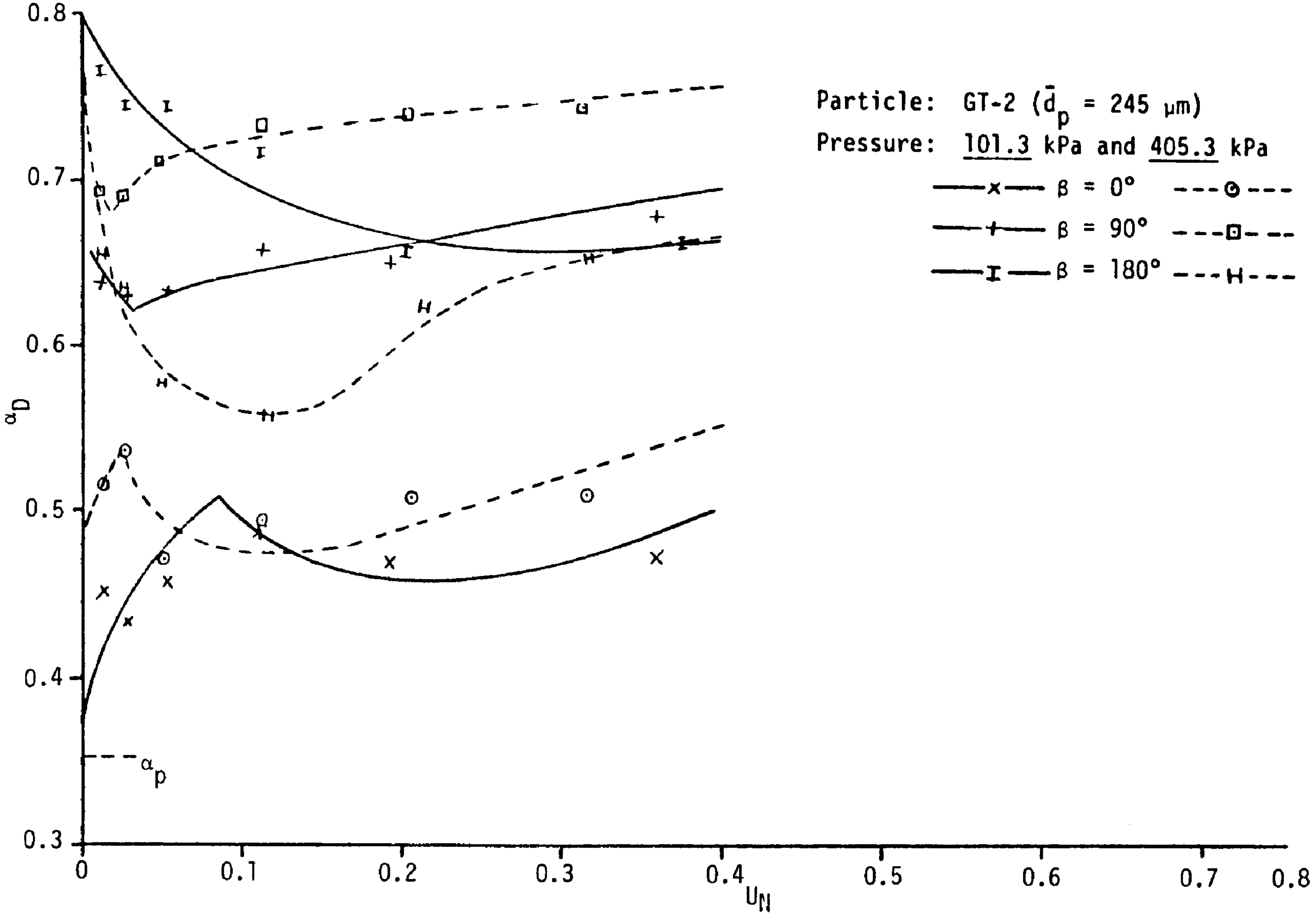

Figure 32 Effect of pressure on dense phase void fraction for small particles

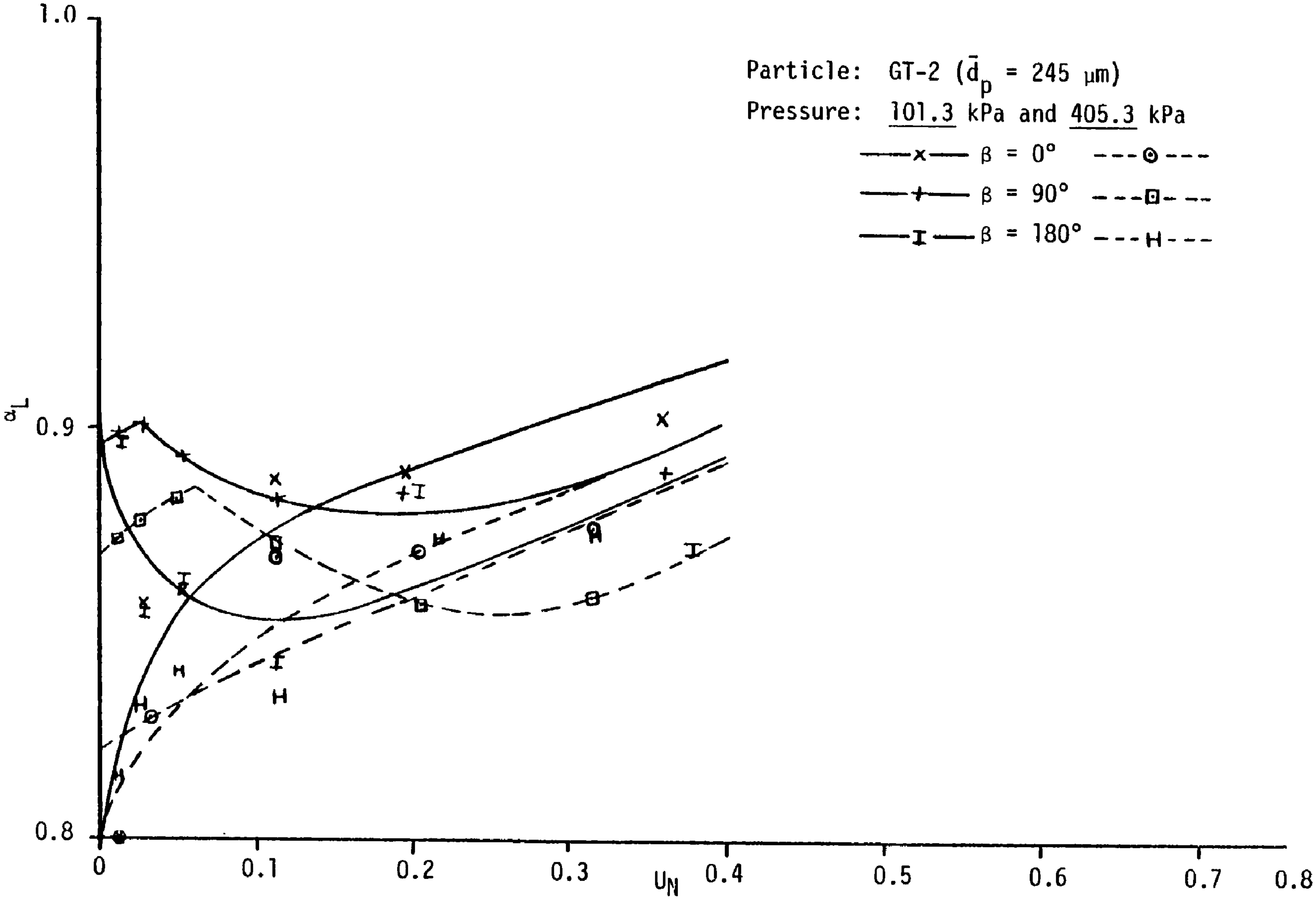

Figure 33 Effect of pressure on lean phase void fraction for small particles

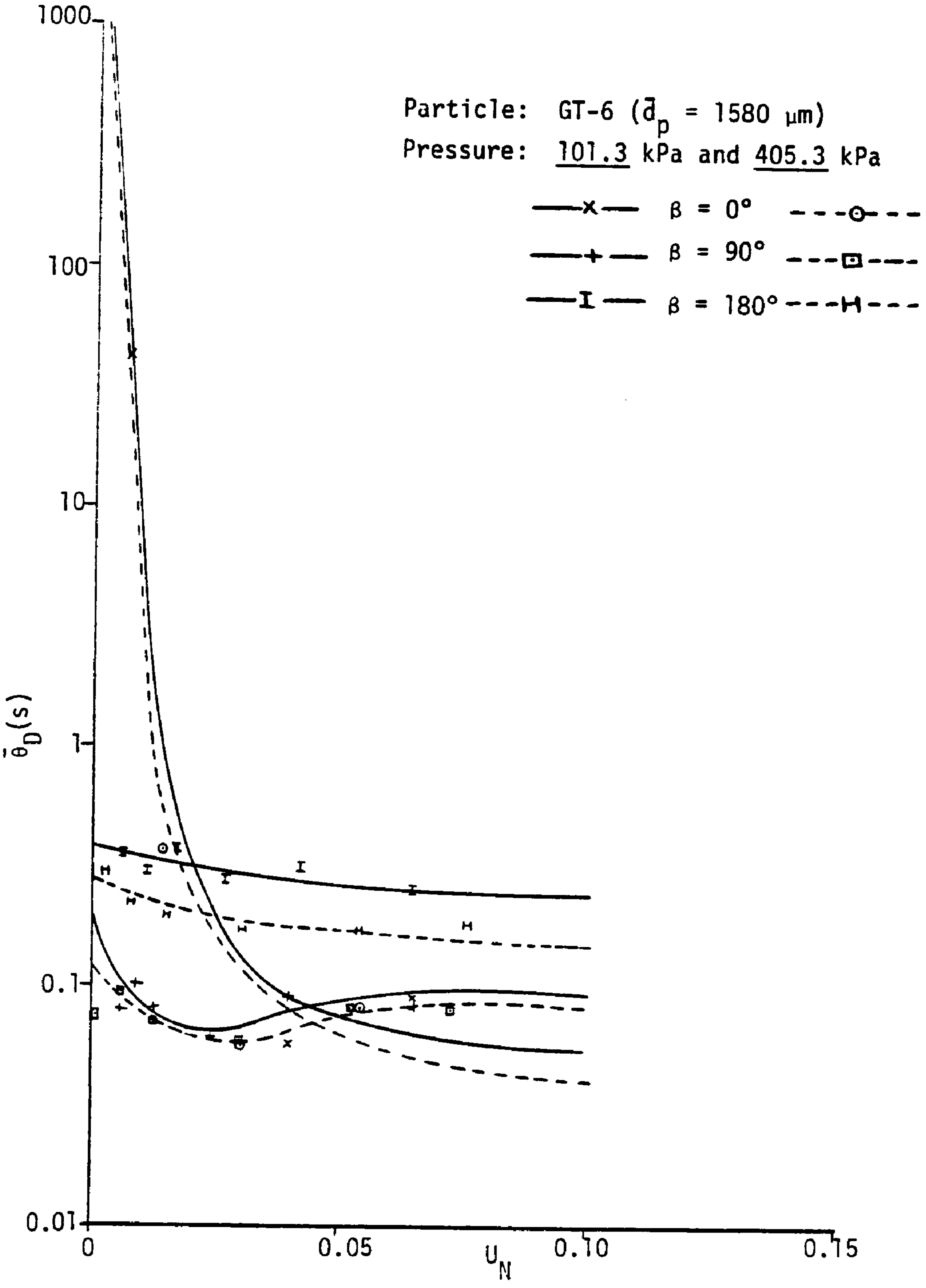

Figure 34 Effect of pressure on dense phase root-square average residence time for large particles

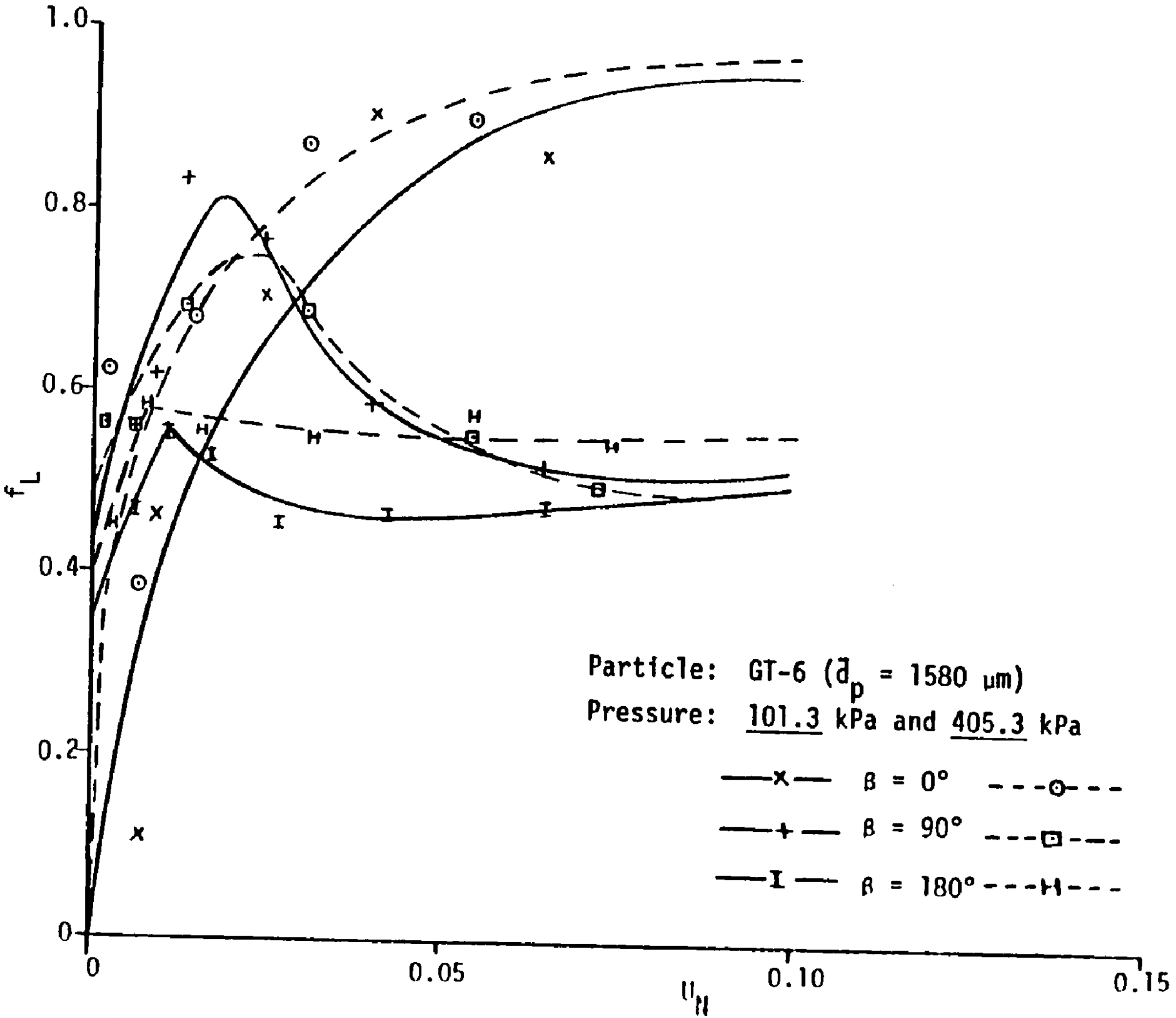

Figure 35 Effect of pressure on lean phase fractional contact time for large particles

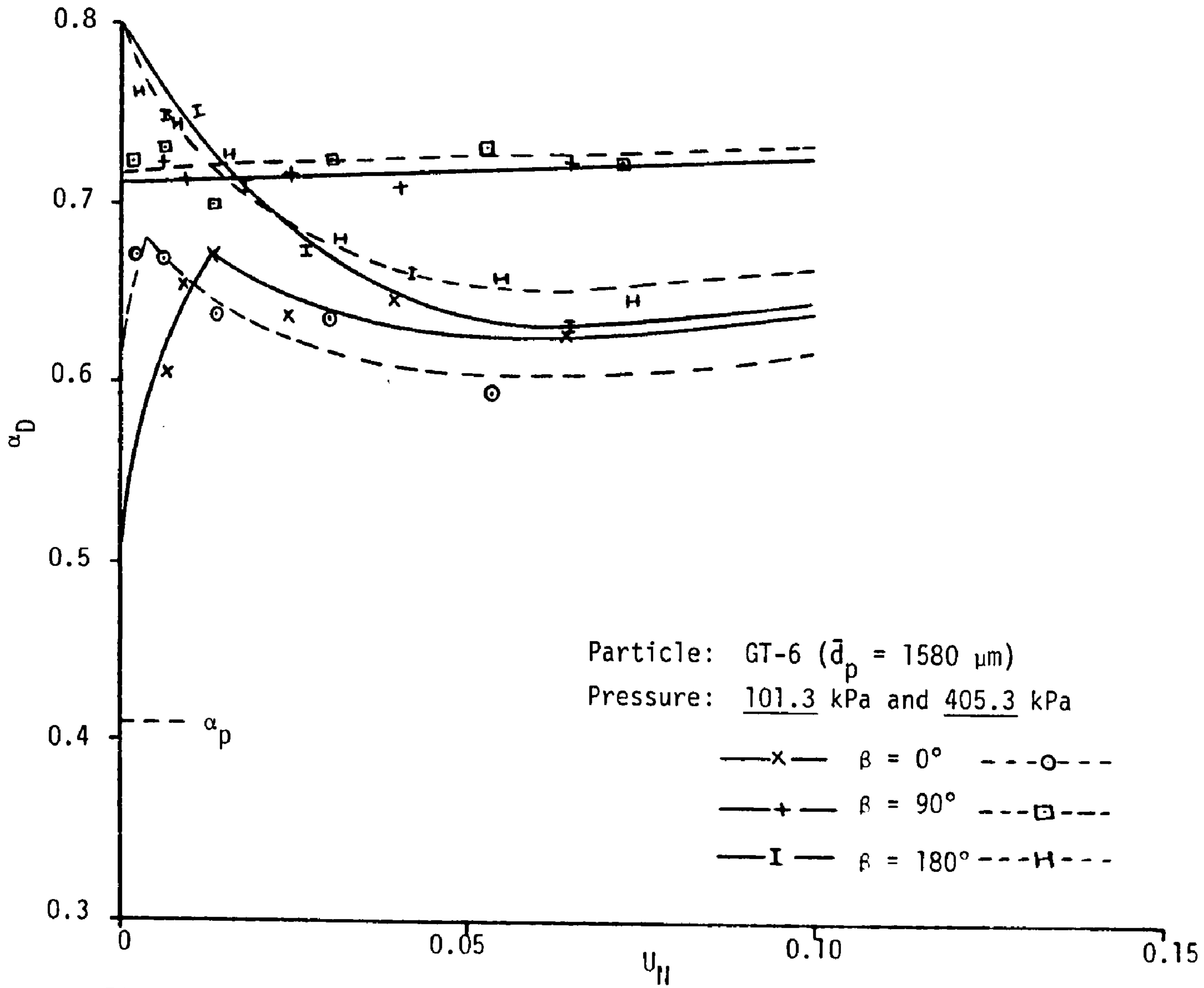

Figure 36 Effect of pressure on dense phase void fraction for large particles

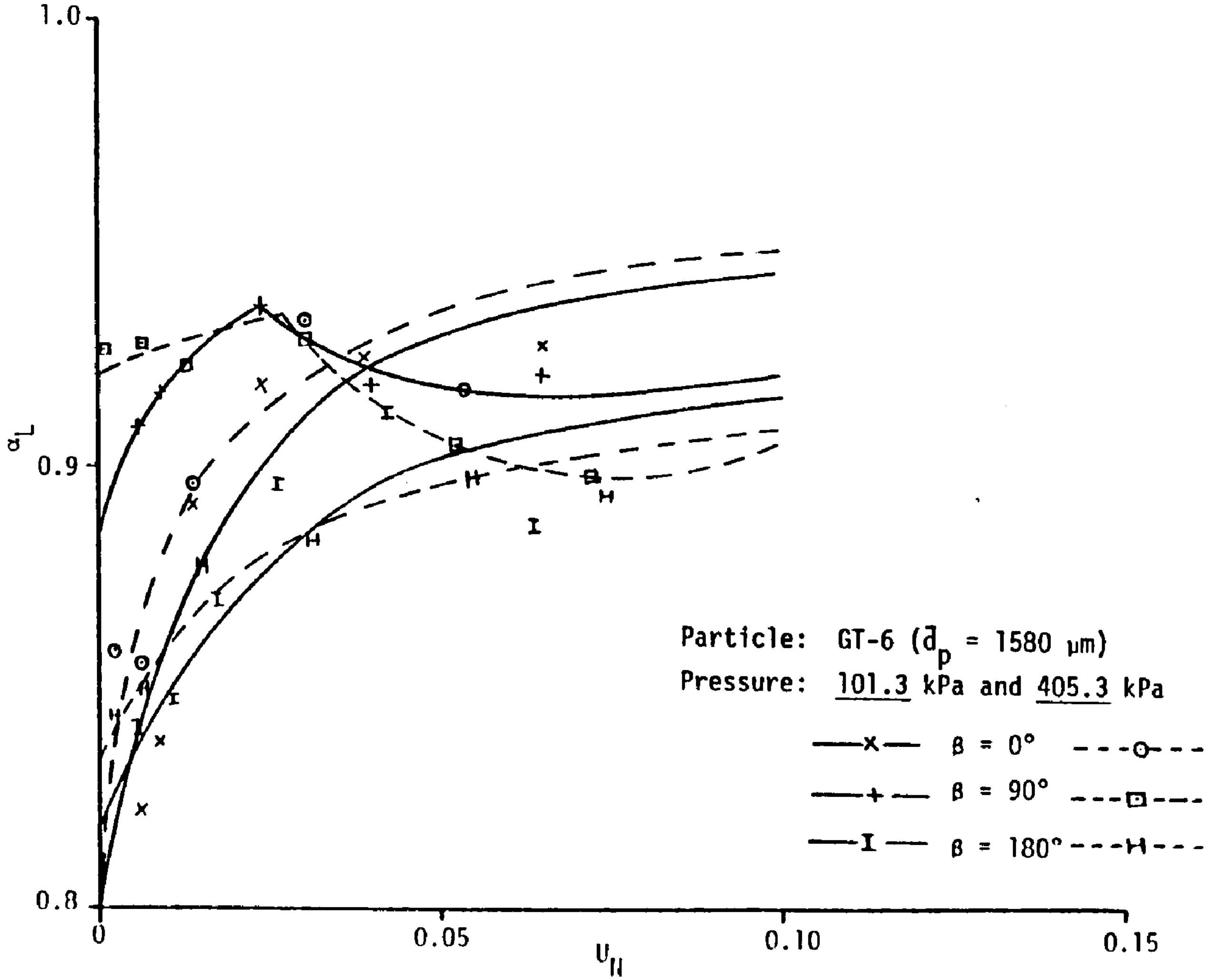

Figure 37 Effect of pressure on lean phase void fraction for large particles

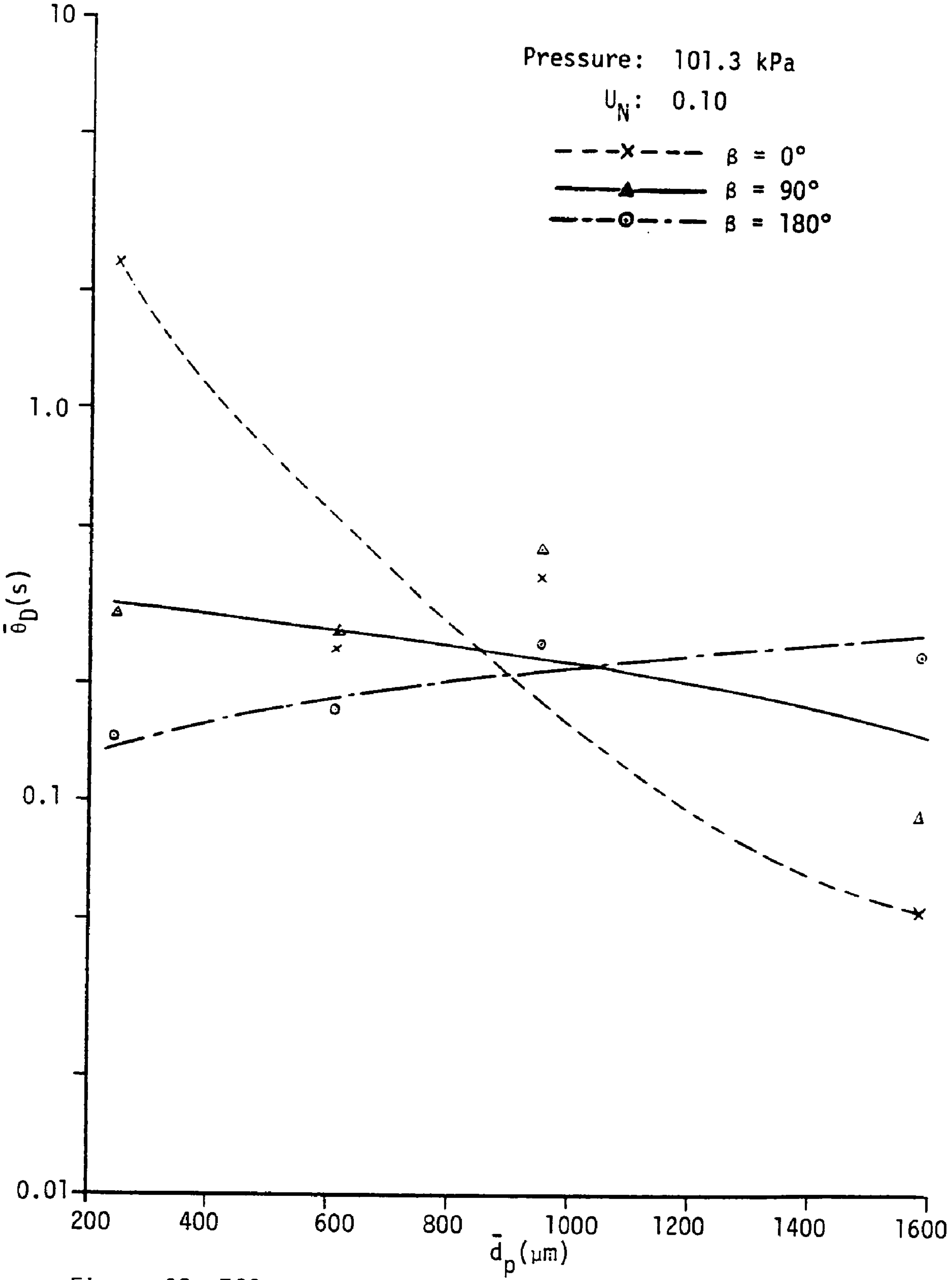

Figure 38 Effect of particle size on dense phase root-square-average residence time

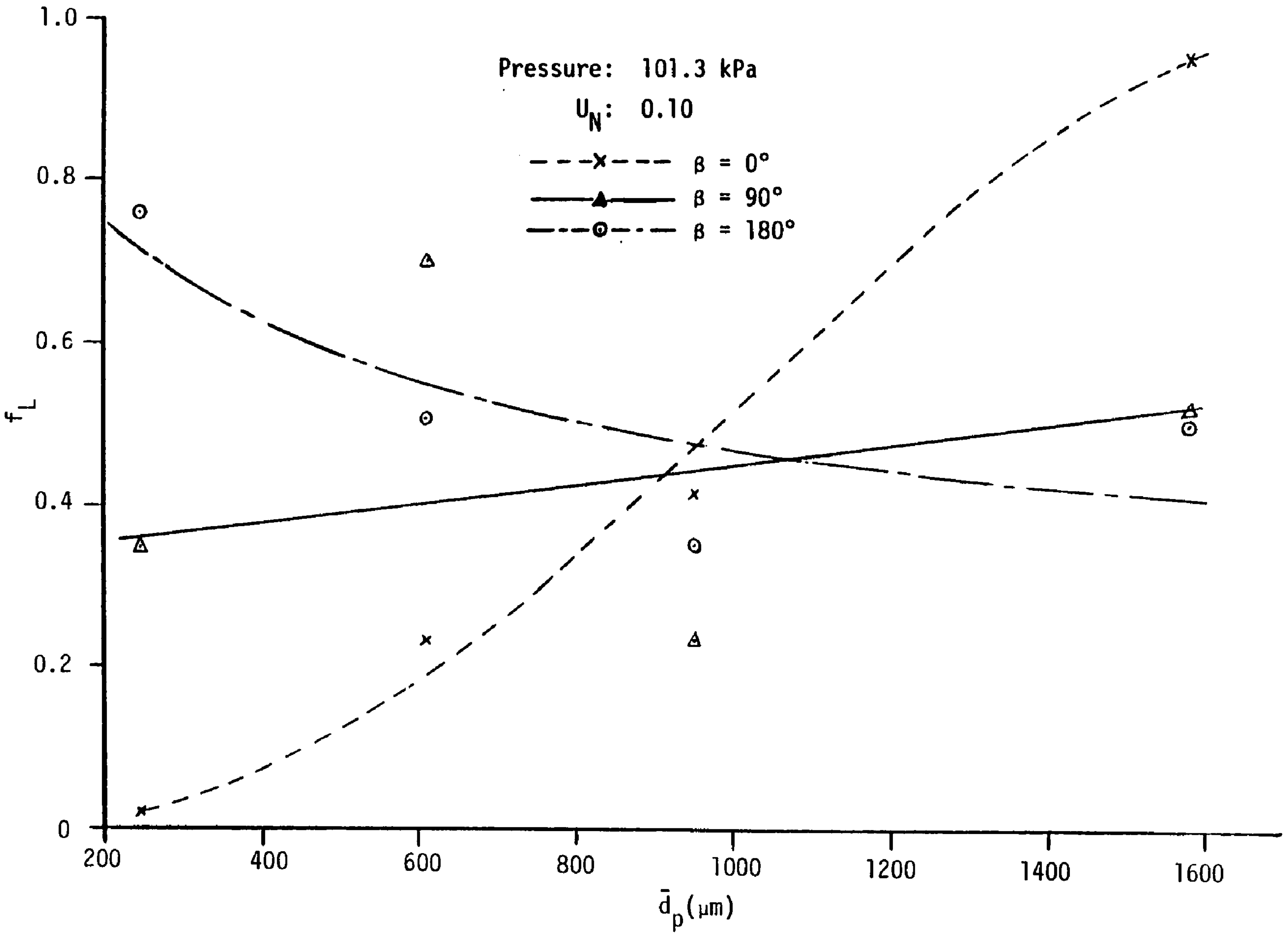

Figure 39 Effect of particle size on lean phase fractional contact time

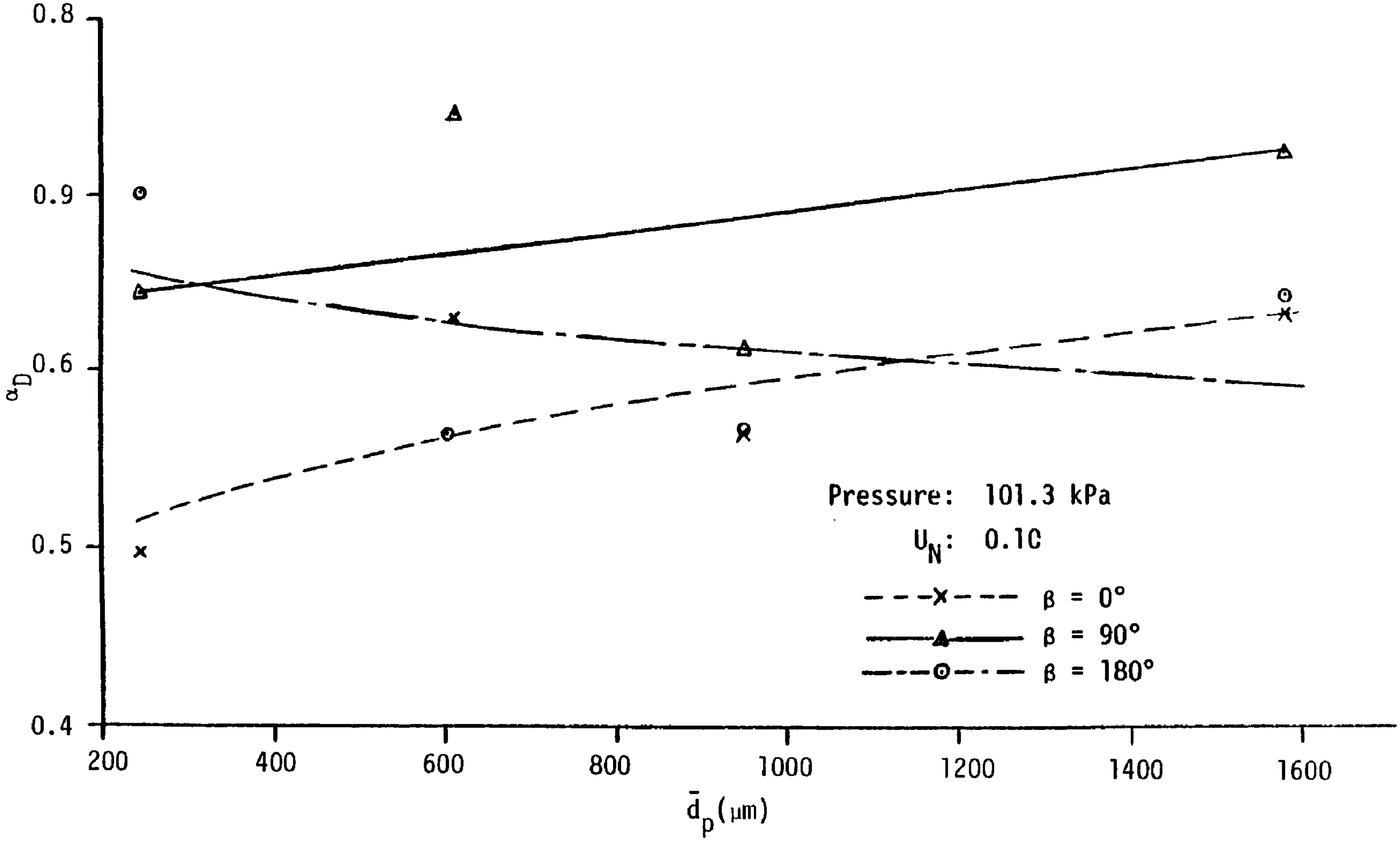

Figure 40 Effect of particle size on dense phase void fraction

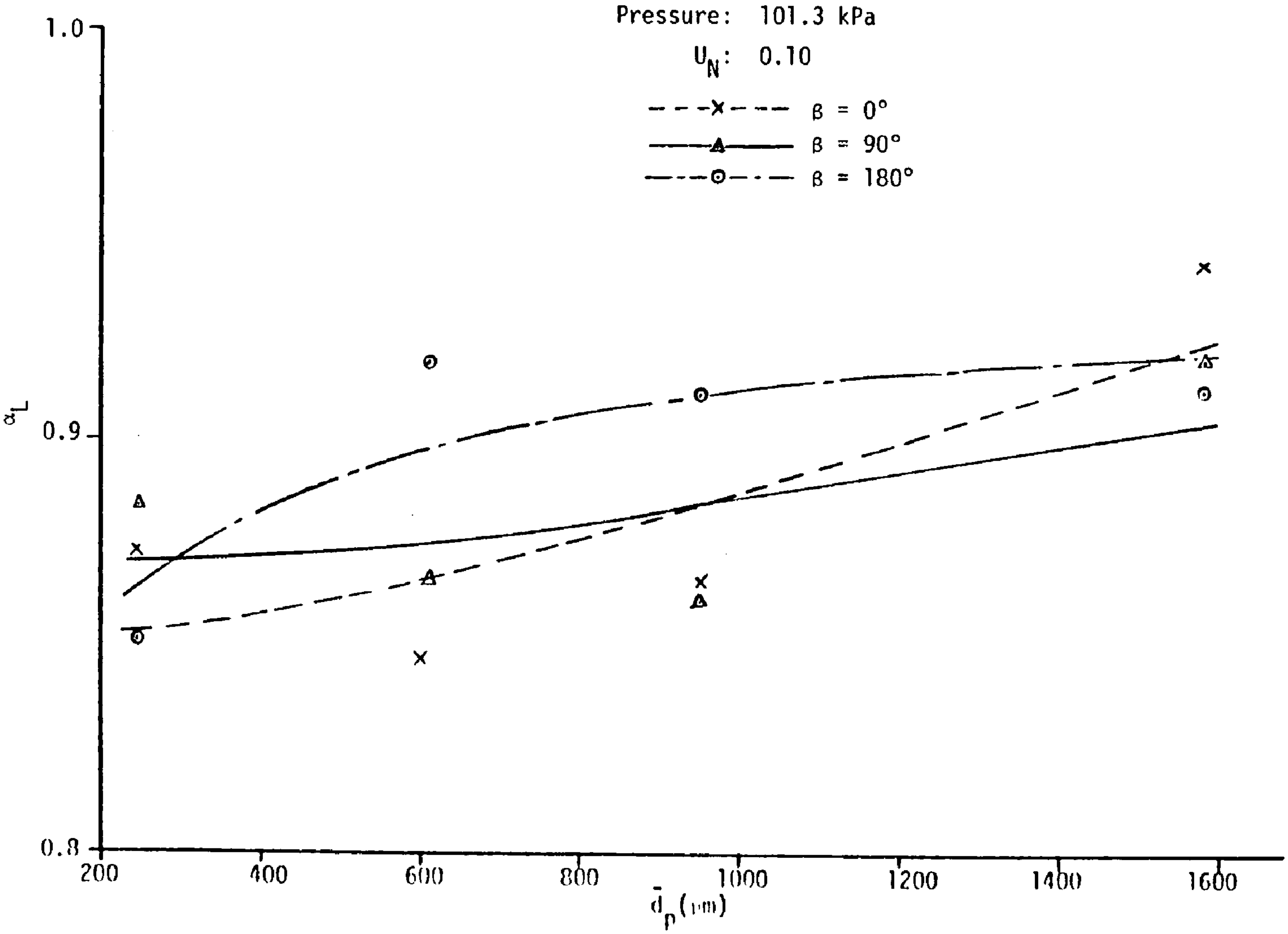

Figure 41 Effect of particle size on lean phase void fraction

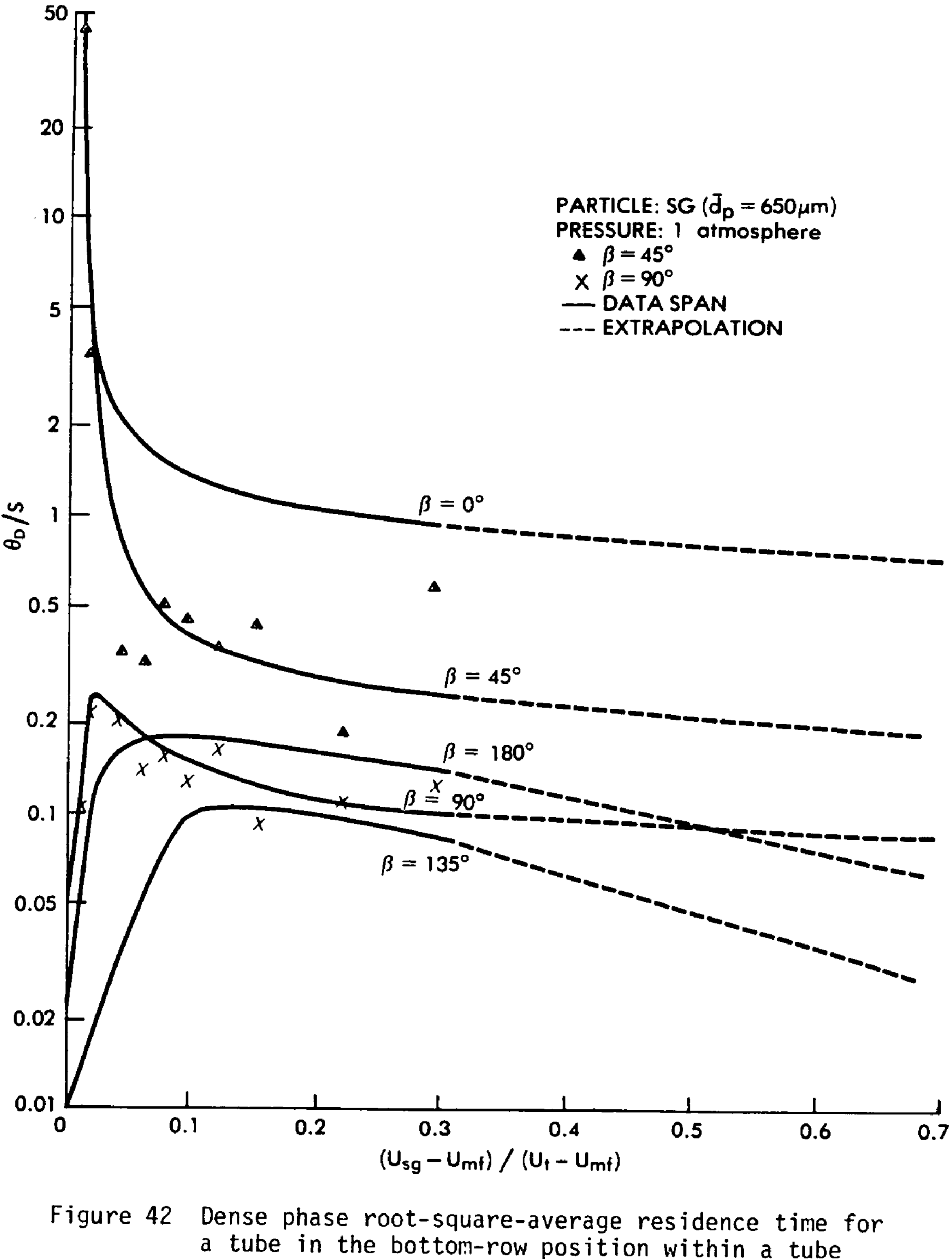

Figure 42 Dense phase root-square-average residence time for a tube in the bottom-row position within a tube bundle

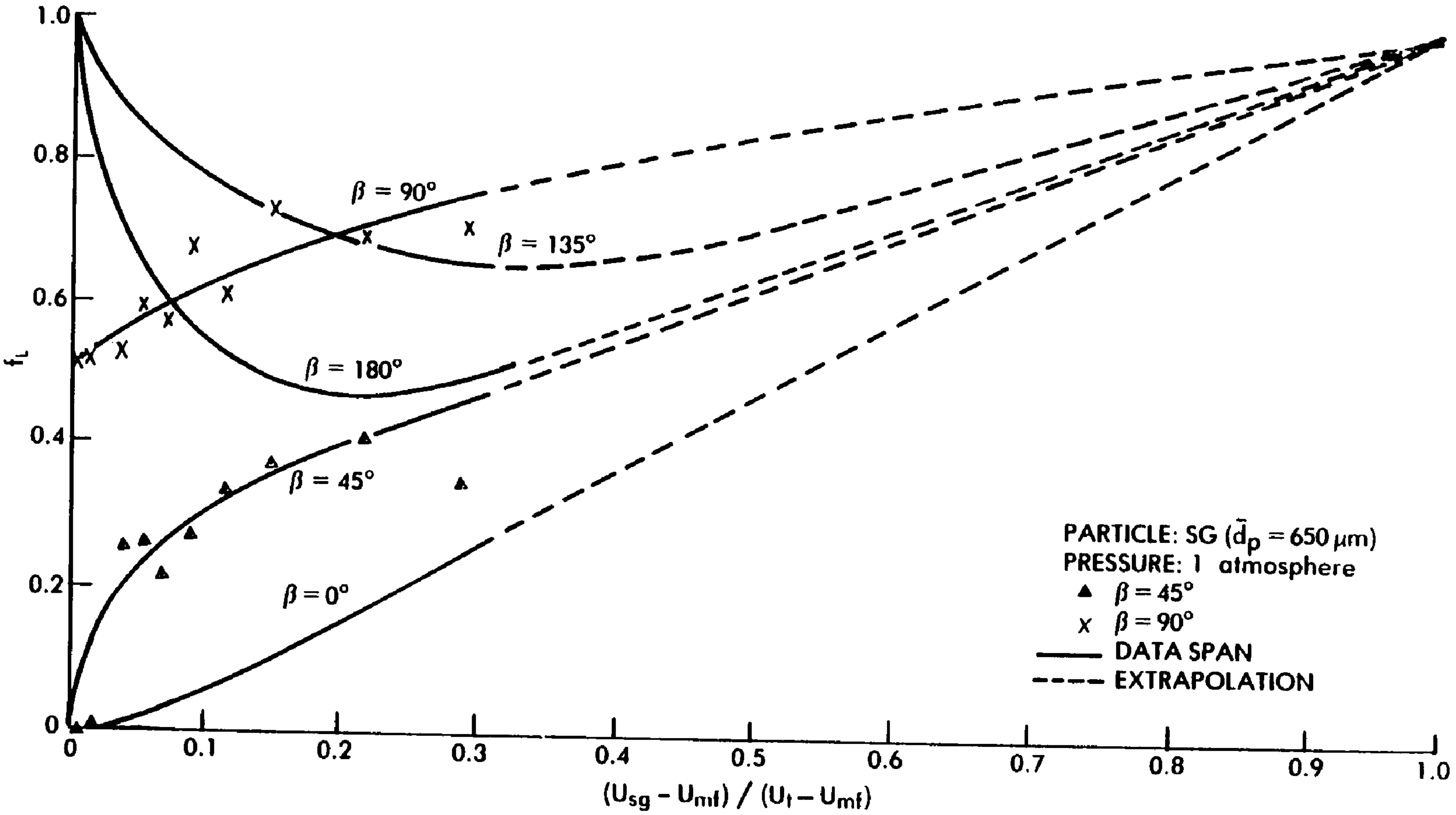

Figure 43 Lean phase fractional contact time for a tube in the bottom-row position within a tube bundle

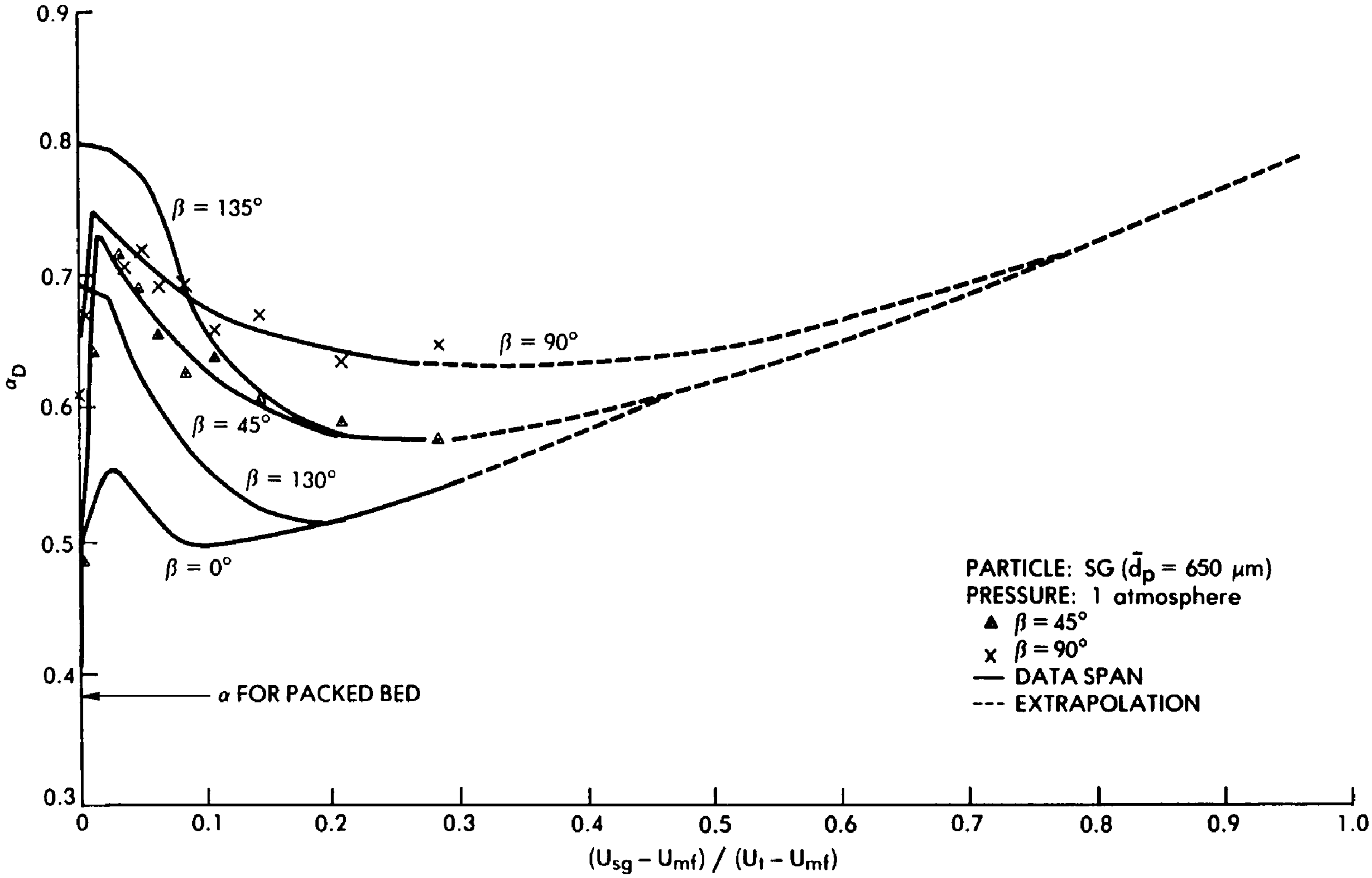

Figure 44 Dense phase void fraction for a tube in the bottom-row position within a tube bundle

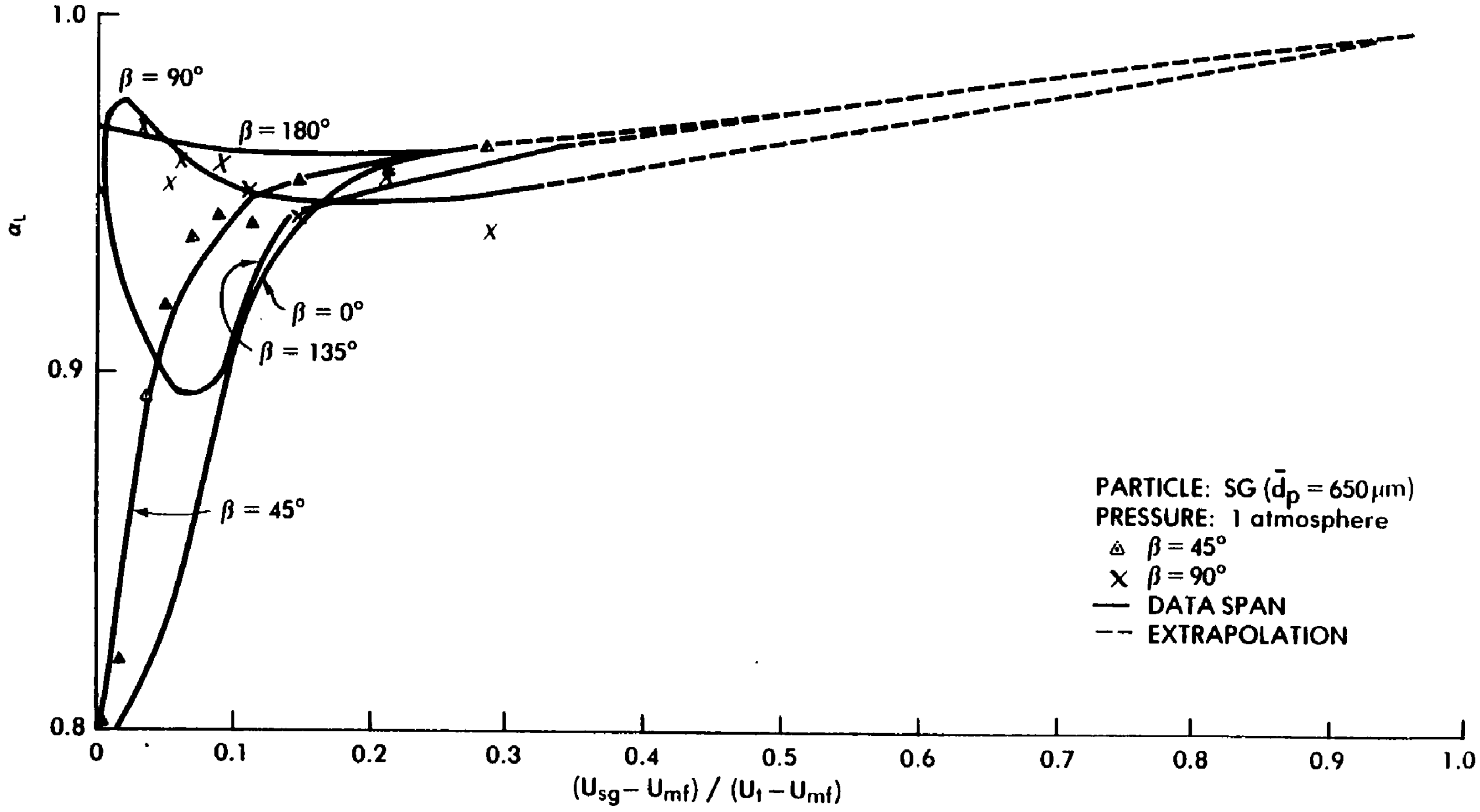

Figure 45 Lean phase void fraction for a tube in the bottom-row position within a tube bundle

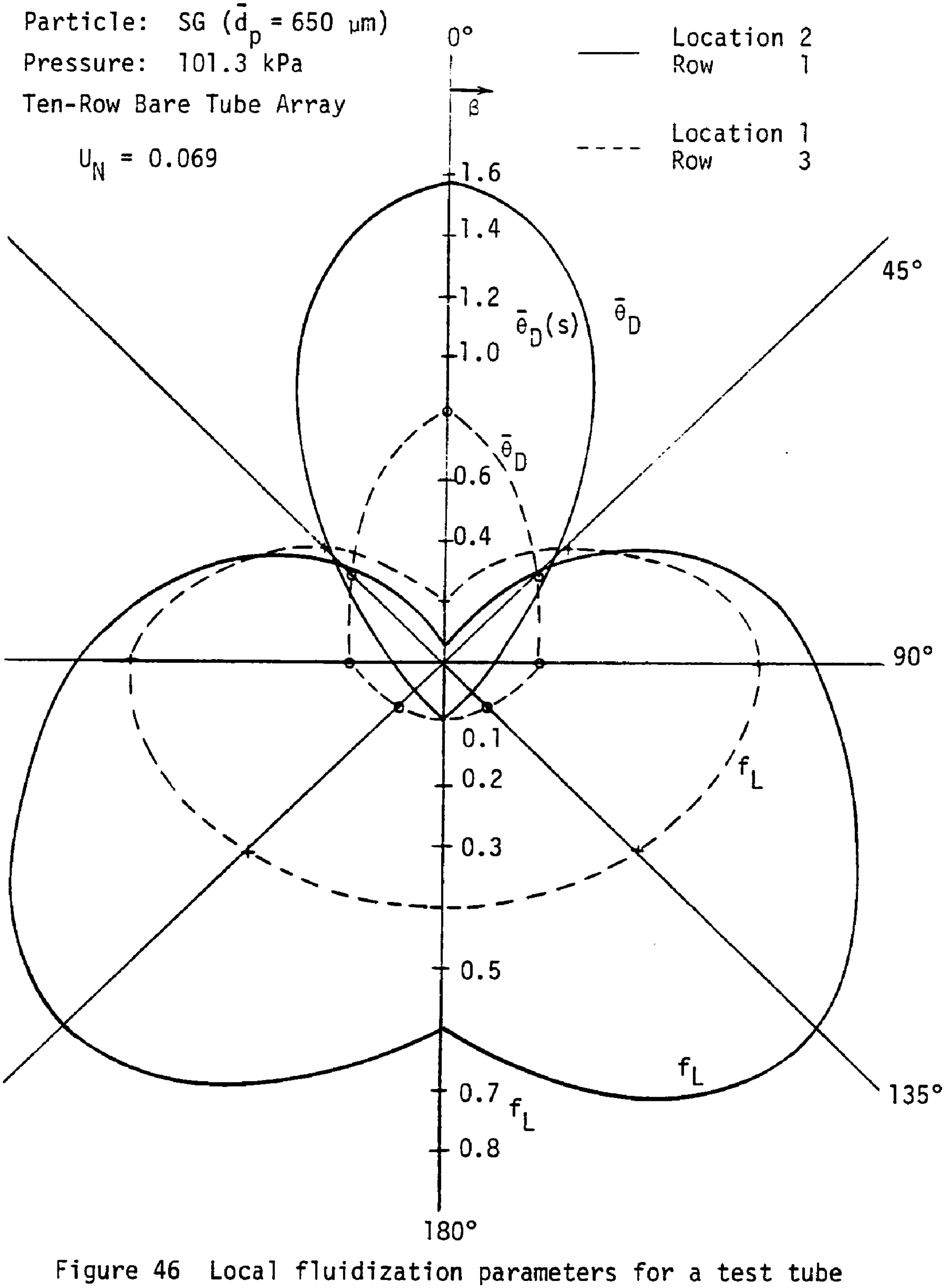

Figure 46 Local fluidization parameters for a test tube at two different locations within a tube bundle

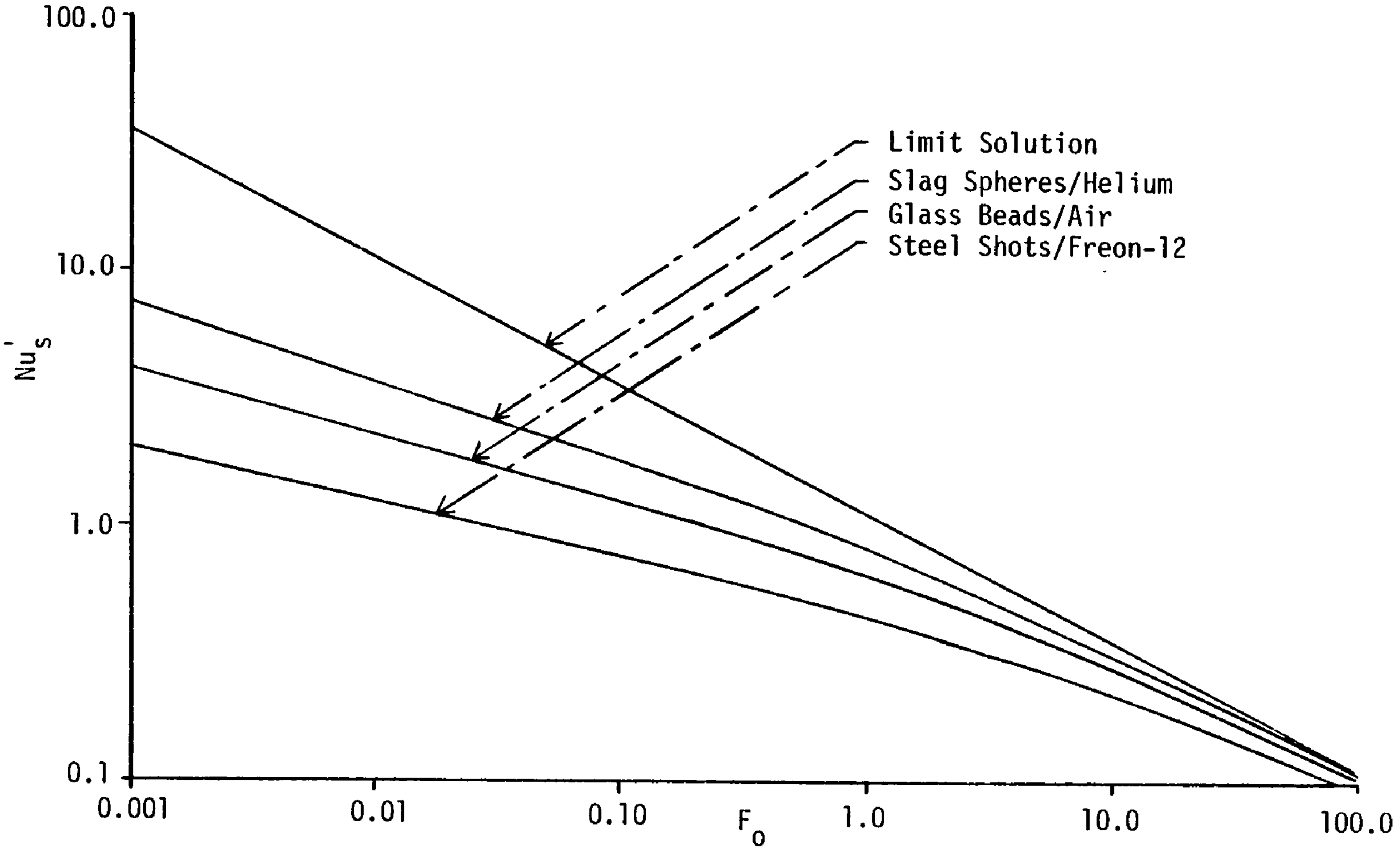

Figure 47 Variation of transient conduction solution with Fourier modulus and conductivity ratio

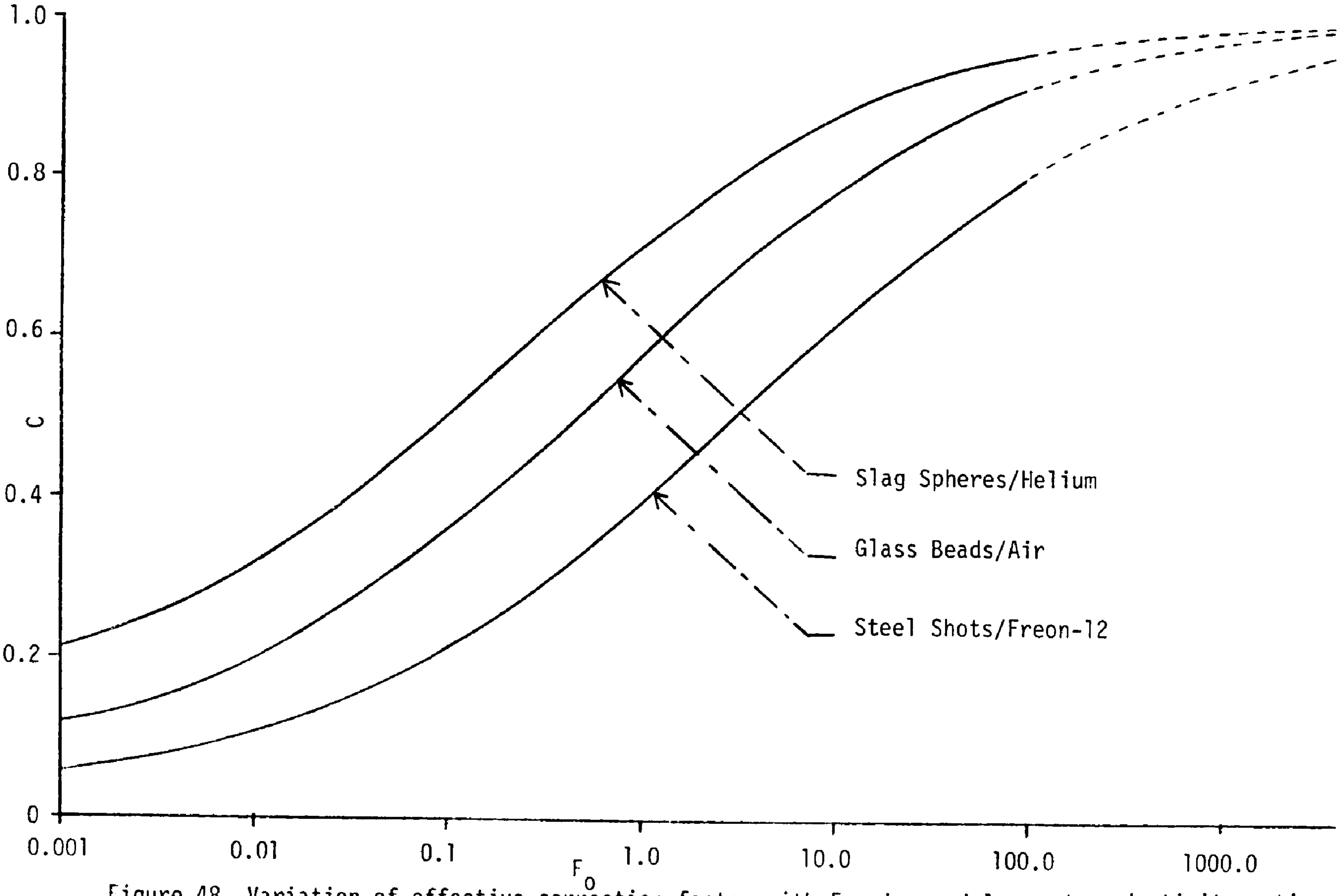

Figure 48 Variation of effective correction factor with Fourier modulus and conductivity ratio

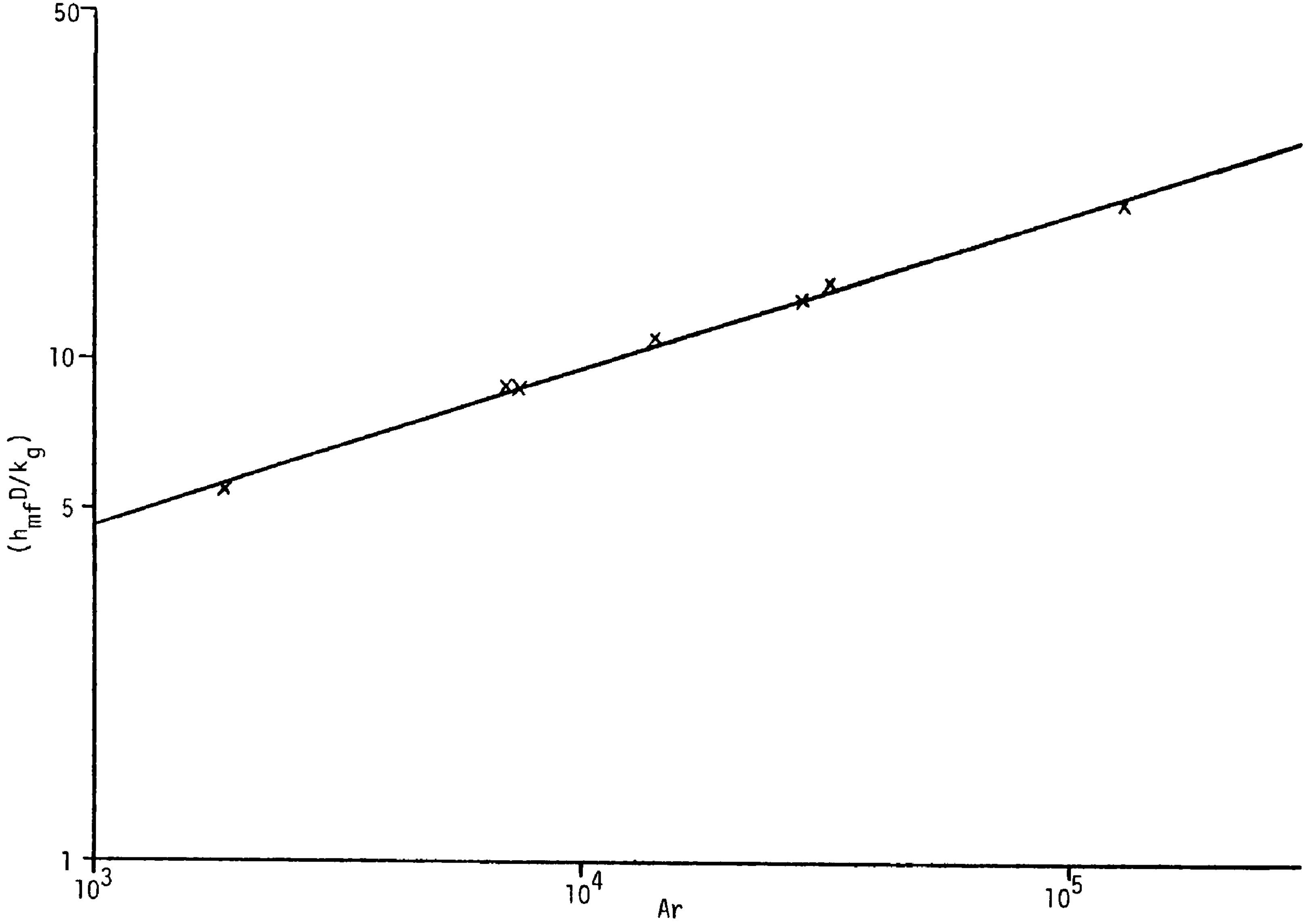

Figure 49 Correlation for heat transfer coefficient at minimum fluidization condition and in the absence of surface renewal

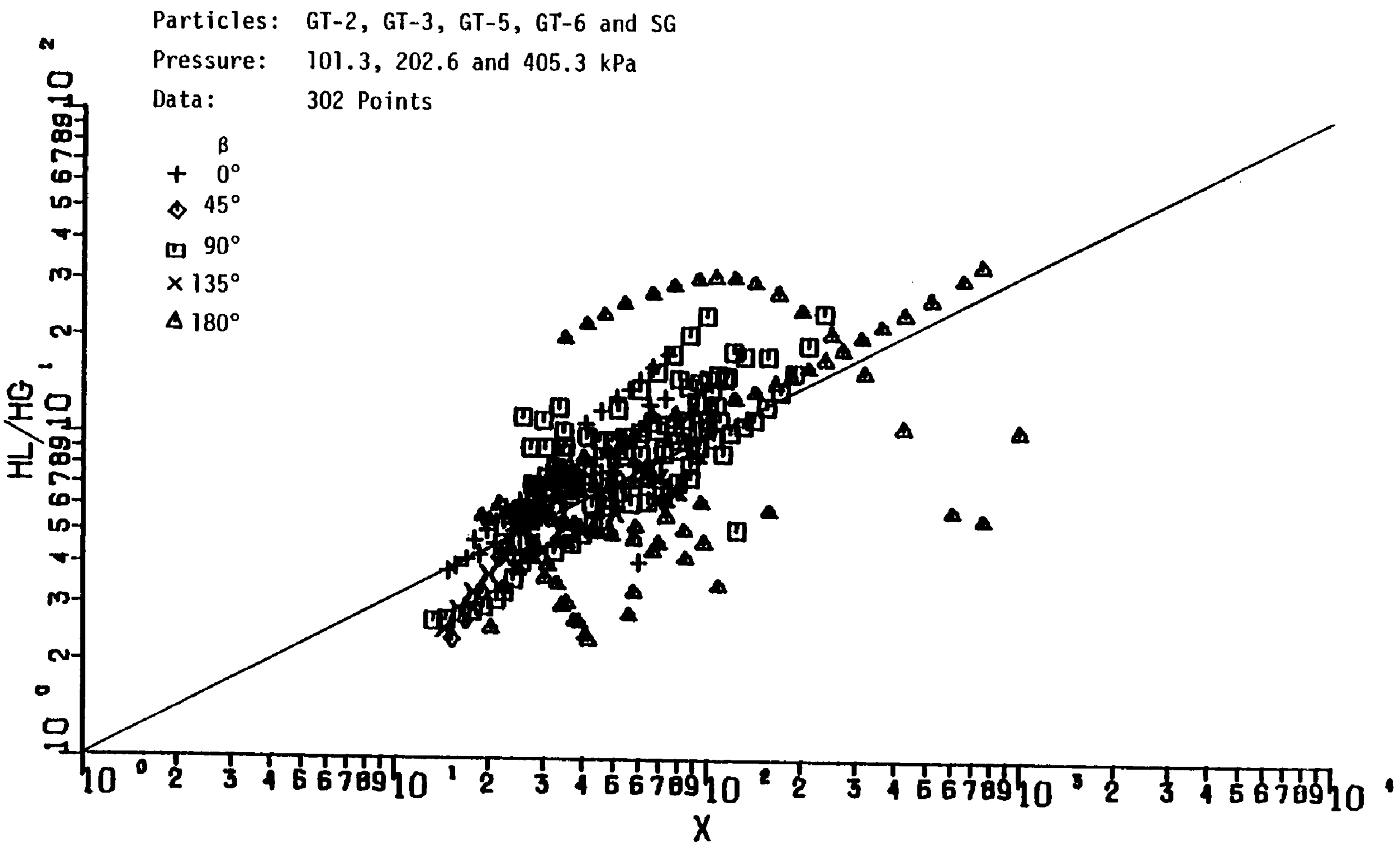

Figure 50 Correlation for effective heat transfer coefficient in the lean phase

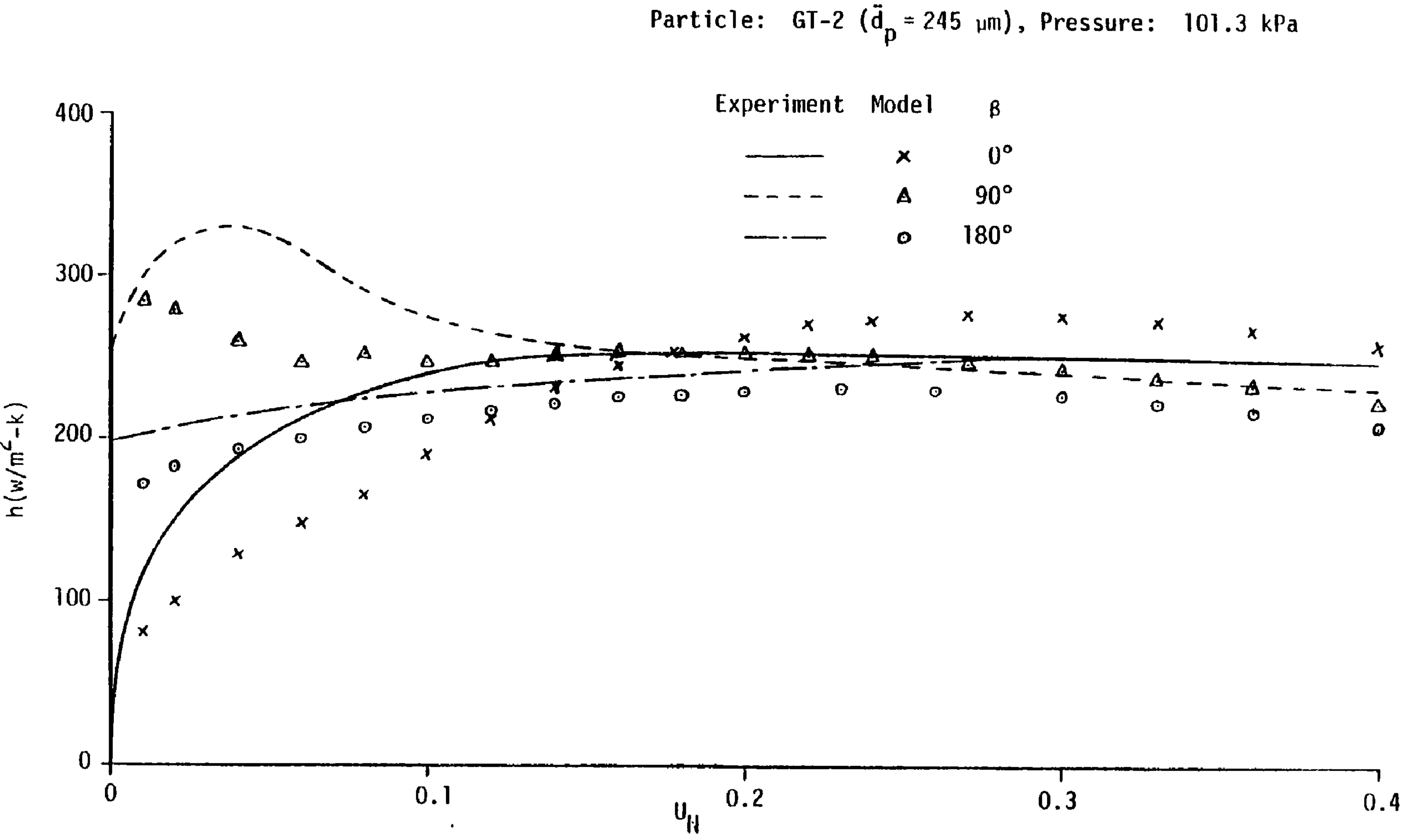

Figure 51 Comparison of model predictions with experimental measurements of local heat transfer coefficient

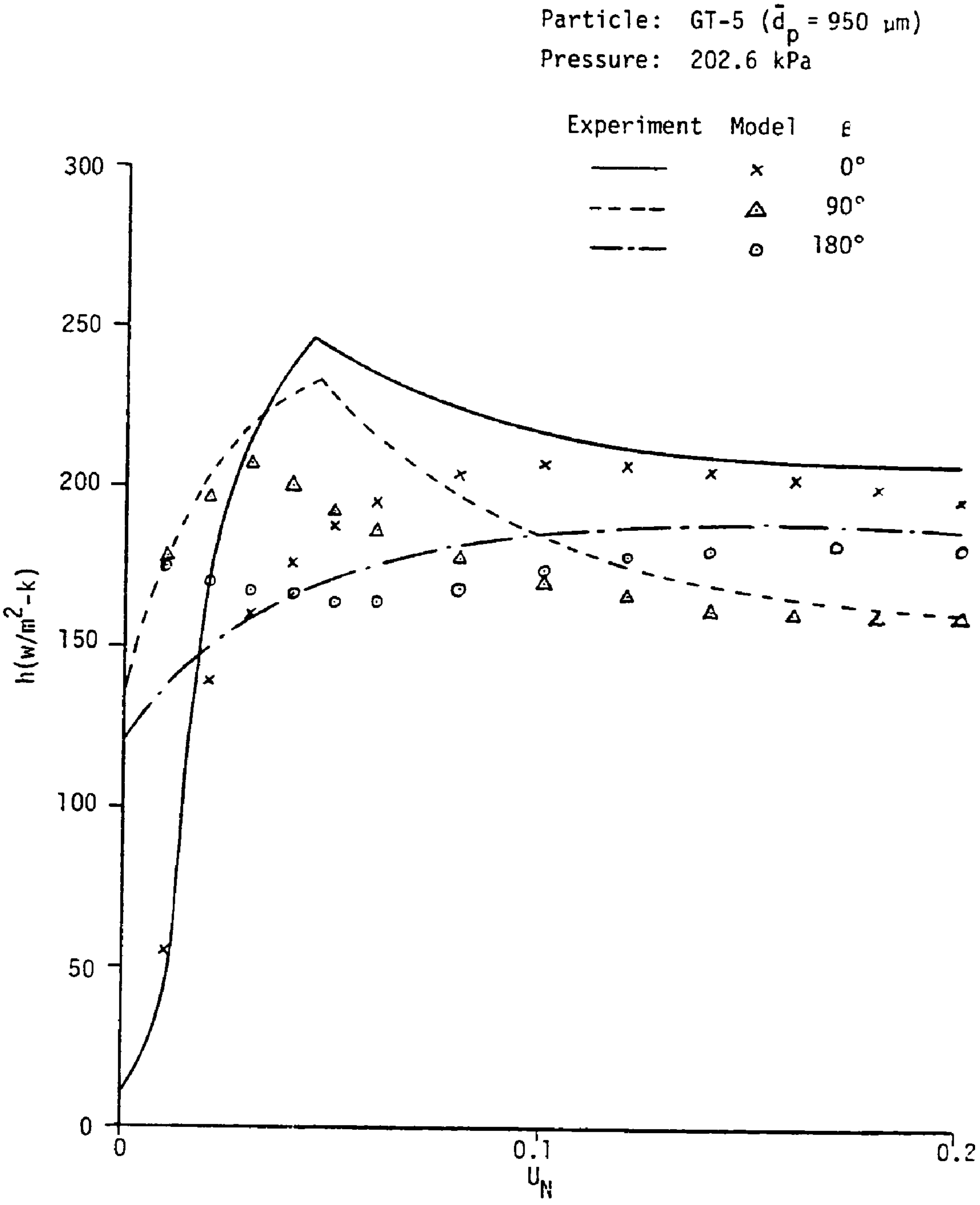

Figure 52 Comparison of model predictions with experimental measurements of local heat transfer coefficient

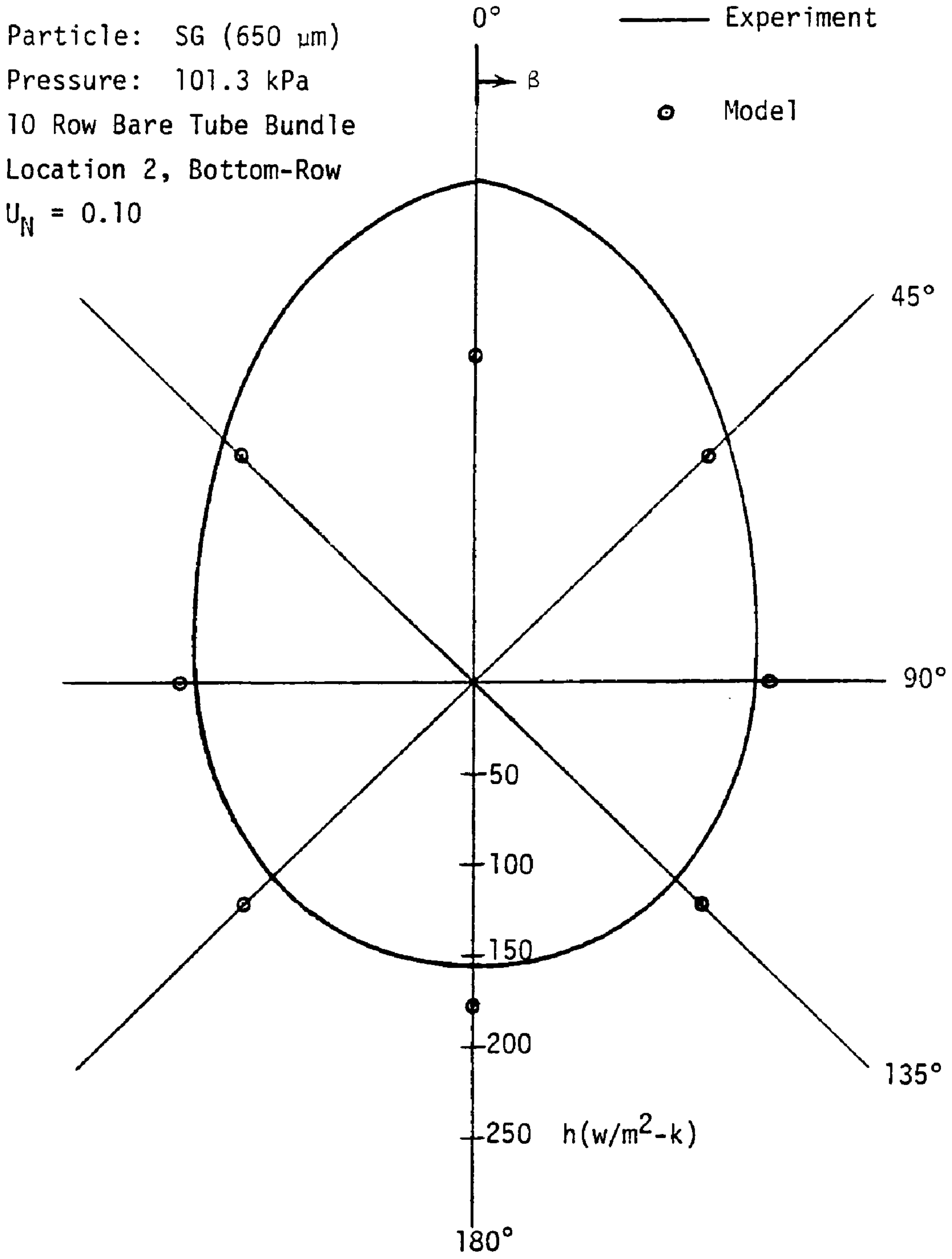

Figure 53 Comparison of model predictions with experimental measurements of local heat transfer coefficient

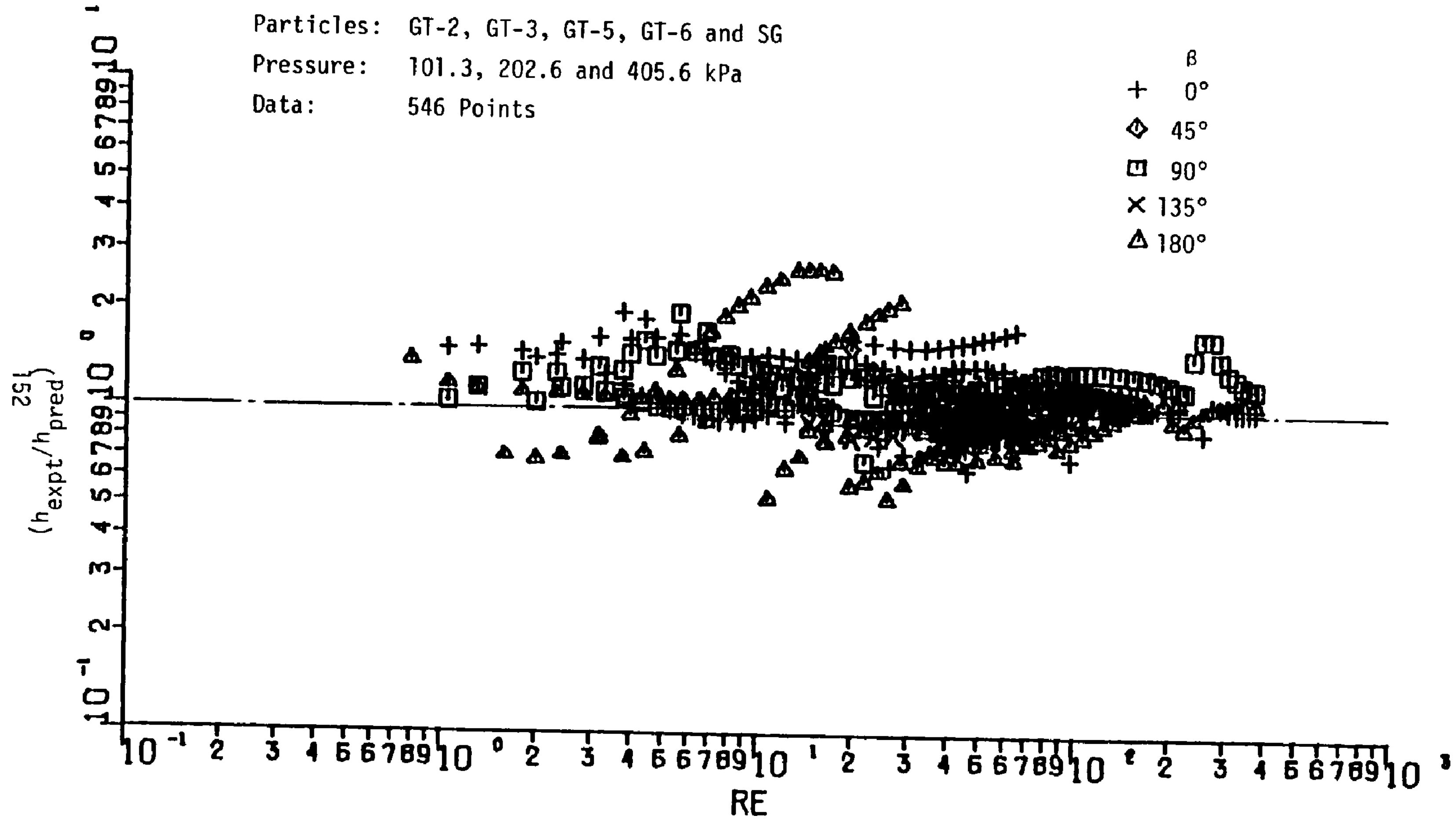

Figure 54 Comparison of experimental data for local heat transfer coefficient with model predictions

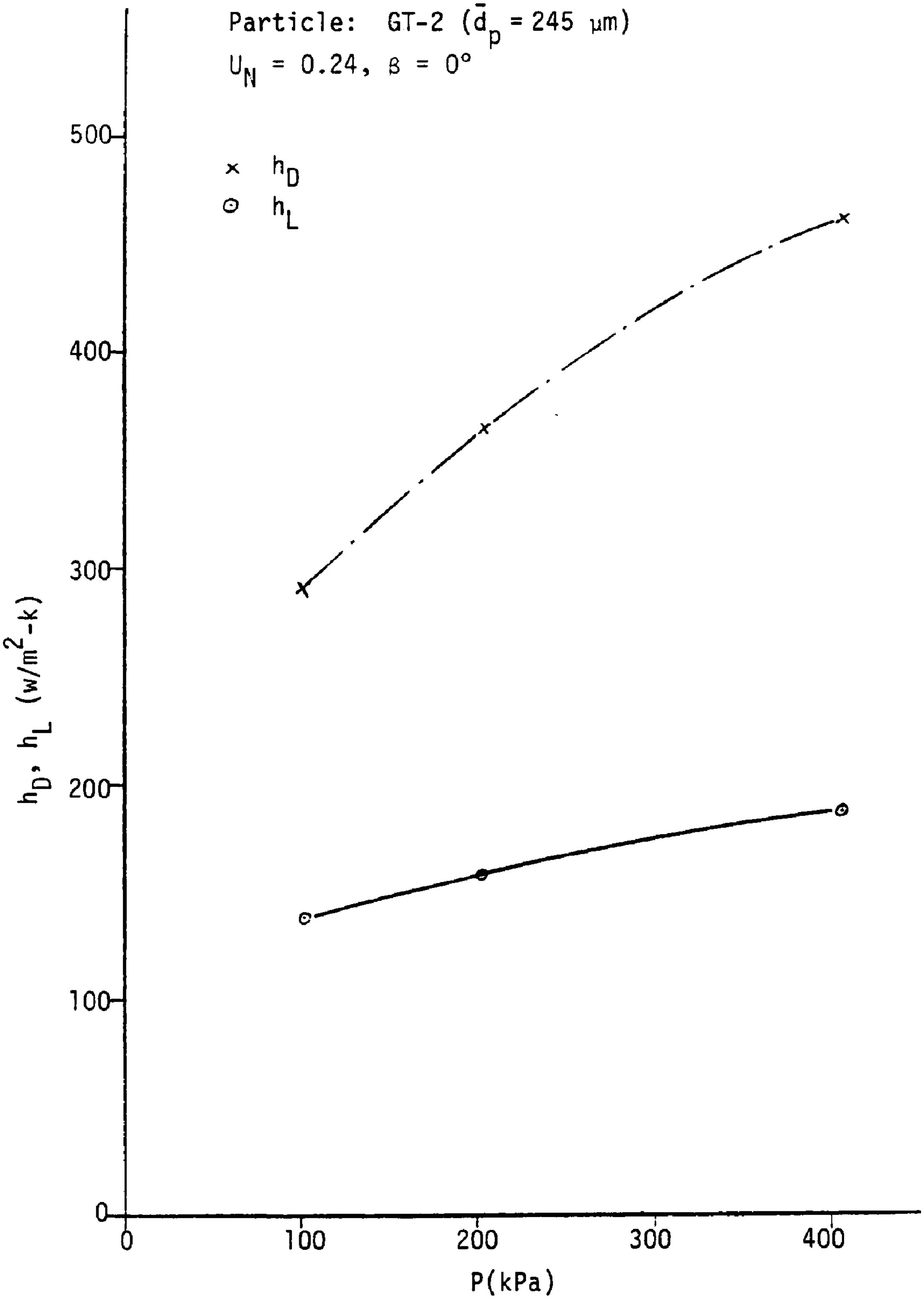

Figure 55 Influence of system pressure on effective heat transfer coefficients in the dense and in the lean phases

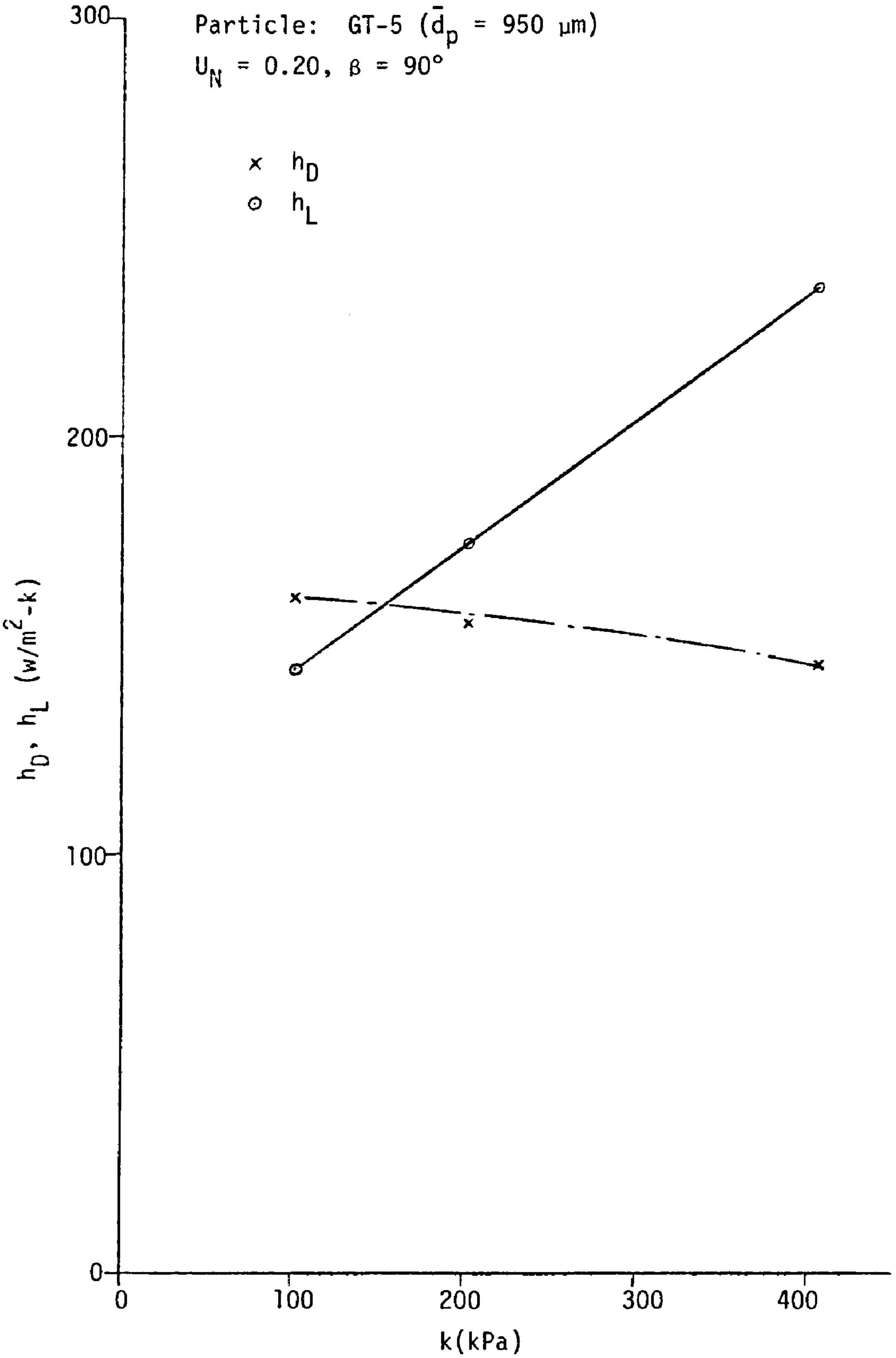

Figure 56 Influence of system pressure on effective heat transfer coefficients in the dense and in the lean phases

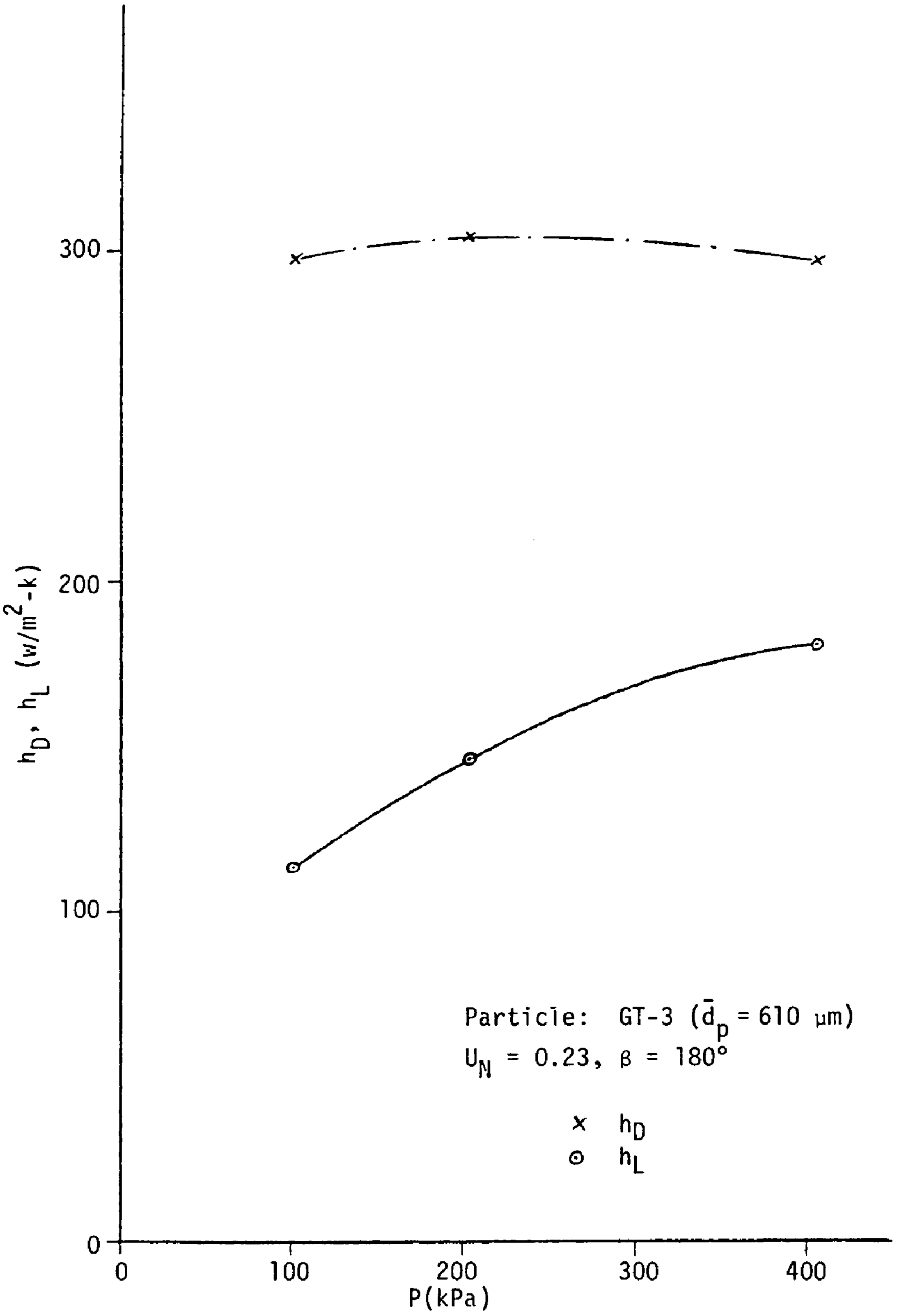

Figure 57 Influence of system pressure on effective heat transfer coefficients in the dense and in the lean phases

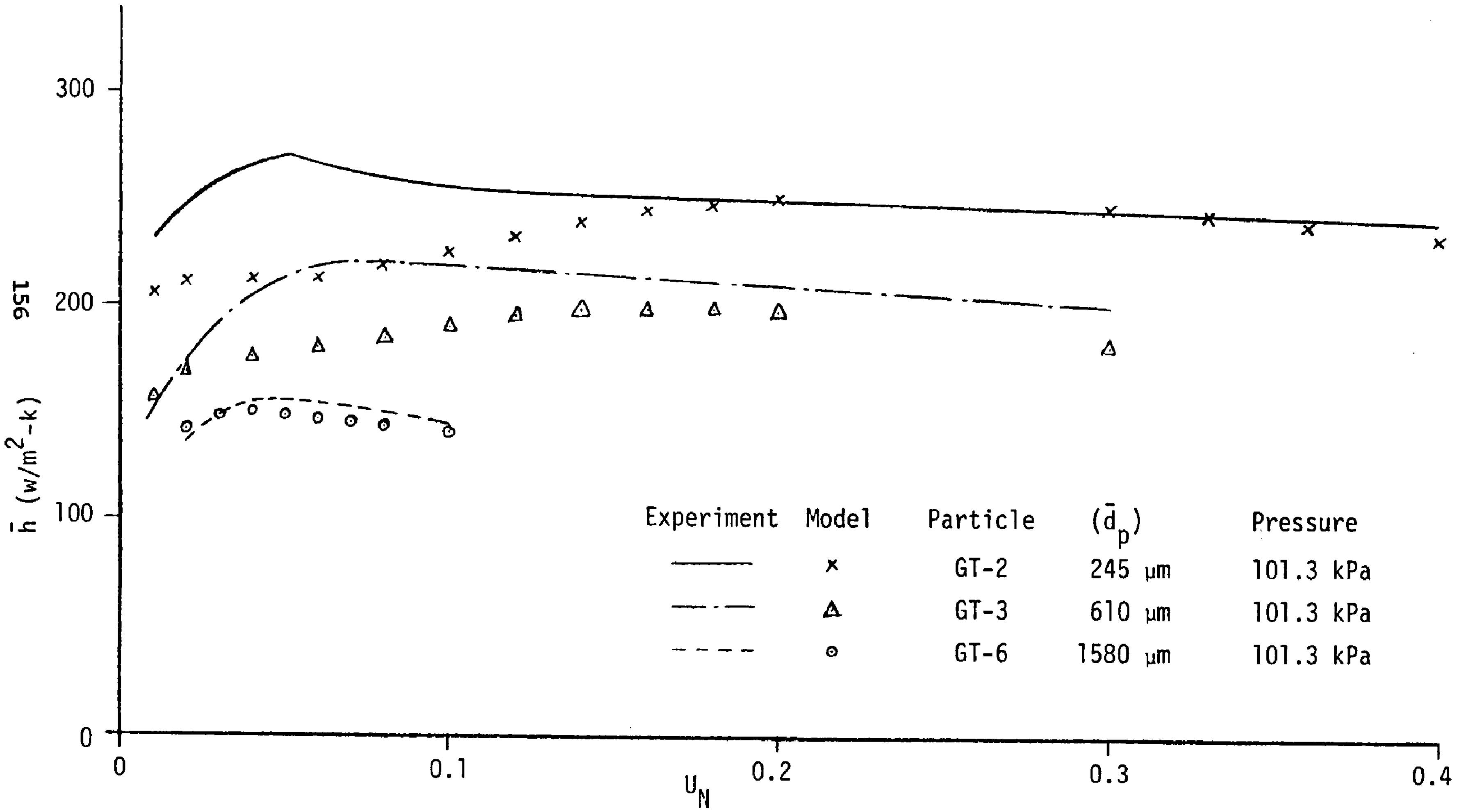

Figure 58 Comparison of model predictions with experimentally-determined values of average heat transfer coefficient

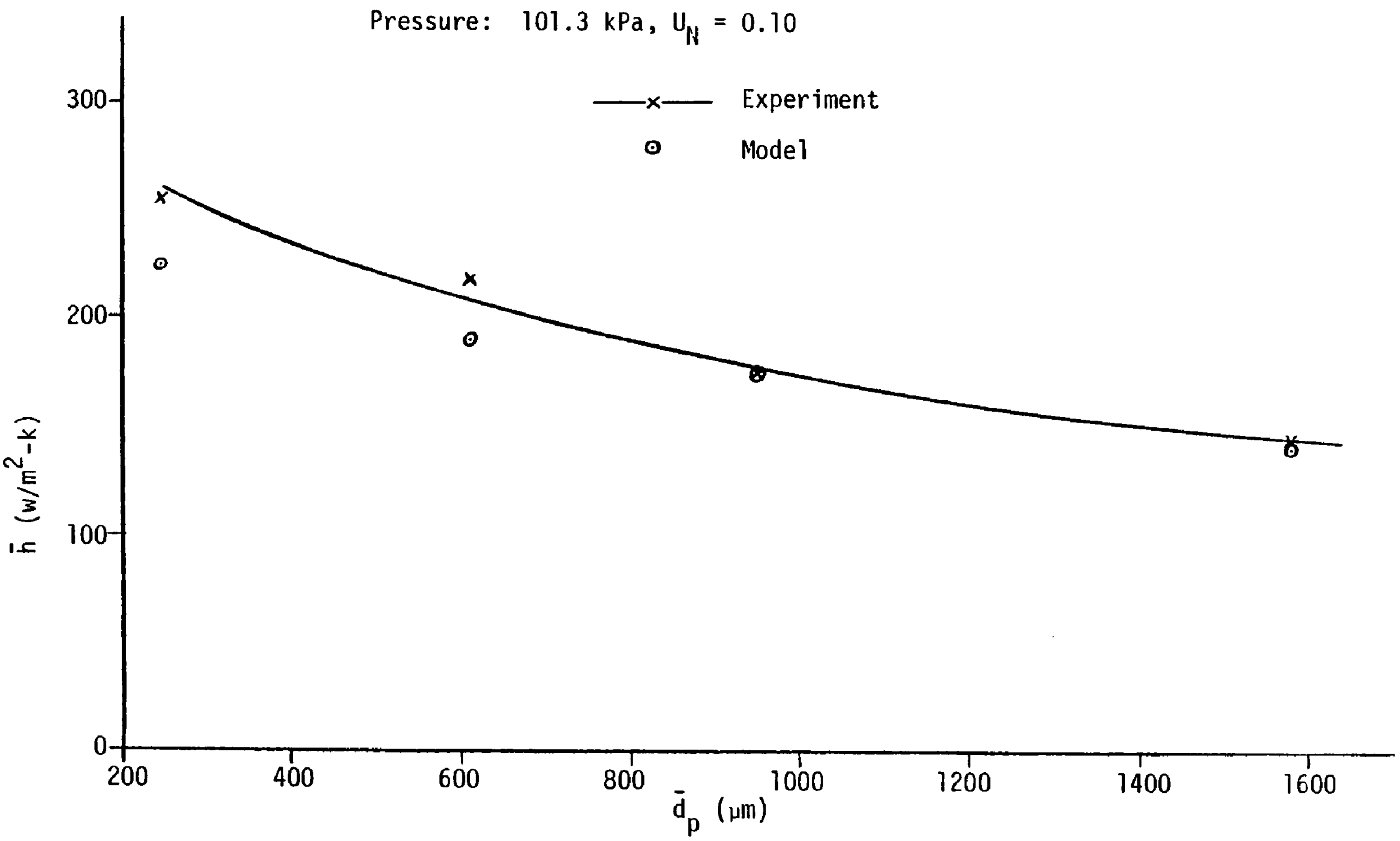

Figure 59 Comparison of model predictions with experimentally-determined values of average heat transfer coefficient

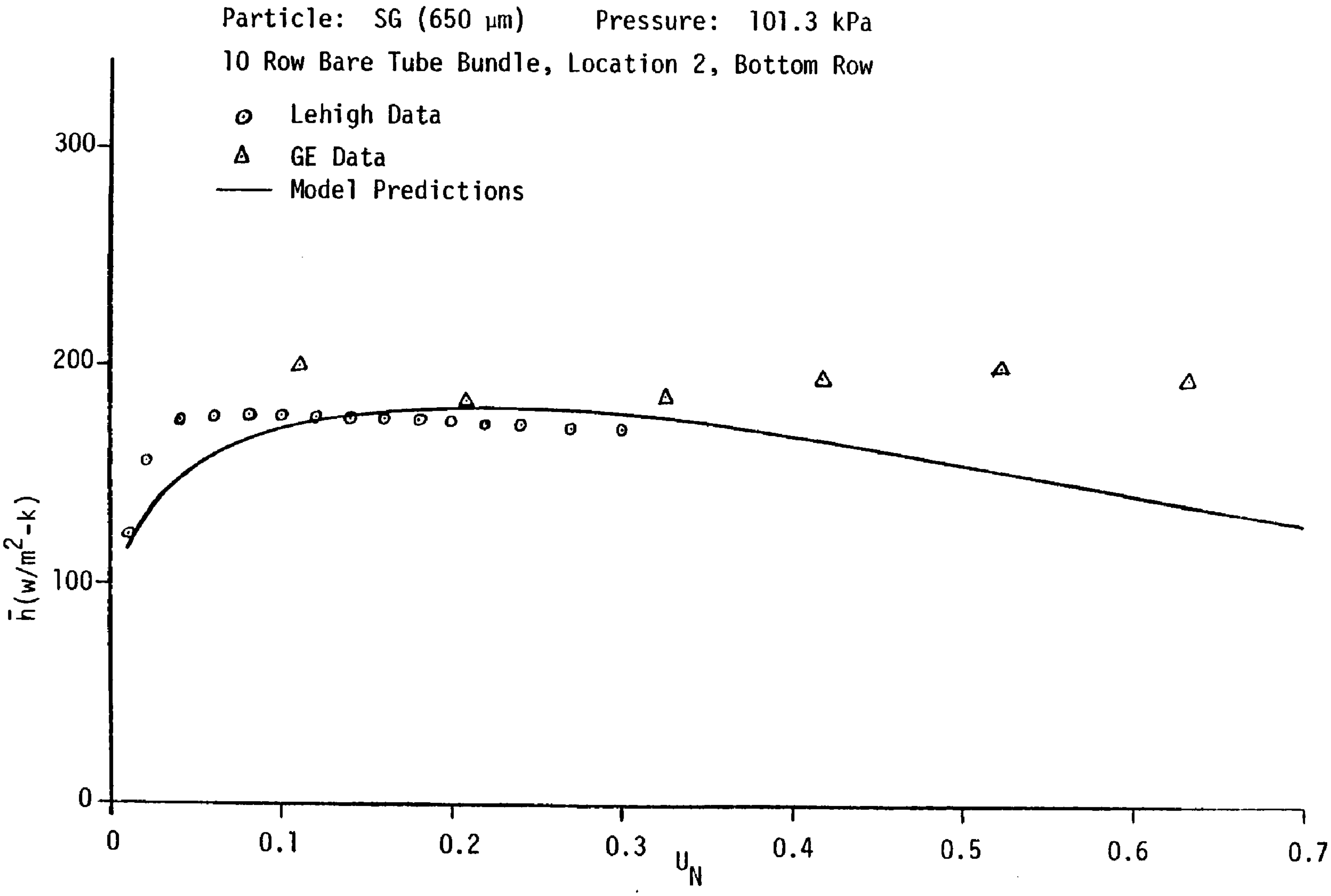

Figure 60 Comparison of model predictions with experimentally-determined values of average heat transfer coefficient

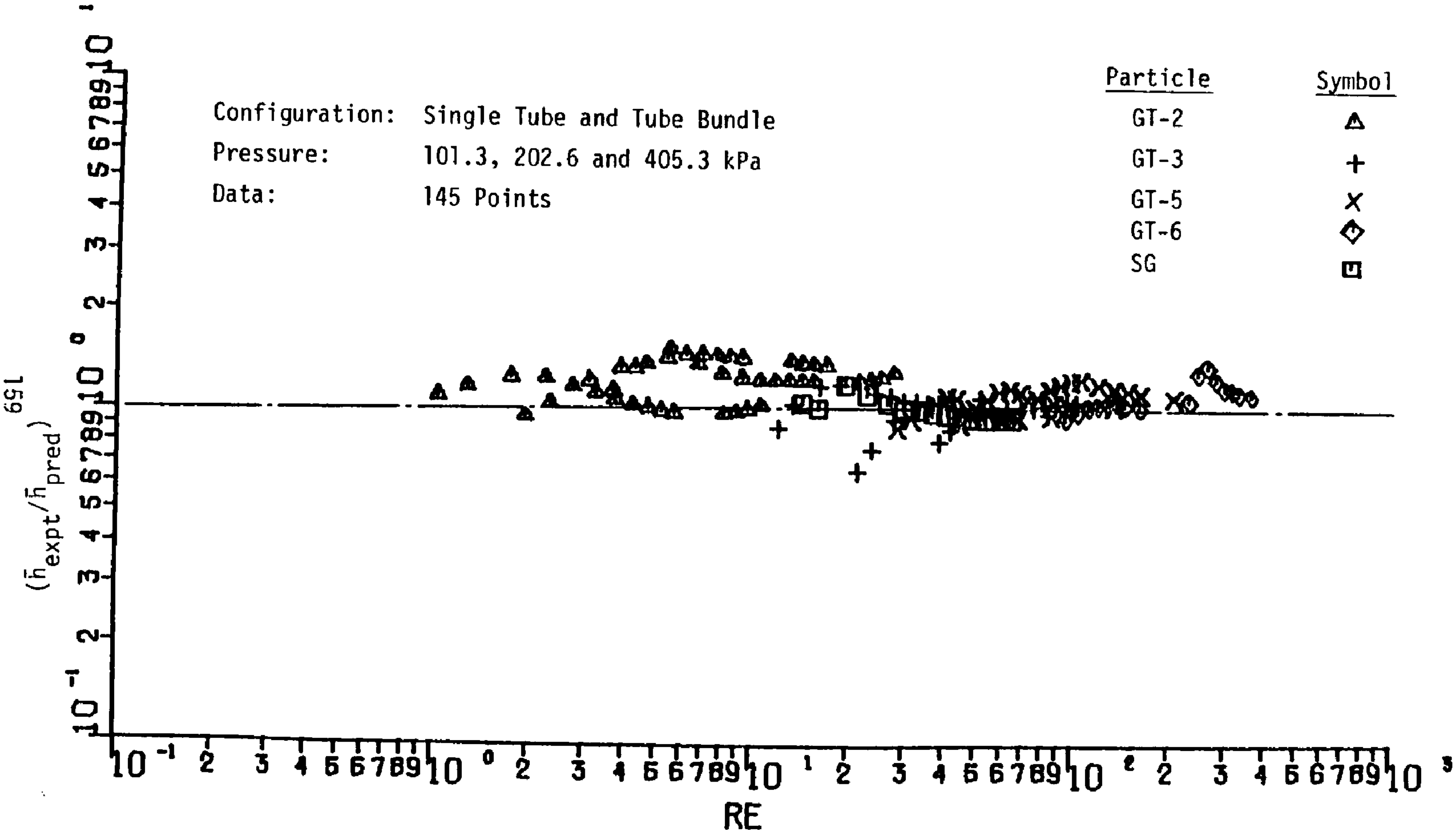

Figure 61 Comparison of experimental data for average heat transfer coefficient with model predictions

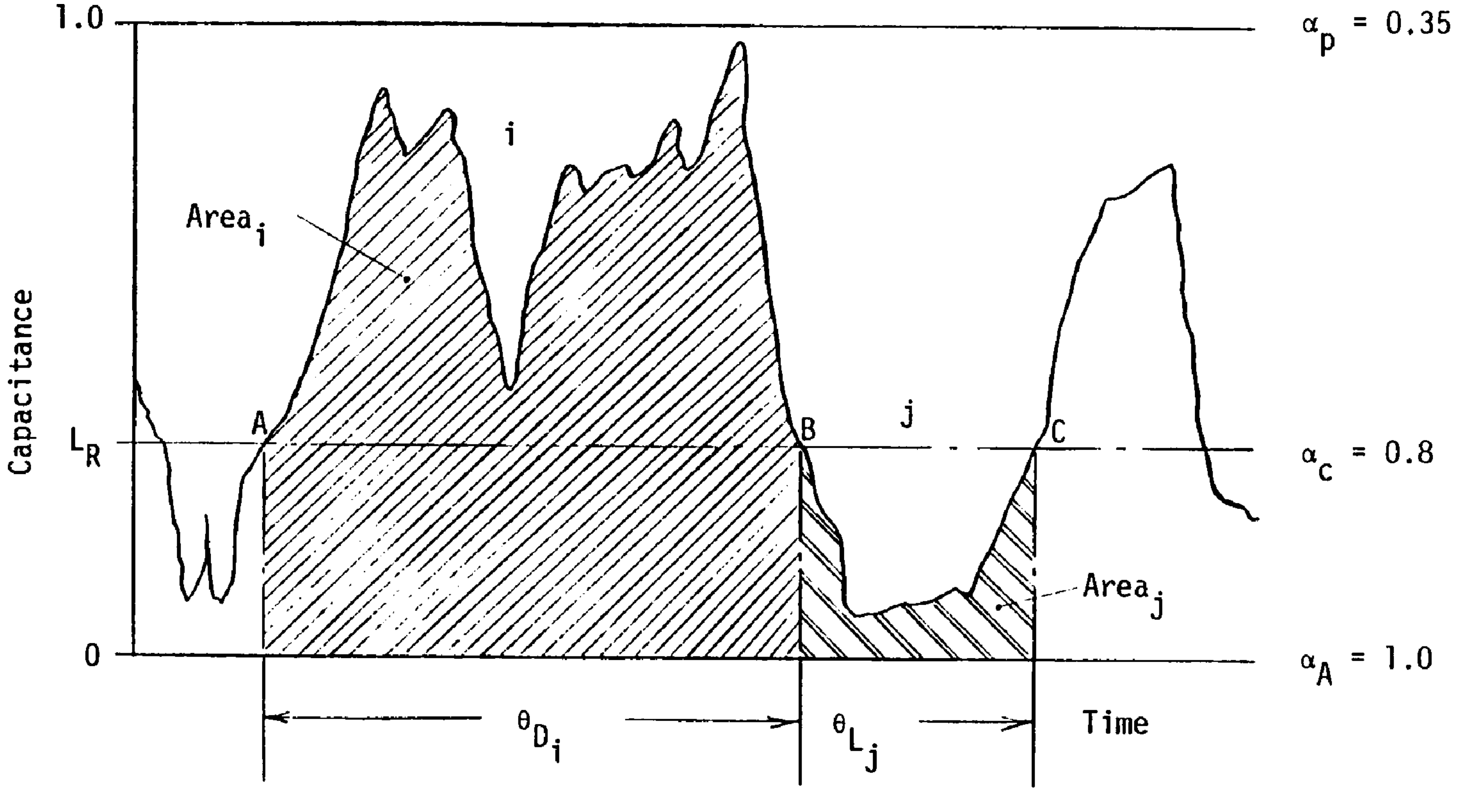

Figure 62 Capacitance signal analysis

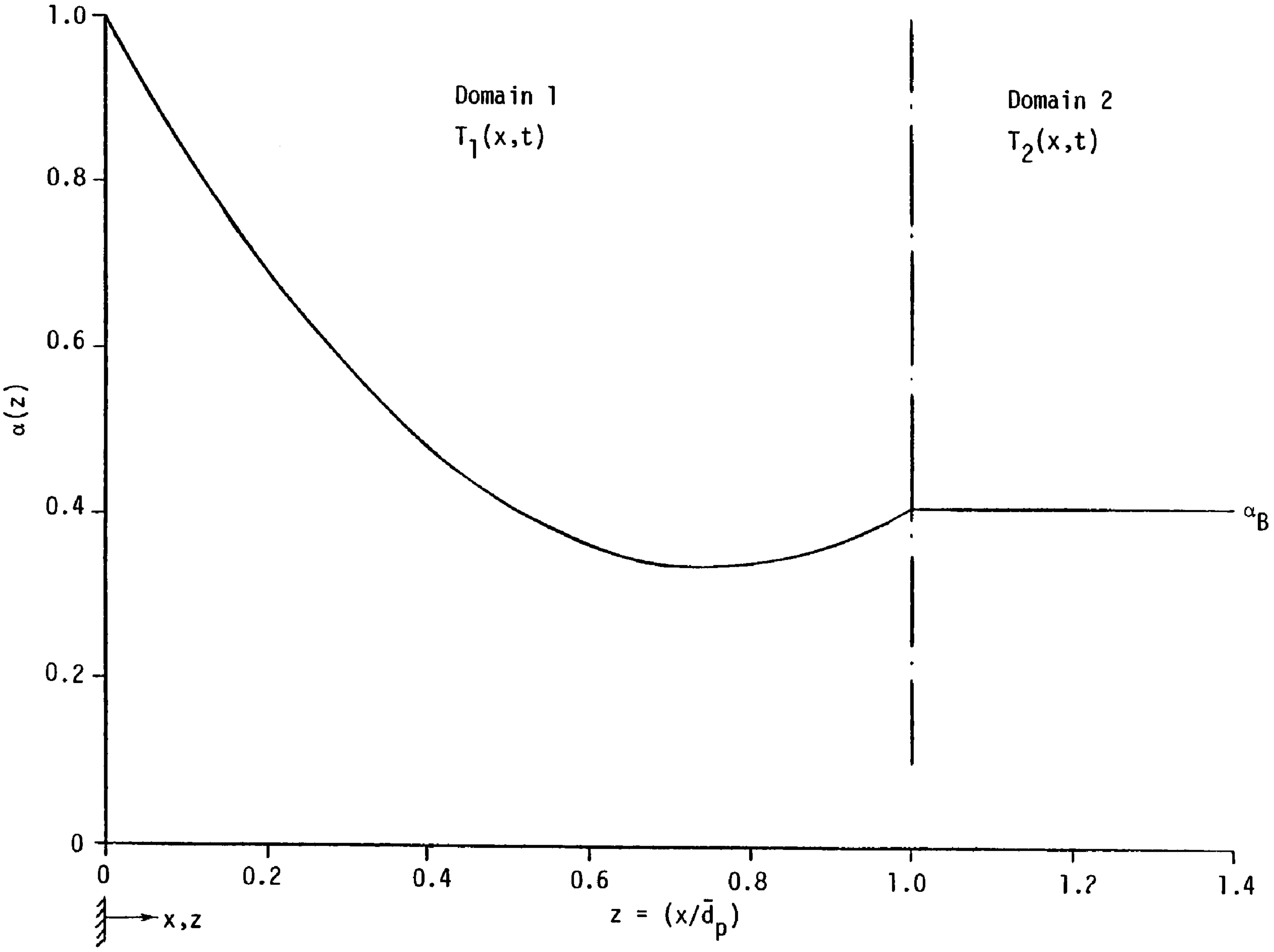

Figure 63 Voidage variation near the wall

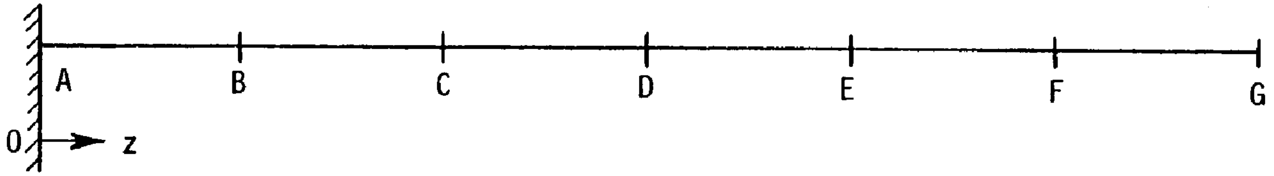

	A		B		C		D		E		F		G	F_o Range
z	0		0.4		1.2		2.8		3.6					
Step Size		0.02		0.04		0.08		0.16						0.001-0.20
Node	1		21		41		61		66					
z	0		1.2		1.68		2.64		4.56		8.40		21.2	
Step Size		0.04		0.08		0.16		0.32		0.64		1.28		0.50-4.0
Node	1		31		37		43		49		55		65	
z	0		1.68		2.64		4.56		8.40		21.2		46.8	
Step Size		0.08		0.16		0.32		0.64		1.28		2.56		10-100
Node	1		22		28		34		40		50		60	

Figure 64 Grid layout for numerical solution

REFERENCES

1. Kunii, D. and Levenspiel, O., *Fluidization Engineering*, John Wiley and Sons, New York, 1969.

2. Botterill, J.S.M., *Fluid-bed Heat Transfer*, Academic Press, New York, 1975.

3. Zabrodsky, S.S., *Hydrodynamics and Heat Transfer in Fluidized Beds*, M.I.T. Press, Cambridge, MA, 1966.

4. Zenz, F.A. and Othmer, D.F., *Fluidization and Fluid-Particle Systems*, Reinhold, New York, 1960.

5. Vreedenberg, H.A., "Heat Transfer between a Fluidized Bed and a Horizontal Tube," *Chem. Eng. Sci.*, vol. 9, 1958, p. 52.

6. Lese, H.K. and Kermode, R.I., "Heat Transfer from a Horizontal Tube to a Fluidized Bed in the Presence of Unheated Tubes," *Can. J. Chem. Eng.*, vol. 50, 1972, p. 44.

7. Petrie, J.C., Freeby, W.A., and Buckham, J.A., "In-bed Heat Exchangers," *Chem. Eng. Prog.*, vol. 64, no. 7, 1968, p. 45.

8. Gel'perin, N.I., Ainshtein, V.G. and Korotyanskaya, L.A., "Heat Transfer between a Fluidized Bed and Staggered Bundles of Horizontal Tubes," *Int. Chem. Eng.*, vol. 9, no. 1, 1969, p. 137.

9. Genetti, W.E., Schmall, R.A. and Grimmett, E.S., "The Effect of Tube Orientation on Heat Transfer with Bare and Finned Tubes in a Fluidized Bed," *Chem. Eng. Prog. Symp. Series*, vol. 67, no. 116, 1971, p. 90.

10. Bartel, W.J. and Genetti, W.E., "Heat Transfer from a Horizontal Bundle of Bare and Finned Tubes in an Air Fluidized Bed," *AIChE Symp. Series*, vol. 69, no. 128, 1973, p. 85.

11. Khan, A.R., Richardson, J.F. and Shakiri, K.J., "Heat Transfer between a Fluidized Bed and a Small Immersed Surface," in *Fluidization*, edited by Davidson, J.F. and Keairns, D.L., Cambridge University Press, London, 1978, p. 351.

12. Andeen, B.R. and Glicksman, L.R., "Heat Transfer to Horizontal Tubes in Shallow Fluidized Beds," ASME Paper 76-HT-67, *ASME-AIChE Heat Transfer Conference*, St. Louis, Mo., 1976.

13. Baskakov, A.P., et al., "Certain Problems of Fluidized-Bed Heat Transfer," Heat Transfer-Sov. Res., vol. 8, no. 5, 1976, p. 17.

14. Ainshtein, V.G. and Gel'perin, N.I., "Heat Transfer between a Fluidized Bed and a Surface," Int. Chem. Eng., vol. 6, no. 1, 1966, p. 67.

15. Gel'perin, N.I. and Einstein, V.G., "Heat Transfer in Fluidized Beds," in Fluidization, edited by Davidson, J.F. and Harrison, D., Academic Press, London, 1971, p. 471.

16. Gutfinger, C. and Abuaf, N., "Heat Transfer in Fluidized Beds," Adv. Heat Transfer, vol. 10, 1974, p. 167.

17. Zabrodsky, S.S., Antonishin, N.V., and Parnas, A.L., "On Fluidized Bed-to-Surface Heat Transfer," Can. J. Chem. Eng., vol. 54, 1976, p. 52.

18. Saxena, S.C., Grewal, N.S., Gabor, J.D., Zabrodsky, S.S. and Galershtein, D.M., "Heat Transfer between a Gas Fluidized Bed and Immersed Tubes," Adv. Heat Transfer, vol. 14, 1978, p. 149.

19. Leva, M., Weintraub, M. and Grummer, M., "Heat Transmission through Fluidized Bed of Fine Particles," Chem. Eng. Prog., vol. 45, 1949, p. 563; Leva, M. and Grummer, M., Chem. Eng. Prog., vol. 48, 1952, p. 307.

20. Dow, W.M. and Jacob, M., "Heat Transfer between a Vertical Tube and a Fluidized Air-Solid Mixture," Chem. Eng. Prog., vol. 47, 1951, p. 637.

21. Levenspiel, O. and Walton, J.S., "Bed Wall Heat Transfer in Fluidized Systems," Chem. Eng. Prog. Symp. Series, vol. 50, no. 9, 1954, p. 1.

22. Wen, C.Y. and Leva, M., "Fluidized-bed Heat Transfer: A Generalized Dense Phase Correlation," AIChE J., vol. 2, 1956, p. 482.

23. Wasan, D.T. and Ahluwalia, M.S., "Consecutive Film and Surface Renewal Mechanism for Heat or Mass Transfer from a Wall," Chem. Eng. Sci., vol. 24, 1969, p. 1535.

24. van Heerden, C., Nobel, A.P.P., and van Krevelen, D.W., "Mechanism of Heat Transfer in Fluidized Beds," Ind. Eng. Chem., vol. 45, no. 6, 1953, p. 1237.

25. Ziegler, E.N. and Brazelton, W.T., "Mechanism of Heat Transfer to a Fixed Surface in a Fluidized Bed," Ind. Eng. Chem. Fundam., vol. 3, no. 2, 1964, p. 94.

26. Mickley, H.S. and Fairbanks, D.F., "Mechanism of Heat Transfer to Fluidized Beds," AIChE J., vol. 1, 1955, p. 374.

27. Mickley, H.S., Fairbanks, D.F. and Hawthorn, R.D., "The Relation Between the Transfer Coefficient and Thermal Fluctuations in Fluidized-Bed Heat Transfer," Chem. Eng. Prog. Symp. Series, vol. 57, no. 32, 1961, p. 51.

28. Botterill, J.S.M. and Williams, J.R., "The Mechanism of Heat Transfer to Gas-fluidized Beds," Trans. Inst. Chem. Engrs., vol. 41, 1963, p. 217.

29. Botterill, J.S.M., Brundrett, G.W., Cain, G.L. and Elliott, D.E., "Heat Transfer to Gas Fluidized Beds," Chem. Eng. Prog. Symp. Series, vol. 62, no. 62, 1966, p. 1.

30. Ziegler, E.N., Koppel, L.B. and Brazelton, W.T., "Effects of Solid Thermal Properties on Heat Transfer to Gas Fluidized Beds," Ind. Eng. Chem. Fundam., vol. 3, no. 4, 1964, p. 324.

31. Baskakov, A.P., "The Mechanism of Heat Transfer Between a Fluidized Bed and a Surface," Int. Chem. Eng., vol. 4, no. 2, 1964, p. 320; "Transfer of Heat from an Isothermal Surface to a Continuous Flow of Dispersed Medium," Heat Transfer - Sov. Res., vol. 1, no. 6, 1969, p. 103.

32. Yoshida, K., Kunii, D. and Levenspiel, D., "Heat Transfer Mechanisms between Wall Surface and Fluidized Bed," Int. J. Heat Mass Trans., vol. 12, 1969, p. 529.

33. Toor, H.L. and Marchello, J.M., "Film-penetration Model for Mass and Heat Transfer," AIChE J., vol. 4, no. 1, 1958, p. 97.

34. Koppel, L.B., Patel, R.D. and Holmes, J.T., "Part-IV: Wall to Fluidized Bed Heat Transfer Coefficients," AIChE J., vol. 16, 1970, p. 464.

35. Kubie, J. and Broughton, J., "A Model of Heat Transfer in Gas Fluidized Beds," Int. J. Heat Mass Trans., vol. 18, 1975, p. 289.

36. Özkaynak, T.F. and Chen, J.C., "Evaluation of the Emulsion Phase Residence Times in Fluidized Beds and its use in Heat Transfer Models," AIChE J., vol. 26, no. 4, 1980, p.544.

37. Antonishin, N.V., Geller, M.A. and Parnas, A.L., "Hyperbolic Equation of Heat Conduction for Dispersed Systems," J. Eng. Phys., vol. 26, no. 3, 1974, p. 353.

38. Botterill, J.S.M. and Butt, M.H.D., "Achieving High Heat Transfer Rates in Fluidized Beds," Br. Chem. Eng., vol. 13, no. 7, 1968, p. 1000.

39. Gabor, J.D., "Wall-to-Bed Heat Transfer in Fluidized and Packed Beds," Chem. Eng. Prog. Symp. Series, vol. 66, no. 105, 1970, p. 76.

40. Chung, B.T.F., Fan, L.T. and Hwang, C.L., "A Model of Heat Transfer in Fluidized Beds," J. Heat Trans., vol. 94, 1972, p. 105.

41. Agrawal, S. and Ziegler, E.N., "On the Optimum Transfer Coefficient at an Exchange Surface in a Gas-fluidized Bed," Chem. Eng. Sci., vol. 24, 1969, p. 1235.

42. Baskakov, A.P., et al., "Heat Transfer to Objects Immersed in Fluidized Beds," Powder Technol., vol. 8, 1973, p. 273.

43. Selzer, V.W. and Thomson, W.J., "Fluidized Bed Heat Transfer--The Packet Theory Revisited," AIChE Symp. Series, vol. 73, no. 161, 1977, p. 29.

44. Krause, W.B. and Peters, A.R., "Heat Transfer Mechanisms Near Horizontal Heat Exchange Tubes in an Air Fluidized Bed of Uniformly Sized Glass Particles," ASME Paper 79-HT-88, Joint ASME/AIChE 18th National Heat Transfer Conference, San Diego, CA, 1979.

45. Botterill, J.S.M. and Desai, M., "Limiting Factors in Gas-fluidized Bed Heat Transfer," Powder Technol., vol. 6, no. 4, 1972, p. 231.

46. Baskakov, A.P. and Suprun, V.M., "Determination of the Convective Component of the Heat Transfer Coefficient to a Gas in a Fluidized Bed," Int. Chem. Eng., vol. 12, no. 2, 1972, p. 324.

47. Denloye, A.O.O. and Botterill, J.S.M., "Bed to Surface Heat Transfer in a Fluidized Bed of Large Particles," Powder Technol., vol. 19, no. 2, 1978, p. 197.

48. Staub, F.W., "Solids Circulation in Turbulent Fluidized Beds and Heat Transfer to Immersed Tube Banks," J. Heat Transfer, Trans. ASME, vol. 101, 1979, p. 391.

49. Özkaynak, T.F. and Chen, J.C., "Average Residence Times of Emulsion and Void Phases at the Surface of Heat Transfer Tubes in Fluidized Beds," AIChE Symp. Series, vol. 74, no. 174, 1978, p. 334.

50. Edwards, D.M. and Chen, J.C., "Capacitance Probe Measurements on the Surface of a Horizontal Tube in a Fluidized Bed," Report TS-773, Dept. of ME and Mech., Lehigh University, May 1977.

51. Chen, J.C., "Heat Transfer to Tubes in Fluidized Beds," ASME Paper 76-HT-75, ASME-AIChE Heat Transfer Conference, St. Louis, Mo., 1976.

52. Gel'perin, N.I., Ainshtein, V.G. and Zaikovskii, A.V., "Variation of Heat Transfer Intensity Around the Perimeter of a Horizontal Tube in a Fluidized Bed," J. Eng. Phy., vol. 10, no. 6, 1966, p. 473.

53. Gel'perin, N.I., Einstein, V.G., Korotjanskaja, L.A. and Perevozchikova, J.P., Teor. Oznovy Khim. Technol., vol. 2, 1968, p. 430.

54. Berg, B.V. and Baskakov, A.P., "Investigation of Local Heat Transfer Between a Fixed Horizontal Cylinder and a Fluidized Bed," Int. Chem. Eng., vol. 14, no. 3, 1974, p. 440.

55. Nixon, T., "Circuit Design for Capacitance Probes," Instrumentation Laboratory, Dept. of ME and Mech., Lehigh University, 1978 (unpublished).

56. Glass, D.H. and Harrison, D., "Flow Patterns Near a Solid Obstacle in a Fluidized Bed," Chem. Eng. Sci., vol. 19, 1964, p. 1001.

57. Botterill, J.S.M., George, J.S. and Besford, H., "Bubble Chains in Gas Fluidized Beds," Chem. Eng. Prog. Symp. Series, vol. 62, no. 62, 1966, p. 7.

58. Hager, W.R. and Thomson, W.J., "Bubble Behavior around Immersed Tubes in a Fluidized Bed," AIChE Symp. Series, vol. 69, no. 128, 1973, p. 68.

59. Staub, F.W. and Canada, G.S., "Effect of Tube Bank and Gas Density on Flow Behavior and Heat Transfer in Fluidized Beds," in Fluidization, edited by Davidson, J.F. and Keairns, D.L., Cambridge University Press, London, 1978, p. 339.

60. Leva, M., Takashi, S. and Wen, C.Y., Génie Chimique, Supplement to Chimie et Industrie, vol. 74, no. 2, 1956, p. 33.

61. Syromyatnikov, N.I., Kulikov, V.M., Nosov, V.S. and Korolev, V.N., "The Instantaneous Local Rate of External Heat Transfer in an Inhomogeneous Fluidized Bed," Heat Transfer - Sov. Res., vol. 8, no. 5, 1976, p. 42.

62. Kunii, D. and Smith, J.M., "Heat Transfer Characteristics of Porous Rocks," AIChE J., vol. 6, no. 1, 1960, p. 71.

63. Kunii, D. and Yagi, S., "Studies on Heat Transfer Near Wall Surface in Packed Beds," AIChE J., vol. 6, no. 1, 1960, p. 97.

64. Bauer, R. and Schlunder, E.U., "Effective Radial Thermal Conductivity of Packings in Gas Flow. Part II. Thermal Conductivity of the Packing Fraction Without Gas Flow," Int. Chem. Eng., vol. 18, no. 2, 1978, p. 189.

65. Korolev, V.N., Syromyatnikov, N.I. and Tolmachev, E.M., "The Structure of Fixed and Fluidized Granular Beds near Immersed Walls," J. Eng. Phys., vol. 21, no. 6, 1971, p. 973.

66. Pillai, K.K., "Voidage Variation at the Wall of a Packed Bed of Spheres," Chem. Eng. Sci., vol. 32, no. 1, 1977, p. 59.

67. Davidson, J.F. and Harrison, D., Fluidized Particles Cambridge University Press, New York, 1963.

68. Jepson, G., Poll, A. and Smith, W., "Heat Transfer from Gas to Wall in a Gas/Solids Transport Line," Trans. Inst. Chem. Engrs., vol. 41, 1963, p. 207.

69. Danziger, W.J., "Heat Transfer to Fluidized Gas-Solids Mixtures in Vertical Transport," I&EC Process Des. and Dev., vol. 2, no. 4, 1963, p. 269.

70. Pfeffer, R., Rossetti, S. and Lieblein, S., "Analysis and Correlation of Heat Transfer Coefficient and Friction Factor Data for Dilute Gas-Solid Suspensions," NASA TN D-3603, 1966.

71. Depew, C.A. and Kramer, T.J., "Heat Transfer to Flowing Gas-Solid Mixtures," Adv. Heat Transfer, vol. 9, 1973, p. 113.

72. Shrayber, A.A., "Turbulent Heat Transfer in Pipe Flows of Gas-Conveyed Solids," Heat Transfer-Sov. Res., vol. 8, no. 3, 1976, p. 60.

73. Gel'perin, N.I., et al., "Structure and Heat Transfer in Turbulent Gas Suspension Flows," Heat Transfer - Sov. Res., vol. 8, no. 5, 1976, p. 77.

74. Shrayber, A.A., "Model of Turbulent Heat Transfer by Gas-Solid-Flows," Heat Transfer - Sov. Res., vol. 9, no. 3, 1977, p. 35.

75. Holman, J.P., Heat Transfer, McGraw-Hill Book Co., New York, 1963, p. 147.

76. Zukauskas, A., "Heat Transfer from Tubes in Crossflow," Adv. Heat Transfer, vol. 8, 1972, p. 93.

77. Two-phase Flow and Heat Transfer in Fluidized Beds, Final Technical Report, SRD-78-103, Thermal Branch, General Electric Company, Schenectady, New York, December 1978.

78. Carnahan, B., Luther, H.A. and Wilkes, J.O., Applied Numerical Methods, John Wiley and Sons, New York, 1969.

79. Zellner, M.G., "DSS/1--Distributed Systems Simulator," Ph.D. Dissertation, Lehigh University, Bethlehem, Pa., 1970.

80. Schiesser, W.E., "DSS/2 (Differential Systems Simulator, Version 2)--An Introduction to the Numerical Method of Lines Integration of Partial Differential Equations," Lehigh University, Bethlehem, Pa., March 1977.

81. Carver, M.B., in "Advances in Computer Methods for Partial Differential Equations," edited by Vichnevetsky, AICA, Rutgers University, New Jersey, 1975.

82. Hindmarsh, A.C., "GEAR: Ordinary Differential Equation System Solver," Lawrence Livermore Laboratory Report UCID-30001, Revision 3, 1974.

83. Hindmarsh, A.C., "GEARB: Solution of Ordinary Differential Equations Having Banded Jacobian," Lawrence Livermore Laboratory Report UCID-30059, Revision 1, March 1975.

84. The IMSL Library, Reference Manual, vol. 1, International Mathematical and Statistical Libraries, Inc., Houston, Texas, January 1979.

85. Schiesser, W.E., "DSS2E--Gearb Package," Computer Program Library, Lehigh University, Bethlehem, Pa., 1979.

APPENDICES

A. Analysis of the Capacitance Signal

As stated in section 3.3, the capacitance signal is normalized to lie between the values 0 and 1, and a signal level corresponding to a void fraction value of 0.8 (α_C) is used to demarcate between the dense and the lean phases.

Let the signal level at cut off for the binary classification be denoted as L_R. If the signal lies intirely on either side of the reference level (L_R), the fractional contact time of that phase becomes unity for that sample and the time-mean density of the phase in contact is obtained by integrating the signal.

Renewal type contact behavior is considered to occur when:

i) the signal intersects the reference level (L_R) and crosses over from one phase to the other,

ii) the time duration of contact of the latter phase exceeds a certain critical time period based upon a pre-selected value of Fourier number ($F_0 = k\theta/C_p \bar{d}_p^2 \geq 0.001$), and

iii) the ratio of the two contact times exceeds a specified value i.e. the time duration of contact required for the second phase is dictated by the length of time the first phase happens to be in contact with the surface.

These conditions were stipulated in order to ensure that the process is identified as one of renewal only when a fresh emulsion comes into contact with the tube surface.

Let I dense-phase contacts and J lean-phase contacts occur over the time duration of the signal. Consider ith dense-phase contact and jth lean-phase contact as shown in Figure 62. Let the area under the signal between A and B be denoted by Area_i and the time period between A and B by ϵ_{D_i} and the corresponding quantities between B and C by Area_j and θ_{L_j} respectively. Then the fluidization parameters can be estimated from the ensuing relations:

$$\bar{\theta}_D = \left[\frac{\sum_{i=1}^{I} \theta_{D_i}}{\sum_{i=1}^{I} \sqrt{\theta_{D_i}}}\right]^2$$

$$\alpha_D = 1 - \left[\left\{\left(\sum_{i=1}^{I} \text{Area}_i\right) \Big/ \left(\sum_{i=1}^{I} \theta_{D_i}\right)\right\} (1 - \alpha_{\text{packed}})\right]$$

$$\alpha_L = 1 - \left[\left\{\left(\sum_{j=1}^{J} \text{Area}_j\right) \Big/ \left(\sum_{j=1}^{J} \theta_{L_j}\right)\right\} (1 - \alpha_{\text{packed}})\right]$$

$$f_L = \left(\sum_{j=1}^{J} \theta_{L_j}\right) \Big/ \left[\left(\sum_{j=1}^{J} \theta_{L_j}\right) + \left(\sum_{i=1}^{I} \theta_{D_i}\right)\right]$$

In this manner, the root-square-average residence time of the dense phase ($\bar{\theta}_D$), the fraction of the total time the lean phase is in contact with the surface (f_L), and the time-averaged void fractions of the dense (α_D) and the lean (α_L) phases were determined for each sample. The values of these parameters averaged over a number of samples for different test conditions are furnished in Tables 8 through 13.

B. Heat Transfer During Surface Renewal - Problem Formulation and Method of Solution

Consider the dense phase that comes into intermittent contact with the tube surface. Following the treatment of Kubie and Broughton [35], the void fraction in the vicinity of the transfer surface or wall is presumed to vary in the manner shown in Figure 63. It is observed that away from the wall, the medium has a constant void fraction (α_D). It is now assumed that essentially one-dimensional conduction is prevalent and that heat is transferred in the direction normal to the wall. By applying the semi-infinite layer approximation and by neglecting the effect of wall curvature (reasonable for large $D/\bar{d}_p$ ratios), the governing equations for transient conduction into the dense phase can be written for constant wall temperature boundary condition as:

<u>domain 1</u> $(0 \leq x \leq \bar{d}_p)$

$$\rho(x)\, c_p(x) \frac{\partial T_1}{\partial t} = \frac{\partial}{\partial x} \left[k(x) \frac{\partial T_1}{\partial x} \right] \qquad (B.1)$$

with initial and boundary conditions

$$T_1(x,0) = T_B \tag{B.2}$$

$$T_1(0,t) = T_W \tag{B.3}$$

<u>domain 2</u> $(x \geq \bar{d}_p)$

$$(\rho c_p)_D \frac{\partial T_2}{\partial t} = k_D \frac{\partial^2 T_2}{\partial x^2} \tag{B.4}$$

with initial and boundary conditions

$$T_2(x,0) = T_B \tag{B.5}$$

$$\lim_{x \to \infty} T_2(x,t) = T_B \tag{B.6}$$

and, at the interface $(x = \bar{d}_p)$

$$T_1(\bar{d}_p,t) = T_2(\bar{d}_p,t) \tag{B.7}$$

$$k(x) \left. \frac{\partial T_1}{\partial x} \right|_{x=\bar{d}_p,t} = k_D \left. \frac{\partial T_2}{\partial x} \right|_{x=\bar{d}_p,t} \tag{B.8}$$

These equations can be expressed in a normalized form by transforming the variables:

$$z = x/\bar{d}_p \ , \ \phi = T_1 - T_B \ , \ \eta = T_2 - T_B \ ,$$

$$F_i = (k_D \ t) \ / \ [\ (\rho c_p)_D \ \bar{d}_p^{\ 2}]$$

The properties in the wall region ($z \leq 1$) can be approximated by

$$\rho(x)\, c_p(x) = \rho_s c_{ps}\,(1-\alpha) + \rho_g\, c_{pg}\, \alpha$$

$$\simeq \rho_s\, c_{ps}(1-\alpha) \text{ for } \frac{\rho_g\, c_{pg}}{\rho_s\, c_{ps}} < < 1$$

$$k(x) \simeq k_g + \frac{(1-\alpha)}{(1-\alpha_D)}\ (k_D - k_g)$$

Also, $(\rho c_p)_D \simeq \rho_s\, c_{ps}(1-\alpha_D)$ for $\frac{\rho_g\, c_{pg}}{\rho_s\, c_{ps}} < < 1$

The voidage variation in the vicinity of the wall ($z \leq 1$) can be estimated from the relation given by Kubie and Broughton [35]:

$$\alpha = 1-3\ (1-\alpha_D)\ (z - \frac{2}{3} z^2)$$

By substituting the foregoing relations in equations (B.1)-(B.8) and by rearranging the resulting expressions, the problem can be formulated as:

$$\frac{\partial\phi}{\partial F_i} = \frac{k_g}{k_D\ z(3-2z)}\ \frac{\partial}{\partial z}\left[\{1 + z(3-2z)(\frac{k_D}{k_g} - 1)\}\ \frac{\partial\phi}{\partial z}\right] \quad \text{for } z \leq 1 \qquad (B.9)$$

$$\frac{\partial\eta}{\partial F_i} = \frac{\partial^2\eta}{\partial z^2} \qquad \text{for } z \geq 1 \qquad (B.10)$$

subject to

$$\phi(z,0) = 0 \quad \text{for } z \leq 1 \qquad (B.11)$$

$$\eta(z,0) = 0 \quad \text{for } z \geq 1 \qquad (B.12)$$

$$\phi(0,F_i) = (T_W - T_B) = \text{constant} \qquad (B.13)$$

$$\lim_{z\to\infty} \eta(z,F_i) = 0 \tag{B.14}$$

$$\phi(1,F_i) = \eta(1,F_i) \tag{B.15}$$

$$k(z) \left.\frac{\partial\phi}{\partial z}\right|_{z=1,F_i} = k_D \left.\frac{\partial\eta}{\partial z}\right|_{z=1,F_i} \tag{B.16}$$

An attempt was made to solve these equations analytically. But owing to algebraic complexity, that approach was abandoned and a numerical solution procedure was chosen instead. A survey was then made of the different numerical techniques that are frequently used for solving partial differential equations - explicit and implicit finite difference approximations [78,79] and numerical method of lines (NMOL) [80,81]. Due to the structure of the present problem - the development of a temperature profile with a steep gradient at the wall and the need to obtain solutions over a wide range of Fourier modulus ($F_o = k_D\, \bar{\theta}_D / C_{pD}\, \bar{d}_p^2$) values (from 0.001 to 100) - the numerical method of lines was selected for use in this investigation.

NMOL involves the representation of the spatial derivatives by finite difference approximations. This serves to transform the partial differential equations into ordinary differential equations, which can then be solved by means of existing ODE integrators [78,80,82-85].

A non-uniform grid (shown in Figure 64) was used to achieve spatial discretization. The spatial derivatives

(ϕ_z, n_z, ϕ_{zz}, n_{zz}) were all represented by second-order-correct finite difference approximations. Appropriate adjustments were made in deriving the relations for the boundary and interfacial nodal points. The resulting system of ordinary differential equations was solved by the GEARB integration scheme [85]. GEARB is a predictor-corrector type time integrator and is intended for use in ODE systems that have a banded Jacobian matrix and for solving stiff differential equations [82-85]. The GEARB package also includes features such as automatic step-size adjustment and error control to achieve efficient integration. The attributes mentioned above in conjunction with lower computer time requirements prompted the selection of GEARB to implement time integration.

Numerical solutions were obtained, as a function of the time-mean Fourier modulus (F_o), for seven different values of the conductivity ratio (k_D/k_g = 1.4, 2.21, 4.0, 6.03, 11.0, 20.0 and 34.7). A variable size grid and a marching technique were used to save on computer time. The procedure employed, for a given value of the conductivity ratio (k_D/k_g), was as follows:

(i) specify the value of F_o for which the time-mean Nusselt number ($Nu_s' = h_s' \bar{d}_p/k_D$, where h_s' is the computed average heat transfer coefficient during the dense phase residence time $\bar{\theta}_D$)is to be determined; this value of F_o also becomes the final value of F_i for the run;

(ii) decide on the number of base points at which print-out is desired during the run and indicate the print interval;

(iii) specify the grid size in the spatial domain and indicate the number of ordinary differential equations to be solved, by getting an estimate for the depth of heat penetration from equation (20);

(iv) provide the initial/starting values for the temperature distribution; for the first run, the initial values are specified in accordance with equations (B.11-B.14);

(v) solve the system of ordinary differential equations and continue the integration process in steps for one print interval;

(vi) print-out the temperature distribution in the spatial domain; determine the temperature gradient at the wall and compute the instantaneous heat transfer coefficient (h_{si});

(vii) carry on with the integration process until the values of h_{si} at all the base points are determined;

(viii) at the end of the run, calculate h_s' by using Simpson's rule [78] to numerically integrate the h_{si} values over the run interval;

(ix) compute Nu_s'

(x) use the output from this run as the input for the next run and continue.

In this manner, the values of Nu_s' were determined for time-mean Fourier modulus (F_o) ranging from 0.001 to 100.0.

Sample results are shown in Figure 47.

C. Evaluation of the Local Heat Transfer Coefficient - Sample Calculation

Consider a single horizontal tube immersed in a fluidized bed of medium size particles (GT-3). Let us estimate the local heat transfer coefficient (h) at the top of the tube (β=0°) for fluidization at a system pressure of 202.6 kPa. If the air flow rate through the bed corresponds to a U_N parameter value of 0.18, the superficial gas velocity (U_{sg}) can be determined using the property values listed in Table 1:

$$U_{sg} = 0.18\ (U_t - U_{mf}) + U_{mf}$$

$$= 0.18\ (3.10 - 0.254) + 0.254$$

$$= 0.766 \text{ m/s}$$

The values of the fluidization parameters for this test condition can be read from Figures 26-29:

$$\bar{\theta}_D = 0.18 \text{ s},\ f_L = 0.421,\ \alpha_D = 0.629,\ \alpha_L = 0.870$$

The thermo-physical properties of air at 300°K are:

$$k_g = 0.026 \text{ w/m-°K},\ c_{pg} = 1006 \text{ J/kg-°K},$$

$$\rho_g = 2.36 \text{ kg/m}^3,\ \mu_g = 18.5 \times 10^{-6} \text{ NS/m}^2$$

The thermal conductivity of the dense phase (k_D) is computed using equation (13) and the property values listed in Table 1:

$$B = 1.25 \left(\frac{1-\alpha_D}{\alpha_D}\right)^{10/9} = 1.25\left(\frac{0.371}{0.629}\right)^{10/9} = 0.695$$

$$\frac{k'}{k_g} = \frac{2}{(1-B\frac{k_g}{k_s})}\left[\frac{(1-\frac{k_g}{k_s})\,B}{(1-B\frac{k_g}{k_s})^2}\ln\left(\frac{k_s}{B\,k_g}\right) - \left(\frac{B+1}{2}\right) - \frac{(B-1)}{(1-B\frac{k_g}{k_s})}\right]$$

$$= 4.50$$

$$k_D = k_g\,[(1-\sqrt{1-\alpha_D}) + \sqrt{1-\alpha_D}\,(\frac{k'}{k_g})]$$

$$= 0.081 \text{ w/m-}^{\circ}\text{K}$$

From equation (12) in the text:

$$C_{pD} = \rho_s\, c_{ps}\,(1-\alpha_D) + \rho_g\, c_{pg}\,\alpha_D$$

$$= 694313.6 \text{ J/m}^3\text{-}^{\circ}\text{K}$$

Now, the time-mean Fourier modulus is:

$$F_o = \frac{k_D\ \bar{\theta}_D}{C_{pD}\ \bar{d}_p^{\,2}} = 0.057$$

From equation (17), the effective correction factor (C) can be evaluated:

$$C = \exp\left[-\frac{a_1}{F_o^{\,a_2+a_3\,\ell n F_o}}\right]$$

$$= 0.400$$

The transient conduction component (h_s) can be calculated from equation (16):

$$h_s = 2C \sqrt{\frac{k_D \; C_{pD}}{\pi \; \bar{\theta}_D}} = 252.9 \quad w/m^2\text{-}°K$$

The effect of fluid flow on conduction is accounted for by the component h_f; this is computed from equations (19), (20) and (21):

$$h_{mf} = 0.26 \frac{k_g}{D} \; Ar^{0.31}$$

$$= 0.26 \frac{(0.026)}{(0.0286)} \; (38134.8)^{0.31} = 6.22 \; w/m^2\text{-}°K$$

$$(x_p/\bar{d}_p) = 3.6 \sqrt{F_o} = 0.859$$

$$h_f = [1 - \exp\,(- \frac{x_p}{\bar{d}_p})] \; h_{mf}$$

$$= 3.6 \; w/m^2\text{-}°K$$

The effective heat transfer coefficient in the dense phase (h_D) then is:

$$h_D = h_s + h_f = 256.5 \; w/m^2\text{-}°K$$

Now, from equation (28):

$$\frac{h_L}{h_g} = [1 + 194.0 \; (\frac{g \; \bar{d}_p}{U_{sg} \; \bar{U}_t})(\frac{\rho_s}{\rho_g})(\frac{1-\alpha_L}{\alpha_L})(\frac{c_{ps}}{c_{pg}})]^{0.5}$$

$$= [1 + 194.0 \; (\frac{9.81 x 0.000610}{0.766 x 3.79})(\frac{2480}{2.36})(\frac{0.13}{0.87})(\frac{753}{1006})]^{0.5}$$

$= 6.93.$

The heat transfer coefficient for gas flow alone (h_g) is estimated from the relation given in [75]:

$$\frac{h_g D}{k_g} = 0.683 \left(\frac{\rho_g U_{gm} D}{\mu_g} \right)^{0.466} \left(\frac{c_{pg} \mu_g}{k_g} \right)^{1/3}$$

$$\text{for } 40 < \left(\frac{\rho_g U_{gm} D}{\mu_g} \right) < 4000$$

where U_{gm} is the gas velocity based on minimum flow area.

$$U_{gm} = (0.766)(\pi x 0.203^2/4)/[(\pi x 0.203^2/4)-(0.203 x 0.0286)]$$

$$= 0.933 \text{ m/s}$$

$$h_g = (0.683)\frac{(0.026)}{(0.0286)} \left[\frac{(2.36)(0.933)(0.0286)}{18.5 \times 10^{-6}}\right]^{0.466} (0.895)$$

$$= (0.5557)\ (3404)^{0.466} = 24.58 \text{ w/m}^2\text{-°K}$$

The effective heat transfer coefficient in the lean phase (h_L) then is:

$$h_L = (6.93)(24.58) = 170.3 \text{ w/m}^2\text{-°K}$$

From equation (9), the local heat transfer coefficient (h) for the top location (β=0°) can be estimated as:

$$h = f_L\ h_L + (1 - f_L)\ h_D$$

$= (0.421)(170.3) + (0.579)(256.5)$

$= 220.2\ \mathrm{w/m^2\text{-}{}^\circ K}$

In a similar manner, the local heat transfer coefficients for other angular positions can be computed.

VITA

The author was born one September mornin' (9-13-1950) to Parvathi and Natarajan in India. He obtained his undergraduate degree in mechanical engineering from REC, Durgapur in 1971 and his Masters degree from IIT Kanpur in 1974. He worked for a year at VRDE, Ahmednagar as Senior Scientific Officer and came to Lehigh University in late 1975 to pursue a doctoral program.